

UNIVERSITÀ DEGLI STUDI DI TRIESTE



XXIV CICLO DEL DOTTORATO DI RICERCA IN NANOTECNOLOGIE

Borsa di Dottorato finanziata da Genefinity Srl.

NANOMATERIALS BASED ON II-VI SEMICONDUCTORS

SSD: ING-IND/22 - Scienza e Tecnologia dei Materiali

DOTTORANDO
Luca Cozzarini

DIRETTORE DELLA SCUOLA
Prof. Maurizio Fermèglia

SUPERVISORE
Prof. Vanni Lughi

ANNO ACCADEMICO 2010/2011

Abstract

This thesis describes: (i) synthesis and characterization of colloidal nanocrystals of II-VI semiconductor compounds; (ii) development of two novel materials using such nanocrystals as “building blocks”: (ii.a) a nanocrystals/polymer composite, to be used as phosphor in LED-based lighting devices; (ii.b) an inorganic, nano-structured multiphase material, showing a promising geometry as an electronic intermediate band material.

Different typologies of nanocrystals (single-phase, alloyed or core-shells) were successfully synthesized using air-stable, safe reagents. Their optical properties (absorption spectrum, fluorescence wavelength and fluorescence quantum yield) were mapped as function of different parameters. Good results in engineering optical properties were achieved by: (a) changing size and/or composition in single-phase nanocrystals; (b) tuning shell composition and thickness and/or mutually diffusing one material into the other in multi-phase nanocrystals. The influence of different surface ligands on optical properties and on solubility in different media was also studied.

Nanocrystal/polymer composite lenses were obtained from nanocrystals with desired fluorescence wavelength and quantum yield, mixed in an appropriate solvent with polymer pellets. The mixture was drop casted or tape casted on a solid substrate, obtaining solid, transparent lenses after solvent evaporation.

A nano-structured, all-inorganic material (composed of semiconductor nanocrystals embedded into a wider bandgap semiconductor) was obtained through self-assembly and densification of colloidal core-shells nanocrystals. The realization of this composite supracrystal was achieved via a multi-step process: (i) colloidal synthesis of core-shell nanocrystals; (ii) surface ligands exchange; (iii) assembly; (iv) heat treatment. Evolution of the optical properties during heat treatment suggests that it is possible to sinter the shell material without altering the internal nano-heterostructure, if temperature and time of the treatment are controlled properly.

Sommario (in Italian)

In questa tesi sono descritti: (I) la sintesi colloidale e la caratterizzazione di nanocristalli di semiconduttori II-VI; (II) lo sviluppo, utilizzando i suddetti nanocristalli quali “unità da costruzione”, di due materiali innovativi: (IIa) un composito nanocristalli/polimero, da usare come fosforo in dispositivi per illuminazione basati su LED; (IIb) un materiale inorganico nano-strutturato multifase, con una geometria promettente quale materiale a banda elettronica intermedia.

Differenti semiconduttori II-VI sono stati sintetizzati in forma di nanocristalli (monofasici, in forma di lega o in struttura di tipo “core-shell”) usando reagenti sicuri e stabili in atmosfera. Le loro proprietà ottiche (spettro di assorbimento, lunghezza d’onda di fluorescenze e resa quantica di fluorescenza) sono state mappate in funzione di numerosi parametri. Sono stati raggiunti ottimi risultati nel controllo delle proprietà ottiche sia in nanocristalli a fase singola (modificandone le dimensioni o la composizione chimica) che in nanocristalli multifase (regolandone la composizione e lo spessore della “shell”, nonché mutualmente diffondendo un materiale nell’altro). È stata anche studiata l’influenza di differenti leganti superficiali sulle proprietà ottiche e sulla solubilità dei nanocristalli in differenti solventi.

Lenti composite di nanocristalli/polimero sono state ottenute a partire da nanocristalli aventi la lunghezza d’onda e la resa quantica di fluorescenza desiderate, mescolandoli con pellet di polimero in solventi appropriati. La miscela è stata depositata su un supporto, tramite drop casting o tape casting, ottenendo lenti solide trasparenti dopo l’evaporazione del solvente.

Un materiale inorganico nano strutturato (costituito da nanocristalli di semiconduttore racchiusi all’interno di un secondo materiale semiconduttore a bandgap maggiore) è stato ottenuto tramite l’autoassemblaggio e la densificazione di nanocristalli core-shell sintetizzati con procedure di chimica colloidale. La realizzazione di suddetto sovra-cristallo si è svolta in più fasi: (i) sintesi colloidale; (ii) sostituzione dei leganti superficiali; (iii) assemblaggio; (iv) trattamento termico. I risultati derivanti dallo studio dell’evoluzione delle proprietà ottiche durante il trattamento termico suggeriscono che sia possibile sinterizzare il materiale della shell senza alterare la nano-eterostruttura interna, se la temperatura e il tempo del trattamento sono scelti opportunamente.

TABLE OF CONTENTS

<i>Abstract</i>	<i>i</i>
<i>Sommario (in italian)</i>	<i>ii</i>
<i>Table of Contents</i>	<i>iii</i>
<i>List of Figures</i>	<i>viii</i>
<i>List of Tables</i>	<i>x</i>
<i>Introduction</i>	<i>1</i>
Relevance and Motivations	<i>1</i>
Thesis Overview	<i>4</i>
References	<i>5</i>
<i>Chapter 1: Synthesis and Characterization of II-VI Semiconductor Nanocrystals</i>	<i>7</i>
Introduction	<i>8</i>
1.1 Optical Properties of Semiconductor Nanocrystals	<i>8</i>
1.1.1 The quantum confinement effect	<i>8</i>
1.1.2 Electron quantum state levels	<i>9</i>
1.1.3 Hole quantum state levels	<i>9</i>
1.1.4 Interpretation of a quantum dot absorption spectrum	<i>9</i>
1.1.5 Emission Stokes shift	<i>10</i>
1.1.6 Fluorescence quantum yield	<i>10</i>
1.2 Classification of Semiconductor Nanocrystals	<i>11</i>
1.2.1 Single phase nanocrystals	<i>11</i>
1.2.2 Multi-phase nanocrystals (core-shell or core-multishell)	<i>11</i>

1.2.3	Alloyed nanocrystals	12
1.3	Colloidal Synthesis.....	12
1.3.1	Nucleation theory	12
1.3.2	Nanocrystals synthesis techniques	14
1.3.3	Core-shell nanocrystals synthesis techniques	14
1.3.4	II-VI semiconductor nanocrystals synthesis	15
1.4	Surface Ligands	16
1.4.1	Synthesis ligands	16
1.4.2	Ligand exchange	16
Experimental Section		17
1.5	Synthesis	17
1.5.1	Semiconductor compounds used in this study.....	17
1.5.2	Materials	18
1.5.3	Precursor solutions preparation	18
1.5.4	Synthesis of single-phase nanocrystals	19
1.5.5	Synthesis of multi-phase nanocrystals	20
1.6	Diffusion Experiments	21
1.6.1	Materials	21
1.6.2	Samples preparation	21
1.6.3	Diffusion experiment	21
1.7	Ligands Exchange	22
1.7.1	Materials	22
1.7.2	Exchange with thiols	22
1.7.3	Exchange with metal-chalcogenide complexes and chalcogenide ligands	22
1.8	Characterization	23
1.8.1	Optical characterization	23
1.8.2	Size evaluation: size curves	23
1.8.3	Size evaluation: Transmission Electron Microscopy	24
1.8.4	Core-shell nanocrystals size evaluation: Concentric Shell Model	24
1.8.5	Nano-heterostructures and alloyed nanocrystals bandgap simulation	24
1.8.6	IR spectra of surface ligands	25

Results and Discussion	26
1.9 Results	26
1.9.1 Shared green chemistry synthesis approach	26
1.9.2 Synthesis and optical properties of single-phase nanocrystals	26
1.9.3 Synthesis and optical properties of core-shell nanocrystals	28
1.9.4 Synthesis of alloyed nanocrystals	37
1.9.5 Heat treatment effect on nanocrystals bandgap	38
1.9.6 Bandgap simulation	39
1.9.7 IR spectra of surface ligands	41
1.9.8 Effectiveness of ligands exchange procedures	44
1.9.9 Solubility and stability in water: effect of counter-ion	45
1.10 Conclusions and Future Developments	46
1.10.1 Results summary	46
1.10.2 Future developments	46
References	47
<i>Chapter 2 :</i> Semiconductor Nanocrystals as phosphors in LED-based white lighting devices	51
Introduction	52
2.1 Light Emitting Diodes	52
2.1.1 White emission from LED-based devices	52
2.1.2 White emission from LED/phosphors devices: state of the art	52
2.2 Semiconductor Nanocrystals as Phosphors	53
2.2.1 Polymer/NCs composite material	53
Experimental Section	54
2.3 Fluorescence Properties Characterization	54
2.3.1 Materials	54
2.3.2 Fluorescence wavelength measurements	54
2.3.3 Fluorescence quantum yield measurements	54
2.3.4 Ligands exchange	55

2.4	Polymer/NCs composite fabrication.....	55
	Results and Discussion.....	56
2.5	Results	56
2.5.1	Fluorescence wavelength and fluorescence quantum yield	56
2.5.2	Shell growth and diffusion influence on fluorescence wavelength	57
2.5.3	Shell growth influence on fluorescence quantum yield	57
2.5.4	Diffusion influence on fluorescence quantum yield	58
2.5.5	Surface ligands influence on fluorescence quantum yield	58
2.6	Conclusions and Future Developments	62
2.6.1	Results summary	62
2.6.2	Future developments: NCs/polymer composite material	63
	References.....	64
<i>Chapter 3:</i>	QD-based Intermediate Band Solar Cell from Colloidal Nanocrystals.....	65
	Introduction	66
3.1	Intermediate Band Materials	66
3.1.1	Intermediate band solar cell	66
3.1.2	Quantum dot-based intermediate band solar cell	67
	Realization Scheme	68
3.2	QD-ISBC from Colloidal Nanocrystals	68
3.2.1	Materials choice	68
3.2.2	Dot material choice	70
3.2.3	Barrier material choice	70
3.2.4	Organic ligands removal	71
3.2.5	Heat treatment design	71
3.2.6	Monitoring nanostructure evolution during heat treatment.....	72
3.3	Experimental	72
3.3.1	Materials	72

3.3.2	Ligands exchange procedure	72
3.3.3	Assembly	72
3.3.4	Heat treatments	73
3.3.5	Fluorescence wavelength measurements	73
	Results and Discussion	74
3.4	Heat treatments	74
3.4.1	Heat treatment effect on single-phase NCs	74
3.4.2	Heat treatment effect on multi-phase NCs	76
3.5	Conclusion and future developments	79
	References	80

List of Figures

<i>Fig. 1.1</i> : typical absorption spectrum of a quantum dot and QSLs	8
<i>Fig. 1.2</i> : CdSe NC absorption spectrum and allowed interband optical transitions	9
<i>Fig. 1.3</i> : schematic representing of excitation-deexcitation taking place at the band edge	10
<i>Fig. 1.4</i> : LaMer plot	13
<i>Fig. 1.5</i> : proposed reaction pathways in colloidal synthesis of CdSe NCs	16
<i>Fig. 1.6</i> : bandgap energies, CB and VC positions of II-VI compounds evaluated in this work	17
<i>Fig. 1.7</i> : TEM images of single-phase NCs	26
<i>Fig. 1.8</i> : absorption spectra of different sizes, single-phase NCs (CdTe, CdSe and CdS).....	27
<i>Fig. 1.9</i> : TEM images CdSe-based core-shell NCs	29
<i>Fig. 1.10</i> : TEM images CdTe-based core-shell NCs	30
<i>Fig. 1.11</i> : expected and measured diameter as a function of nominal shell thickness	32
<i>Fig. 1.12</i> : evolution of absorption PL after overgrowing ZnSe shell on CdSe NCs	33
<i>Fig. 1.13</i> : evolution of absorption PL after overgrowing CdS shell on CdSe NCs	33
<i>Fig. 1.14</i> : evolution of absorption PL after overgrowing CdS shell on CdTe NCs	34
<i>Fig. 1.15</i> : evolution of 1 st absorption peak and fluorescence peak position during shell growth	34
<i>Fig. 1.16</i> : schematic representation of CdSe-ZnSe and CdSe-CdS core-shell heterostructures	35
<i>Fig. 1.17</i> : schematic representation of possible configurations of CdTe-CdS core-shell NCs	36
<i>Fig. 1.18</i> : evolution of fluorescence peak position during CdS shell growth on CdTe NCs	37
<i>Fig. 1.19</i> : TEM images of alloyed NCs:	38
<i>Fig. 1.20</i> : 1 st absorption peak position as a function of heat treatment time	38
<i>Fig. 1.21</i> : hypsochromic shift of bandgap energy as a function of heat treatment time	39
<i>Fig. 1.22</i> : bandgap energy simulation for CdSe-ZnSe and CdSe-CdS core-shell NCs	40
<i>Fig. 1.23</i> : bandgap energy simulation for $Cd_xZn_{1-x}Se$ and $CdSe_xS_{1-x}$ alloyed NCs	40
<i>Fig. 1.24</i> : IR spectra of original surface ligands on CdSe and CdS compared with cadmium oleate	41
<i>Fig. 1.25</i> : IR spectra of original surface ligands on ZnSe compared with zinc oleate	41
<i>Fig. 1.26</i> : free carboxylic acid and metal-carboxylate complex	42

<i>Fig.1.27</i> : IR absorption spectra of oleic acid and cadmium oleate	42
<i>Fig. 1.28</i> : IR absorption spectra of original and new surface ligands (presumably MPA)	43
<i>Fig. 1.29</i> : IR absorption spectra of mercaptoacetic acid and new surface ligands	43
<i>Fig. 1.30</i> : mercaptoacetic acid and two possible configuration for its surface adsorption on CdS NCs	44
<i>Fig. 1.31</i> : IR absorption spectra of original new surface ligands (presumably SnS_4^{4-})	44
<i>Fig. 1.32</i> : absorption spectra CdTe NCs with MPA/ NH_4^+ (collected after different times)	45
<i>Fig. 2.1</i> : example of white lighting device based on LED emitter coupled with phosphors	53
<i>Fig. 2.2</i> : fabrication steps of a NCs/polymer composite	55
<i>Fig. 2.3</i> : fluorescence QY as a function of fluorescence wavelength for all synthesized NCs	56
<i>Fig. 2.4</i> : fluorescence spectra of some NCs emitting in the visible range	56
<i>Fig. 2.5</i> : fluorescence QY as a function of shell thickness for CdSe-ZnSe and CdSe-CdS NCs	57
<i>Fig. 2.6</i> : fluorescence QY as a function heat treatment time for CdSe-ZnSe NCs	58
<i>Fig. 2.7</i> : fluorescence QY of different NCs, with original ligands or MPA on their surface	59
<i>Fig. 2.8</i> : fluorescence QY of CdSe, CdSe-CdS and CdSe-CdS-ZnS NCs with orig. ligands or MPA	60
<i>Fig. 2.9 (A)</i> : fluorescence QY of CdSe and CdTe NCs with original ligands or MPA on their surface	61
<i>Fig. 2.9 (B)</i> : bulk CdSe and CdTe band positions and thiol redox level respect to vacuum energy level	61
<i>Fig. 2.10</i> : CdSeS-CdS partially alloyed core-shell NCs in colloidal solution, excited with UV light	62
<i>Fig. 2.11</i> : CdSeS-CdS partially alloyed NCs embedded in solid PMMA lens, excited with UV light	63
<i>Fig. 3.1</i> : energy bands and possible absorption processes in a IB-material	66
<i>Fig. 3.2</i> : Quantum Dot Supracrystal and its possible electronic bands configuration	67
<i>Fig. 3.3 (left)</i> : two-phase core-shell semiconductor nanocrystal	68
<i>Fig. 3.3 (right)</i> : semiconductor nanocrystals embedded into a wider bandgap semiconductor	68
<i>Fig. 3.4</i> : CB and VB positions respect to the vacuum level of II-VI compounds evaluated in this work	70
<i>Fig. 3.5</i> : drop casting of NCs suspension on glass substrate and samples after solvent evaporation	73
<i>Fig. 3.6</i> : bandgap energy of CdS NCs as a function of heat treatment time, for different temperatures	74
<i>Fig. 3.7</i> : schematization of apparent bandgap decrease with increasing NC size	75
<i>Fig. 3.8</i> : Arrhenius plot for bandgap energy variation (initial, linear part) in CdS NCs	75

<i>Fig. 3.9</i> : bandgap of CdSe-CdS NCs as a function of heat treatment time, for different temperatures	76
<i>Fig. 3.10 (left)</i> : band offset in a CdSe-CdS heterojunction	77
<i>Fig. 3.10 (right)</i> : schematization of apparent bandgap decrease with CdS shell merging together	77
<i>Fig. 3.11</i> : Arrhenius plot for bandgap energy variation in CdSe-CdS NCs	77
<i>Fig. 3.12</i> : bandgap energy (plot) and proposed nanostructure evolution (sketched) at 400 °C	78
<i>Fig.3.13</i> : example of Schottky junction with QD-based nano-heterostructured material	79

List of Tables

<i>Table 1.1</i> : crystal structures and values of a , c , ρ and E_G of II-VI semiconductor evaluated in this work	17
<i>Table 1.2</i> : typical zinc and cadmium precursors formulations	18
<i>Table 1.3</i> : typical chalcogen precursors formulations	19
<i>Table 1.4</i> : typical synthesis parameters for single-phase NCs	20
<i>Table 1.5</i> : typical synthesis parameters and nominal shell thickness range for multi-phase NCs	21
<i>Table 1.6</i> : crystal structure, crystal density, lattice parameters and ML thickness	25
<i>Table 1.7</i> : values of E_G , E_{CB} , E_{VB} , m_e^* , m_h^* and ϵ used in this work	25
<i>Table 1.8</i> : 1 st absorption peak wavelength and size range for synthesized single-phase NCs	26
<i>Table 1.9</i> : fluorescence wavelength range for synthesized core-shell NCs	28
<i>Table 1.10</i> : composition, precursor ratio, fluorescence λ , shape and size of synthesized alloyed NCs	37
<i>Table 3.1</i> : crystal structure, effective lattice constant, bandgap energy and bands position	69

INTRODUCTION

Motivation and relevance

Materials engineering at the nanometer scale, where many physical phenomena have natural length, is gaining an increasing attention from many scientific fields.

A “quantum dot”, defined for the first time at the beginning of 1980s by Ekimov¹, is a semiconductor crystal of nanoscopic size, whose excitons are confined in all three spatial dimensions. As a consequence of this confinement, its electronic structure can be tuned by varying the size of the crystal: the gap between the Highest Occupied Molecular Orbital (HOMO) and the Lowest Unoccupied Molecular Orbital (LUMO) widens with decreasing crystallite size^{2,3} (phenomenon known as “size-dependant bandgap”). Thanks to this phenomenon, semiconductor nanocrystals exhibit very interesting size-dependent optoelectronic properties that cannot be achieved by their bulk counterparts⁴.

In 1993, Murray, Noms and Bawendi³ pioneered the synthesis of monodisperse nanoparticles in a coordinating solvent. Synthesis techniques have then developed, and nowadays semiconductor nanocrystals can be obtained by relatively simple and cheap methods via colloidal green chemistry. Colloidal synthesis of semiconductor nanostructures have developed from preparation of simple objects (like single-phase, spherical nanoparticles) toward more and more sophisticated structures where size, composition and shape of a multicomponent structure can be tailored in an independent manner². The use of these multicomponent nano-heterostructures provides an interesting opportunity to design optoelectronic properties through electron and hole wavefunction engineering⁵.

Nanocrystals can self-assemble from colloidal solutions into ordered structures (superlattices)⁶: assembling nanocrystals into solids opens up the possibilities of fabricating new solid-state materials and devices with novel physical properties, as interactions between proximal nanoparticles give rise to new collective phenomena. Solution-based processes such as spin coating, dip coating or drop casting can reduce the fabrication costs of optoelectronic devices based on these superlattices. However, realizing solid state optoelectronic application using such nano-sized building blocks has been, so far, a challenging objective.

The first chapter of this thesis introduces synthesis, characterization and properties simulation of some II-VI semiconductor nanocrystals and nano-heterostructures. This part of the work was propaedeutic to understand key relationships between synthesis parameters, dimensions, composition, surface ligands and optical properties of nanocrystals, that were used as “building blocks” to develop novel materials for the applications presented later in the thesis.

The second and third chapters of this work explore two possible optoelectronic applications of these nanocrystals. Two major energy-related problems are approached: energy efficiency and energy conversion. In recent years, due to growing energy demand and depletion of conventional energy sources, research efforts are focusing on improving efficiency of existent devices as well as finding new and clean energy conversion technologies.

The second chapter of this thesis addresses to efficiency improvement, focusing on application of semiconductor nanocrystals to illumination devices. Nowadays, conventional light sources such as incandescent bulbs, are known for their low efficiency. Among possible replacements for conventional light sources, Light Emitting Diodes (LEDs) are very promising, thanks to their high efficiency, reliability and long life time ⁷. However, even if commercial LEDs are available in a broad range of pure colors (being the color of emitted light related to the bandgap E_G of the semiconductor used), mixed colors, as white, require combining at least two pure colors ⁸. A possible solution is to combine UV or blue emitting LED with phosphors ^{9,10}: the LED is used as the optical excitation source; some of its light is absorbed by the phosphors, that re-emit shorter frequencies light (green, yellow, red), producing white light. This approach seems to be promising for the development of simple and cost effective white lighting devices. In commercial available devices, generally a blue emitting gallium nitride (GaN) LED and cerium-doped yttrium-aluminum granate (YAG : Ce⁺³) are used as excitation source and yellow phosphor respectively ^{7,11}. This mixture of blue and yellow produces white light; however, the color rendering index is sometimes low, due to the lack of red emission, and the color purity varies with input power ⁷. To overcome these problems, near-UV InGaN emitters can be used ^{10,12}, and different typologies of phosphors have been evaluated. Instability and narrow absorption properties of organic phosphors and broad emission spectra of inorganic ones makes sometimes difficult to access precisely the desired colors ⁸. Semiconductor nanocrystals have attracted considerable attention as promising candidates, thanks to their size-tunable emission color, high fluorescence quantum yield, narrow emission spectrum (FWHM \approx 30 nm compared to 50-100 nm of inorganic phosphors ¹³) and broad absorption spectrum ^{7,8}. This last feature (high density of absorbing states from their bandgap to UV region) permits the simultaneous excitation of different wavelength-emitting phosphors with a single light source. Several groups ^{7,8,14,15} showed the possibility to incorporate semiconductor nanocrystals inside a polymeric matrix. Research work presented in the second chapter of this thesis concerns the development of a composite material (nanocrystals inside polymeric matrix) as a promising candidate for down-converting phosphors, to be coupled with a LED (used as the optical excitation source) to obtain a cost effective white lighting device.

The third chapter of this thesis presents a possible application of semiconductor nanocrystals to an existing energy conversion technology: photovoltaic devices. Nowadays, low efficiency and high cost limit the diffusion of photovoltaic as prominent energy conversion technology. All photovoltaic conversion processes are based on two necessary mechanisms: absorption of photons (associated with generation of charge carriers) and extraction of the charge carriers to an external electrical circuit, where they can be used to produce work. One of the major intrinsic limitations of photovoltaic

converters is associated to the absorption step, since the solar spectrum cannot be utilized efficiently. Single-junction photovoltaic devices utilize one semiconductor material (characterized by an energy bandgap E_G) as absorbent: photons with energy lower than E_G are lost (because their energy is too low to enable absorption); on the other hand, photons with energies higher than E_G waste their excess energy as heat. Quantitatively, the maximum single-junction cell efficiency is expressed by the Shockley-Queisser limit¹⁶, which is about 31% for an optimal E_G . A possible way to bypass this limitation is to develop an absorbent material presenting an electrically isolated, half-filled electronic band (known as “intermediate band”), located within the semiconductor bandgap. The “intermediate band” and its working principles were originally theorized by Luque and Martí in 1997¹⁷. The presence of such band leads to the generation of one extra electron-hole pair when two below-bandgap photons are absorbed¹⁷; this electron-hole pair adds to those produced conventionally by photons with energy higher than E_G , increasing the photogenerated current. It can be shown that the voltage supplied by the cell is still limited by the CB-VB bandgap and not by any of the lower bandgaps¹⁸, increasing the solar cell photocurrent without degrading its voltage¹⁹. The limiting conversion efficiency of an intermediate band solar cell could reach 47% at 1 sun (about 63% at full solar concentration^{17,20}), comparing with 43% of a two bandgap tandem solar cell at 1 sun (55% at full solar concentration). Semiconductor nanocrystals have been proposed to implement an intermediate band material^{19,21-23}. In a three dimensional, ordered array of semiconductor nanocrystals (referred as “quantum dots”), located inside another, higher bandgap semiconductor (referred as “barrier” or “host material”), an intermediate electronic band would arise within the bandgap of the barrier material from the confined electronic states of the quantum dots; delocalization of the electrons in the intermediate band could be achieved by increasing the dots density until the electron wave functions have significant overlap and become delocalized¹⁸. This geometry is known as “quantum dots supracrystal”; there have been already a number of reported tridimensional ordered quantum dot supracrystals grown by molecular beam epitaxy²⁴⁻²⁶; it has been only under this approach that, so far, working intermediate band solar cells have been manufactured^{27,28}. The research work presented in the third chapter of this thesis considers an alternative, novel approach to obtain such complex nano-geometry by a simple, cost effective method. Starting from colloidal synthesized core-shell semiconductor nanocrystals (obtained at near-ambient temperature and pressure), the desired quantum dot supracrystal is obtained by self-assembly of nanocrystals from colloidal solution and subsequent application of a heat treatment conceived to sinter the external shell material while preserving the nano-heterostructure.

Thesis overview

This thesis is divided into three main chapters.

Chapter 1 This chapter introduces semiconductor nanocrystals and their peculiar optical properties. Then it describes synthesis protocols of different typologies of nanocrystals (single-phase, alloyed and complex heterostructures), through a common, green chemistry system (one solvent and two stabilizing ligands). Optical characterization techniques, ligands exchange procedures and bandgap simulation of complex nano-heterostructure via effective-mass approximation are presented. Results are shown and discussed in the final part of the chapter.

Chapter 2 This chapter deals with the development of a composite material (nanocrystals inside polymeric matrix) as a promising candidate for a phosphor to be coupled with a LED (used as the optical excitation source) to obtain a cost effective white lighting device. The chapter first introduces basic Light Emitting Diodes concepts; then it concentrates on optimization of nanocrystals optical properties (absorption spectra, emission wavelength and fluorescence quantum yield) and their relations with nanostructure and surface ligands.

Chapter 3 This chapter presents an alternative, novel approach to obtain a nanostructured multiphase material (semiconductor nanocrystals enclosed into a wider bandgap semiconductor) through a simple, cost effective method: self-assembly of core-shell nanocrystals followed by application of a heat treatment conceived to sinter the external shell material, while preserving the nano-heterostructure. This novel material should be characterized by an electronic intermediate band. The chapter first introduces basic concepts of intermediate band materials and intermediate band solar cells based on quantum dots; then it presents the proposed realization scheme. Experimental details of nanocrystals assemblies, heat treatments and nanostructure evolution monitoring through fluorescence spectroscopy are also described; results are presented and discussed in the final section of the chapter.

References

- (1) Ekimov, A. I.; Onushchenko, A. A. *Journal of Experimental and Theoretical Physics* **1981**, *34*, 345-348.
- (2) Talapin, D. V.; Lee, J.-S.; Kovalenko, M. V.; Shevchenko, E. V. *Chemical Reviews* **2010**, *110*, 389-458.
- (3) Murray, C. B.; Noms, D. J.; Bawendi, M. G. *Journal of American Chemical Society* **1993**, *115*, 8706-8715.
- (4) Park, J.; Joo, J.; Kwon, S. G.; Jang, Y.; Hyeon, T. *Angewandte Chemie (Int. Ed.)* **2007**, *46*, 4630-60.
- (5) Balet, L. P.; Ivanov, S. a; Piryatinski, a; Achermann, M.; Klimov, V. I. *Nano Letters* **2004**, *4*, 1485-1488.
- (6) Murray, C. B.; Kagan, C. R.; Bawendi, M. G. *Annual Review of Materials Research* **2000**, *30*, 545-610.
- (7) Chung, W.; Park, K.; Yu, H. J.; Kim, J.; Chun, B.-H.; Kim, S. H. *Optical Materials* **2010**, *32*, 515-521.
- (8) Lee, J.; Sundar, V. C.; Heine, J. R.; Bawendi, M. G.; Jensen, K. F. *Advanced Materials* **2000**, *12*, 1102-1105.
- (9) Lee, S.; Seo, S.-Y. In *Proceedings of SPIE*; SPIE, 2001; Vol. 4445, pp. 82-92.
- (10) Kim, J. S.; Jeon, P. E.; Park, Y. H.; Choi, J. C.; Park, H. L.; Kim, G. C.; Kim, T. W. *Applied Physics Letters* **2004**, *85*, 3696.
- (11) Steigerwald, D.; Rudaz, S.; Liu, H.; Kern, R. S.; Gotz, W.; Fletcher, R. *Jom* **1997**, *49*, 18-23.
- (12) Nakamura, S.; Mukai, T.; Senoh, M. *Applied Physics Letters* **1994**, *64*, 1687.
- (13) Sato, Y.; Takahashi, N.; Sato, S. *Japanese Journal of Applied Physics* **1996**, *35*, L838-L839.
- (14) Khanna, P.; Singh, N. *Journal of Luminescence* **2007**, *127*, 474-482.
- (15) Bomm, J.; Büchtemann, A.; Fiore, A.; Manna, L.; Nelson, J. H.; Hill, D.; Sark, W. G. J. H. M. van Beilstein *Journal of Nanotechnology* **2010**, *1*, 94-100.
- (16) Shockley, W.; Queisser, H. J. *Journal of Applied Physics* **1961**, *32*, 510.
- (17) Luque, A.; Martí, A. *Physical Review Letters* **1997**, *78*, 5014-5017.
- (18) Luque, A.; Martí, A.; Nozik, A. J. *MRS Bulletin* **2007**, *32*, 236-241.
- (19) Tomic, S.; Harrison, N. M.; Jones, T. S. *Optical and Quantum Electronics* **2008**, *40*, 313-318.
- (20) Luque, A.; Martí, A. *Progress in Photovoltaics: Research and Applications* **2001**, *9*, 73-86.
- (21) Tomic, S.; Jones, T. S.; Harrison, N. M. *Applied Physics Letters* **2008**, *93*, 263105.
- (22) Cuadra, L. *Thin Solid Films* **2004**, *451-452*, 593-599.
- (23) Shao, Q.; Balandin, A. A.; Fedoseyev, A. I.; Turowski, M. *Applied Physics Letters* **2007**, *91*, 163503.
- (24) Mazur, Y. I.; Ma, W. Q.; Wang, X.; Wang, Z. M.; Salamo, G. J.; Xiao, M.; Mishima, T. D.; Johnson, M. B. *Applied Physics Letters* **2003**, *83*, 987.
- (25) Springholz, G. *Science* **1998**, *282*, 734-737.
- (26) Kiravittaya, S.; Benyoucef, M.; Zapf-Gottwick, R.; Rastelli, A.; Schmidt, O. G. *Applied Physics Letters* **2006**, *89*, 233102.
- (27) Luque, A.; Martí, A.; Stanley, C.; López, N.; Cuadra, L.; Zhou, D.; Pearson, J. L.; McKee, A. *Journal of Applied Physics* **2004**, *96*, 903.
- (28) Martí, A.; Antolin, E.; Stanley, C.; Farmer, C.; Lopez, N.; Daaz, P.; Canovas, E.; Linares, P.; Luque, A. *Physical Review Letters* **2006**, *97*, 1-4.

CHAPTER 1

Synthesis and Characterization of II-VI Semiconductor Nanocrystals

This chapter introduces semiconductor nanocrystals and their peculiar optical properties. Synthesis protocols and characterization techniques are then described.

Key theoretical features are presented in the introduction (paragraphs 1.1 - 1.5); experimental procedures adopted in synthesis, ligands exchange, simulation and characterization are described in the experimental section (paragraphs 1.5 – 1.8); finally, results and conclusions are presented and discussed (paragraphs 1.9 - 1.10).

Introduction

Defined for the first time at the beginning of 1980s by Ekimov¹, a semiconductor nanocrystal (NC) is a nanometric sized crystal of a semiconductor material, whose excitons are confined in all three spatial dimensions. Consequently, its electronic structure can be tuned by varying its size, leading to a phenomenon known as the “size-dependent band gap”²: the energy between Highest Occupied Molecular Orbital (HOMO) and Lowest Unoccupied Molecular Orbital (LUMO) widens with decreasing crystallite size^{2,3}.

1.1 Optical Properties of Semiconductor Nanocrystals

1.1.1 The quantum confinement effect

The size dependence of optical properties is determined by the degree of spatial confinement of the electronic wave function⁴, which depends on relation between the size and the exciton Bohr radius. A NC of a given semiconductor material is considered a “quantum dot” (QD) if its size is smaller than the exciton Bohr radius of the respective bulk semiconductor⁵. Under this size, it is possible to tune continuously the energy bandgap (E_G), therefore controlling the emission color or the absorption onset⁵. Another typical feature of QDs is the discrete structure of energy levels (termed “quantum size levels” – QSLs), replacing the continuous energy bands of a bulk material⁵. In a spherical QD, surrounded by an infinite potential barrier, the energy of the QSLs (characterized by angular momentum quantum number l) can be written in parabolic approximation as⁶:

$$E_{l,n}^{e,h} = \frac{\hbar^2 \phi_{l,n}^2}{2m_{e,h}d^2} \quad (1.1)$$

where $m_{e,h}$ are the electron and hole effective masses, d is the crystal size and $\phi_{l,n}$ are the n^{th} root of spherical Bessel function of order l . A typical absorption spectrum and QSLs of a QD are shown in Fig. 1.1.

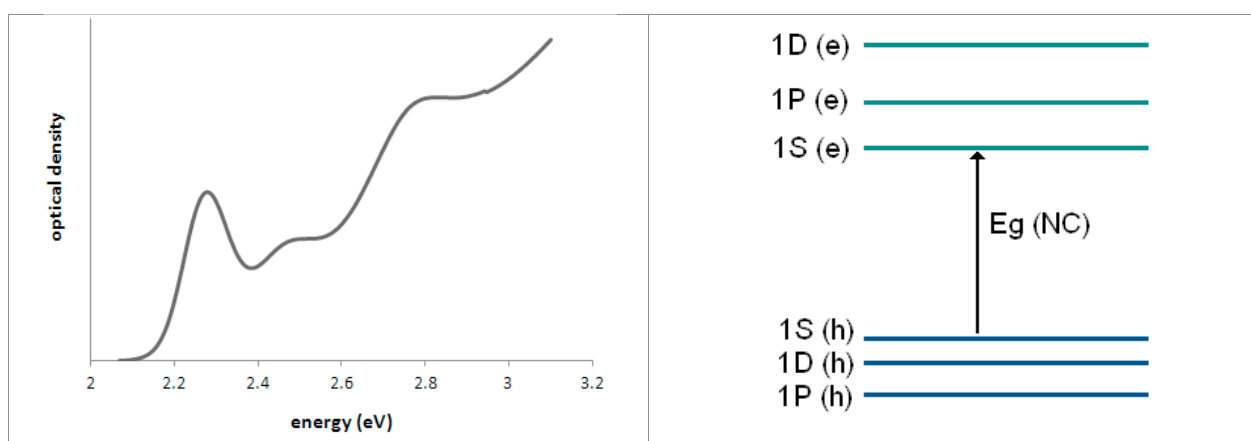


Fig. 1.1: typical absorption spectrum of a “quantum dot” (left) and QSLs (right) - freely adapted from Klimov⁵

1.1.2 Electron quantum state levels

In the case of a spherical QD, in the absence of band-mixing effects, conduction band originates an independent series of electron quantized states, that can be described using two quantum numbers^{4,5}: L (the angular momentum, related to the symmetry) and n (the number of the state in the series of a given symmetry). In the typical notation of quantized states, the angular momentum is indicated by a letter (S for $L=0$, P for $L=1$ and so on) and is preceded by the value of n . Electron quantum state levels are therefore written as " nL "; in order of increasing energy, the three lower states are: $1S$, $1P$ and $1D$.

1.1.3 Hole quantum state levels

Because of the more complex, multi sub-band situation of the valence band, hole quantized states are better described considering the total angular momentum F ^{4,5,7}, equal to the sum of the orbital momentum of the hole envelope function, L , and the Bloch function angular momentum J . Hole quantum state levels can be written as " nL_F "; the three lowest hole states are $1S_{3/2}$, $1P_{3/2}$ and $2S_{3/2}$.

1.1.4 Interpretation of a quantum dot absorption spectrum

A typical QD absorption spectrum and some possible electronic transitions are shown in Fig. 1.2. The $1S(e)-1S_{3/2}(h)$ transition is considered the "band-edge" transition. Transitions to the $1S(e)$ and $2S(e)$ electron levels are also possible from $nS_{2/3}(h)$ and $nS_{1/2}(h)$ hole quantum state levels⁷. Similar considerations apply to P and D allowed transitions (for a complete coverage of this topics, further readings of Ekimov^{1,7}, Efros⁴ and Klimov⁵ works are suggested).

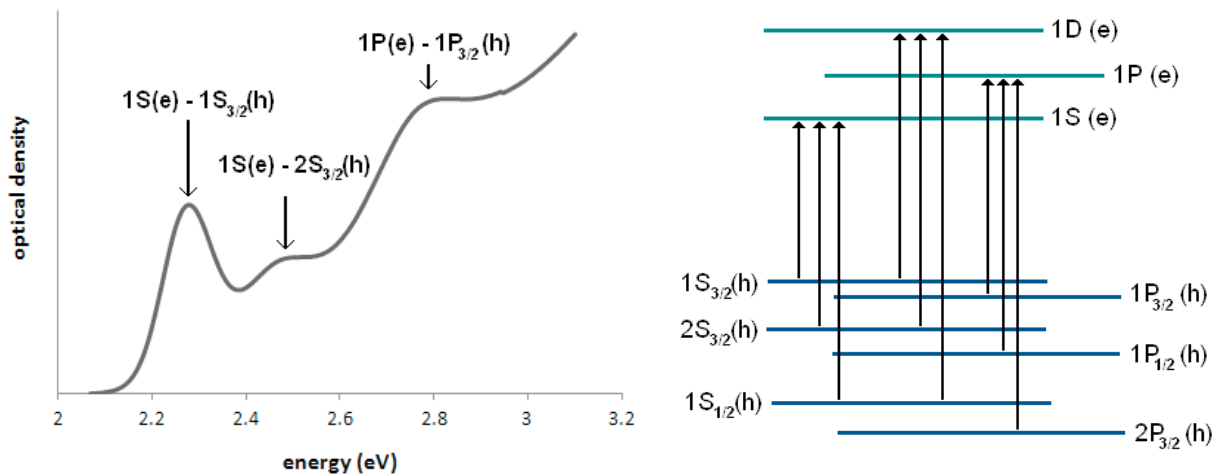


Fig. 1.2: left: CdSe NC absorption spectrum, with arrows marking the positions of well resolved transitions; right: allowed interband optical transitions (freely adapted from Klimov⁵)

1.1.5 Emission Stokes shift

Another distinctive feature of semiconductor NCs optical properties is the red-shift of the emission peak respect to the absorption band-edge, known as Stokes shift. The shift decreases with increasing the NC radius, and disappears beyond a certain radius. According to Bagga et al.⁸, the red-shift is caused by the splitting of the exciton states by the electron-hole exchange interaction: after absorption, the exciton in the singlet state first thermalize to a triplet state, from where it deexcites to the original state, giving rise to a Stokes shift equal to the energy difference between the singlet and triplet states.

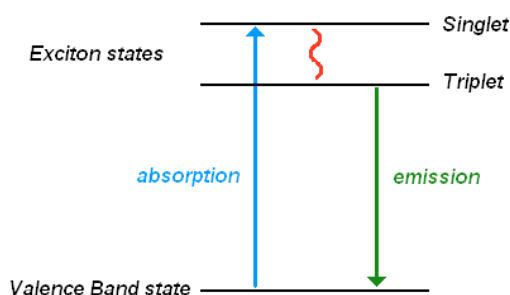


Fig. 1.3: schematic representing of excitation-deexcitation taking place at the band edge (adapted from Bagga et al.⁸)

1.1.6 Fluorescence quantum yield

In semiconductor nanocrystals, high fluorescence quantum yield (defined as the ratio of photons emitted through fluorescence to photon absorbed) is achieved by maximizing the probability of band-edge recombination; this is made difficult by the numerous, competing process that may occur after the generation of an exciton inside the nanocrystal:

- (i) one of both charge carriers may be trapped in surface states⁹
- (ii) scavenged by redox species¹⁰ (if in solution)
- (iii) become trapped on local defect sites¹¹ (if in a solid matrix)

In addition, electrons may undergo radiative or auger-assisted ionization, leading to non-radiative recombination or permanent oxidation of the nanocrystal¹². Surface states originate from surface atoms not completely incorporated into the lattice, possessing orbitals that are capable of accepting or donating electrons. These orbitals (or dangling bonds) exhibit a range of energy levels that lie within the bandgap, providing non-radiative recombination pathways¹³, competing with band-edge luminescence. Passivation of these traps with appropriate surface ligands has been shown to greatly enhance the luminescence quantum yields of nanocrystals¹⁴; unfortunately, because of steric consideration, the organic ligands have packing densities way lower than those of surface atoms¹⁵. In principle, an epitaxial grown inorganic shell (see paragraph 1.2.2), completely eradicate surface traps, and also reduces the probability of the other side processes that may compete with band edge radiative recombination⁹.

1.2 Classification of Nanocrystals

1.2.1 Single phase nanocrystals

These are the simplest NCs, consisting of only one-phase semiconductor¹⁶. As a consequence of their size-dependent bandgap, the size of single-phase NCs can be related to their first exciton energy. In spherical NCs, the relation between radius r and bandgap E_G^{NC} can be expressed using the formula from Brus et al.⁶, through an effective mass approximation:

$$E_G^{NC} = E_G^{bulk} + \frac{\hbar^2}{2r^2} \cdot \left(\frac{1}{m_e^*} + \frac{1}{m_h^*} \right) - \frac{1}{r} \cdot \frac{1.8e^2}{\epsilon} \quad (1.2)$$

where E_G^{bulk} is the bandgap of the bulk material, m_e^* and m_h^* are electron and hole effective masses, \hbar the Planck's constant, e the elementary charge and ϵ the absolute permittivity of bulk material.

1.2.2 Multi-phase nanocrystals (core-shell or core-multishell)

Core/shell NCs (defined also as “nano-heterostructures”) contain at least two semiconductor materials arranged in an onion-like structure¹⁶. Since optical properties of core/shell NCs depends both on the core and the shell sizes and composition, hypothetical curves that relate D or ϵ with dimensions become multiple-variables functions, and are generally not available in literature. Growing an epitaxial shell provides a physical barrier between the inner “core” and the surrounding medium, making NCs less sensitive to surface chemistry and photo-oxidation. It makes also possible to tune their absorption/emission energies and their quantum yield¹⁷. The relative band edges of the two material determine the properties of the resultant core-shell NCs; different combinations of core-shell materials result in nano-heterostructures that fall within two main categories^{9,17}:

- a) *Type-I* structures: the bandgap of the shell material is larger than that of the core; both electrons and holes are confined in the core. Type-I nanocrystal are the ideal choice to achieve high QY, since they provide the greatest probability of band-edge charge recombination.
- b) *Type-II* structures: either the valence-band edge or the conduction band edge of the shell material is located inside the bandgap of the core. Upon photoexcitation of the NC, this staggered band alignment leads to a spatial separation of the charge carriers in different regions of the core-shell structure¹⁷; this reduces the overlap of the electron and hole wavefunctions and lengthens the lifetime of the excited state¹⁸, rising the probability that the unconfined charge carrier will be trapped or scavenged⁹. Therefore, Type-II nanocrystals exhibit low quantum yields and they can be extremely sensitive to local environment.

Other categories can be defined as:

- c) *inverted Type-I*¹⁷: the bandgap of the shell material is smaller than that of the core; depending on the thickness of the shell, the charge carriers are partially or completely confined in the shell.
- d) *quasi Type-I*¹⁹: one charge carrier is confined in the core (or in the shell), the other one is delocalized over the entire nano-heterostructure.

It is useful to point out that the relative band edges in a core-shell nanostructure changes in function of both the core and shell dimensions, since the alignment of quantized energy states is determined not only by bulk material energy offsets but also by confinement energies. Therefore, it can be possible to switch between Type-I and Type-II regime also by varying the dimensions of the system^{20,21}, in addition to its chemical composition.

1.2.3 Alloyed nanocrystal

The formation of an alloyed structure is an alternative way to influence the bandgap of NCs, changing their composition instead of their size. According to van Embden⁹, alloying is more simple if the anions of the different semiconductors are the same, since this allows efficient diffusion of the smaller cations between tetrahedral interstitial sites. A typical example is $\text{Cd}_{1-x}\text{Zn}_x\text{Se}$, corresponding to CdSe NCs, in which a fraction of Cd atoms is substituted by Zn ones in the crystal lattice. The bandgap of this ternary compound will be between those of pure CdSe and pure ZnSe^{22,23}, according to Vegard's law:

$$E_G^{\text{Cd}_x\text{Zn}_{1-x}\text{Se}} = xE_G^{\text{CdSe}} + (1-x)E_G^{\text{ZnSe}} - b(1-x) \quad (1.3)$$

where E_G^{CdSe} and E_G^{ZnSe} are the bandgaps of bulk CdSe and ZnSe, respectively. This curve shows a deviation from linear behavior, known as "bowing parameter" b , which depends on the difference in electronegativity of the two components. The difference is not very pronounced in common anion systems^{24,25} (such as $\text{Cd}_{1-x}\text{Zn}_x\text{Se}$ or $\text{Cd}_{1-x}\text{Zn}_x\text{S}$), while is more relevant in common cation compounds²⁶ (such as $\text{CdSe}_{1-x}\text{S}_x$ or $\text{CdTe}_{1-x}\text{Se}_x$), that consequently present larger bowing parameters.

1.3 Colloidal synthesis

A colloidal synthesis generally involves several consecutive stages²: (i) a nucleation from an initially homogeneous solution; (ii) growth of the pre-formed nuclei; (iii) isolation of the particles from the reaction mixture; (iv) possible post-preparative treatments.

1.3.1 Nucleation theory

Classic studies by La Mer²⁷ show that production of a monodisperse colloid requires a temporally discrete nucleation event followed by a slower, controlled growth on the existing nuclei. In this process, many nuclei are generated at the same time; then these nuclei start to grow without additional nucleation. The final size distribution will be determined by the time over which the nuclei are formed and begin to grow:

- (i) If the growth of the particles during the nucleation is negligible compared with subsequent growth (all the particles nucleate almost simultaneously), their growth history will be nearly the same, and their final size would be more uniform^{28,29}
- (ii) If the nucleation process persists throughout the growth of the particles, their growth history will differ largely one from another, and the control of the final size distribution will be more difficult²⁸.

A LaMer plot ²⁷ (shown in Fig. 1.4) is useful to visualize how the energy barrier works to induce a “burst nucleation”. The energy barrier to the homogeneous nucleation can be thermodynamically interpreted as follows : the Gibbs free energy change ΔG for the formation of a spherical crystals with radius r is given by: ^{27,28,30}

$$\Delta G = 4\pi r^2 \gamma + \frac{4}{3}\pi r^3 \Delta G_V \quad (1.4)$$

where γ is the surface free energy per unit area (always positive) and $\Delta G_V = -RT \ln S/V_m$ is the free energy change between the monomers in solution and unit volume of bulk crystal ²⁸ (negative, as long the solution is supersaturated). A plot of ΔG_V versus r has a maximum ($d\Delta G/dr = 0$), called the critical radius r_c , which is the minimum radius of a particle that can grow spontaneously in the supersaturated solution:

$$r_c = \frac{2\gamma V_m}{RT \ln S} \quad (1.5)$$

where V_m is the molar volume of the bulk material and S the supersaturation of the solution. This imposes the first necessary condition for homogeneous nucleation: S should be sufficient high (concentration higher than concentration “ C_I ” in Fig. 1.4) to have a r_c smaller than the size of the crystal embryos that form the nuclei for the nucleation process ^{28,31}.

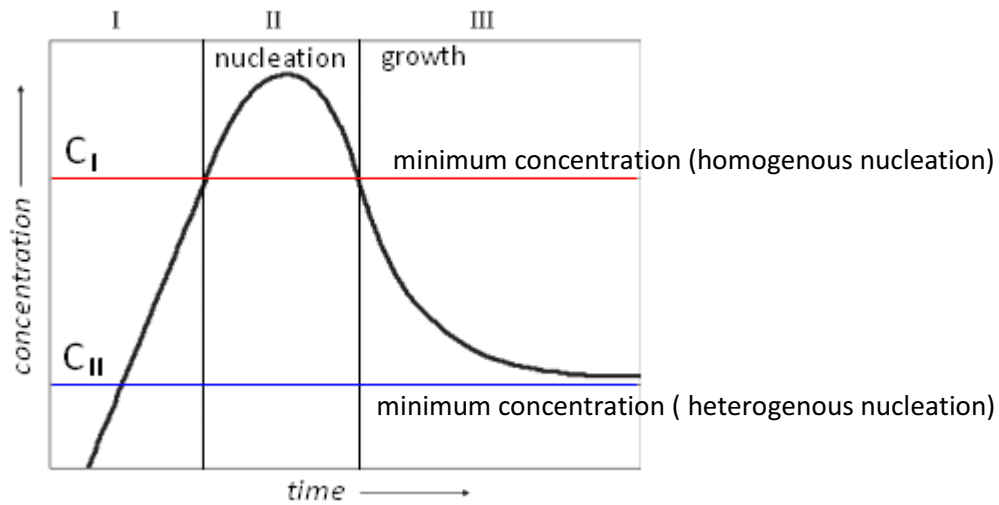


Fig. 1.4: LaMer plot (freely adapted from Park et al. ²⁸ and LaMer & Dinegar ²⁷)

In homogeneous nucleation process, nuclei appear in an homogenous solution without any seed for heterogeneous nucleation; the thermodynamic barrier required for that process is higher than that required for heterogeneous nucleation, due to the absence of foreign objects or phase boundaries that could lowers the effective surface energy contribution. Therefore, heterogeneous nucleation (i.e. growth of material on pre-existing nuclei) can occur at a lower supersaturation (concentration labeled “ C_{II} ” in Fig. 1.4) and/or lower temperature than homogeneous nucleation ^{19,30}. Heterogeneous nucleation has a lower ΔG :

$$\Delta G (hetero) = \Delta G (homo) \times f(\theta) \quad (1.6)$$

where θ is the contact angle between the nucleating crystal and the existing surface, depending on the ability of the growing material to wet the substrate (increasing with decreasing interfacial tension). In solid-solid interfaces, interfacial tension is related to lattice mismatch between the two materials; therefore, heterogeneous nucleation will be more simple if the lattice mismatch between the growing and the existing material is small.

1.3.2 Nanocrystals synthesis techniques

There are basically two typologies of synthetic routes²⁸ to obtain colloidal NCs:

- (i) “Hot-injection” techniques. First introduced by Bawendi group³, produce a high degree of supersaturation by a rapid injection of precursors into a hot solution, that raises the monomer concentration above the homogeneous nucleation threshold. During the rapid nucleation process, the monomer concentration sharply decreases and the nucleation rate slows down. As long as the consumption of the precursor is not exceeded by the rate of precursor addition, no new nuclei form²⁹ (only heterogeneous nucleation on pre-existing nuclei). These methods have been widely used to synthesize high quality semiconductor NCs³², but also transition³³ and noble metals³⁴ nanoparticles.
- (ii) “Heating-up” techniques. In these methods the precursors, the reagents and the solvent are mixed at low temperature; the reaction vessel is then heated to a certain temperature to initiate the crystallization reaction. These synthetic procedures are usually simpler than hot-injection methods, and are particularly advantageous for large scale production^{35,36}.

1.3.3 Core-shell nanocrystals synthesis techniques

For multi-phase, core-shell NCs, synthetic routes become more complex. High quality shells can be obtained by slow epitaxial growth on pre-existing “core” NCs. Some general rules^{17,19} can be applied to different techniques:

- (i) lattice mismatch between shell and core materials should be as small as possible (especially if thick shell are desired)
- (ii) growth temperature should be low enough to avoid homogenous nucleation of shell material and alloying between core and shell material, but high enough to allow growth of shell material on core seeds
- (iii) shell precursor addition rate should be low enough (according to precursor reactivity) to avoid high shell monomer concentration that could lead to homogenous nucleation of shell material

Core-shell synthesis techniques can be differentiate (A) by number of steps required or (B) by precursor addition method:

(A) Classification by number of steps required:

- (A1) *Multiple step* approach^{17,37-40}. This method involves an initial synthesis of the “core” NCs (“core synthesis” step), that are then washed to remove unreacted precursors and byproducts (“purification” step), before the addition of shell precursors (“shell growth” step).
- (A2) *Single step* approach⁴¹. This technique involves the addition of the shell precursors to the cores growth solution without intermediate washing. It provides a relatively simple route to core-shell NCs, but the composition and tunability of the shell thickness is difficult to control⁹.
- (A2a) *Single injection of multiple (more than two) precursors*^{42,43}. All the precursors (core and shell) are injected simultaneously. Depending on different precursor reactivity, core-shell, graded composition or alloyed NCs may be synthesized.

(B) Classification by method of precursor addition:

- (B1) *Injection* techniques^{9,32,40,44,45}. Shell precursor are added at a well defined rate to the previously prepared cores. The injection rate is slow (frequently dropwise - for example by means of a syringe pump) in order to prevent homogeneous nucleation of the shell material; growth temperature is generally kept as low as possible, to avoid alloying between core and shell materials⁹.
- (B1a) *Successive Ion Layer Adsorption and Reaction (SILAR)*^{20,39,46,47}. First used by Li et al.⁴⁷, in this particular injection technique pre-calculated amounts of shell precursors are injected alternately, allowing each atomic layer to be deposited separately with almost monolayer control on shell thickness⁹. The SILAR method reduces the coexistence of the shell’s cations and anions in solution, lowering the possibility of homogeneous nucleation; it also allows to monitor accurately the evolution of optical properties. Finally, this technique generally generates narrower size distribution and allows to synthesize a wide range of heterostructure (i.e. multi-shells⁴⁷).
- (B2) *Non-injection* techniques. All the shell precursors are added to the cores at room temperature, then the solution is heated to the desired reaction temperature. If the reaction parameters are well chosen and controlled, the shell material nucleate heterogeneously on the pre-existing cores instead of creating independent NCs of a second material. This approach simplify a lot the synthesis of multiphase NCs, but not all systems are suitable for this synthetic route.

1.3.4 II-VI semiconductor nanocrystals synthesis

II-VI semiconductors compounds consist, as the name suggests, of a II group metal and a IV group chalcogen. In 1993, Murray, Noms and Bawendi³ pioneered the synthesis of monodisperse cadmium-based NCs using pyrophoric dimethyl cadmium and trioctylphosphine chalcogenides in a coordinating solvent (trioctylphosphine oxide). Synthesis techniques have then developed, and nowadays cadmium sulfide, cadmium selenide, and cadmium telluride NCs can be easily obtained in non coordinating, less expensive solvents, with a wide range of safe, quasi non-toxic precursors and stabilizing ligands⁴⁸⁻⁵³. Also zinc chalcogenide NCs can be obtained from similar precursors, but the operative window

appears to be much narrower than that of corresponding cadmium compounds⁵⁴. Usually, II-VI semiconductor NCs are synthesized in high boiling point hydrocarbon, such as octadecane or 1-octadecene; commonly used precursors are carboxylate-metal complexes (such as cadmium or zinc oleate, laureate or stearate) and chalcogen-alkylphosphines complexes (such as trioctylphosphine sulfide, selenide or telluride). Liu et al.⁵⁵ proposed reaction pathways (shown in Fig. 1.5) for colloidal synthesis of CdSe NCs. Similar pathways apply also to other metal-chalcogenide NCs synthesis.

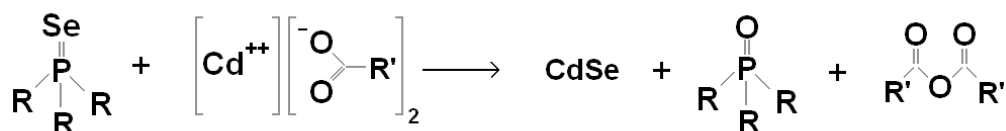


Fig. 1.5: proposed reaction pathways in colloidal synthesis of CdSe NCs (freely adapted from Li et al.)

R = octyl or butyl group; R' = CH₃-(CH₂)₆-CH = CH-(CH₂)₇-CH₃

1.4 Surface Ligands

The surface ligands play a key role in nucleation and growth processes. They also determine the solubility of the NCs in various media, affect their ability to form long range assemblies and modify their charge transport and photophysics properties^{2,56}.

1.4.1 Synthesis ligands

Most synthetic routes to high quality NCs with tunable sizes and shape utilize long hydrocarbon molecules containing a coordinating headgroup (typically carboxylic acids, amines and phosphines) as ligands²⁸, which sterically stabilize nanocrystals in non-polar solvents⁵⁷. The presence of these long, insulating molecules creates a barrier around each NC and blocks the access of other species to the nanocrystal surface^{2,57,58}.

1.4.2 Ligand exchange

Original, bulky ligands can be replaced with different ones for several reasons: for example, to make NCs soluble in different media (i.e. water instead of n-hexane) or to improve charge transport. A typical ligands exchange procedure involves an exposure of colloidal NCs to a large excess of competitive ligands, resulting in an exchange (partial or total) of original surface molecules². The procedure can be prolonged in time and/or repeated several times to maximize the removal of the original surface ligands. The process can be facilitated by using a two-phase mixture of polar and non-polar solvents to promote the phase separation of the different products². The degree of ligand exchange is usually assessed by Nuclear Magnetic Resonance (NMR), Infra Red spectroscopy (IR) or X-ray Photoelectron Spectroscopy (XPS).

Experimental Section

1.5 Synthesis

1.5.1 Semiconductor compounds used in this study

Cadmium sulfide (CdS), cadmium selenide (CdSe), cadmium telluride (CdTe), zinc sulfide (ZnS), zinc selenide (ZnSe) and their alloys were synthesized in the form of single and multi-phase nanocrystals. Crystal structures, lattice parameters a and c , crystal density ρ and energy bandgap E_G of bulk compounds are shown in table 1.1. Energy bandgaps, conduction and valence band positions (expressed as energy respect to the vacuum level) are graphically schematized in Fig. 1.6

compound	crystal structure	a (Å)	c (Å)	ρ (g/cm ³)	E_G (eV)
CdS ⁵⁹⁻⁶¹	wurtzite	4.14	6.72	4.821	2.48
	zinc-blende	5.83		4.855	2.42
CdSe ^{59,60}	wurtzite	4.30	7.01	5.662	1.75
	zinc-blende	6.08		5.664	1.67
CdTe ⁵⁹⁻⁶¹	zinc-blende	6.48		5.856	1.51
ZnS ^{59,60}	wurtzite	3.82	6.26	4.086	3.75
	zinc-blende	5.41		4.087	3.72
ZnSe ^{59,60}	zinc-blende	5.67		5.262	2.72

Table 1.1: crystal structures and values of a , c , ρ and E_G (at 300 K) of II-VI semiconductor evaluated in this work

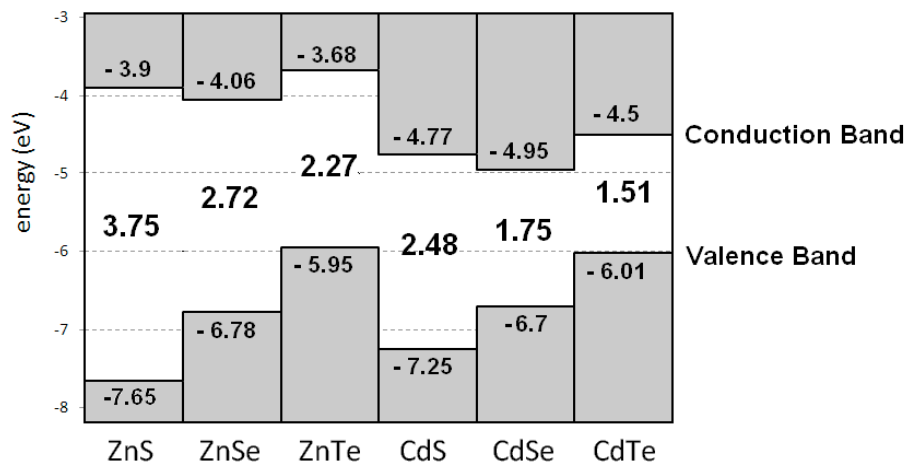


Fig. 1.6 bandgap energies, conduction and valence band positions (expressed as energy respect to the vacuum level) of II-VI compounds evaluated in this work (values from Adachi^{59,62,63})

1.5.2 Materials

Trioctylphosphine (TOP, 90%), oleic acid (OA, >93%), lauric acid (LA, >98%), octadecylphosphonic acid (ODPA, 97%), 1-octadecene (ODE, 90%), sulfur (S, >99%), selenium (Se, >99%), tellurium (Te, > 99%), cadmium acetate dihydrate (Cd-Ac, 98%), zinc acetate dihydrate (Zn-Ac, >98%), zinc stearate (Zn-SA, technical grade), methanol (>99.8%), acetone (>99,9%) were obtained from Sigma-Aldrich.

1.5.3 Precursor solutions preparation

All the following procedures were performed in inert atmosphere. Cadmium oleate (Cd-OA) and zinc oleate (Zn-OA) solutions were obtained heating Cd-Ac or Zn-Ac in ODE and OA at 250 °C for 30 minutes; zinc laureate (Zn-LA) solution was obtained heating Zn-Ac in ODE and LA at 250 °C for 30 minutes; cadmium octadecylphosphonate(Cd-ODPA)/cadmium oleate solution was obtained heating Cd-Ac in ODE, OA and ODPA at 250 °C for 30 minutes; Zn-SA solution was obtained heating Zn-SA in ODE at 100 °C for 30 minutes. Trioctylphosphine-chalcogenide solutions (trioctylphosphine sulfide, TOP-S; trioctylphosphine selenide, TOP-Se; trioctylphosphine telluride, TOP-Te) were obtained dissolving S, Se or Te powder in TOP and ODE by sonication and heating at 50°C for 10 minutes; phosphine-free chalcogenide precursor solutions (ODE-S and ODE-Se) were obtained dissolving S and Se powder in ODE at 50 °C and 200 °C respectively. Typical precursor formulations are shown in tables 1.2 - 1.3.

Zinc precursors					
	Zn-Ac	Zn-SA	OA	LA	ODE
ZnSe NCs	22 mg	-	0.15 ml	-	10 ml
	-	63 mg	-	-	
	22 mg	-	-	100 mg	
(shell) B*/ZnX	264 mg	-	0.8 ml	-	5.2 ml
	-	75 mg	-	-	6 ml

Cadmium precursors					
	Cd-Ac	OA	LA	ODPA	ODE
CdSe NCs	135 mg	0.4 ml	-	-	10 ml
	-	-	-	-	
	22 mg	-	0.8 ml	-	
CdS NCs	270 mg	0.6 ml	-	-	20 ml
CdTe NCs	54 mg	0.3 ml	-	20 mg	15 ml
(shell) C*/CdS	324 mg	0.8 ml	-	-	5.2 ml

Table 1.2: typical zinc and cadmium precursor formulations
(X* = Se or S; B* = CdSe or CdSe-ZnSe; C* = CdSe or CdTe)

Selenium precursors				
	Se	TOP	TBP	ODE
CdSe NCs	80 mg	0.5 ml	-	1.5 ml
	40 mg	-	-	20 ml
	40 mg	-	-	20 ml
ZnSe NCs	32 mg	0.1 ml		8 ml
(shell) B*/ZnSe	96	1 ml	-	5.4 ml
	96	-	0.6 ml	5.4 ml

Sulfur precursors				
	S	TOP	TBP	ODE
CdS NCs	32 mg	0.5 ml		1.5 ml
	32 mg	-	-	12 ml
(shell) C*/CdS	38 mg	1.5 ml	-	4.5 ml
(shell) Y*/ZnS	38 mg	1.5 ml	-	4.5
	38 mg	-	0.8 ml	5.2 ml

Tellurium precursors				
	Te	TOP	TBP	ODE
CdTe NCs	30 mg	0.2 ml	-	2 ml
	32 mg	-	0.1	2 ml

Table 1.3: typical chalcogen precursor formulations
(B* = CdSe; C* = CdSe or CdTe; Y* = CdSe, CdSe/CdS or CdSe/ZnSe)

1.5.4 Synthesis of single-phase nanocrystals

To synthesize monophasic NCs, both (i) *hot injection* (for all NC typologies) and (ii) *heating up* (only for CdS and ZnSe) techniques were used. Typical synthesis parameters for single phase NCs are shown in table 1.4.

General procedure – hot injection: solvent and first precursor were heated to the injection temperature T_{INJ} , then second precursor was injected and temperature was set to the *growth temperature* T_{GR} for the time t_{GR} .

General procedure – heating up: solvent and both precursors were mixed at room temperature, then reaction vessel was heated to T_{GR} kept at this temperature for t_{GR} .

compound	solvent	precursors	T_{INJ} (°C)	T_{GR} (°C)	t_{GR} (min)
CdS	ODE	Cd-OA TOP-S ODE-S	260 - 300	260 - 300	0 – 20
CdSe	ODE	Cd-OA TOP-Se ODE-Se	220 - 280	200 - 250	0 – 30
CdTe	ODE	Cd-OA Cd-ODPA TOP-Te	200 - 300	200 - 285	0 – 60
ZnSe	ODE	Zn-OA Zn-SA Zn-LA TOP-Se	290 - 320	290 - 310	0 – 60

Table 1.4: typical synthesis parameters for single-phase NCs

1.5.5 Synthesis of multi-phase nanocrystals

Typical synthesis parameters for multi-phase NCs (termed “core-shell”) are shown in table 1.5. These NCs were synthesized according two techniques:

- (1) *Precursor injection techniques - general procedure* (SILAR or not SILAR methods): a known volume of solvent was heated to the initial shell growth temperature (T_{s1}), then the previously synthesized and purified (= washed twice with methanol to remove unreacted species) core NCs (with a known size and concentration) were slowly introduced into the solvent. Sequential injections of pre-calculated amounts (determined as explained in paragraph 1.8.4) of shell precursors were performed: the first injection consisted of enough cation (in case of common anion systems) or anion (in case of common cation systems) precursor to cover the anion (cation) sites on the “core” nanoparticles surface. The following injections consisted in equimolar amounts of anion/cation precursors necessary to grow a concentric, 1-ML thick shells. This operation was repeated in order to grow a known number of MLs of shell material on the cores. The temperature was maintained at T_{s1} for the first layers, increased to a $T_{s2} > T_{s1}$ for the external layers, possibly without exceeding the alloying temperature T^* (determined by monitoring the absorption spectrum: when hypsochromic shifts were observed, core and shell materials were considered inter-diffusing into each other). Growth time was generally kept between 5 and 10 minutes (longer times for the external layers; time was determined by monitoring the absorption spectrum: when no major changes were observed, the shell layer reaction was considered complete).
- (2) *Heating up techniques, general procedure*: a known quantity of “core” nanocrystals were mixed at room temperature with a pre-determined quantity of shell precursors; then the solution was heated to the desired reaction temperature T_s . These typology of shell growth techniques were used only to synthesize “test” versions of CdSe-CdS and CdTe-CdS core-shells.

shell material	shell precursors	T_s (°C)	T^* (°C)	shell thickness range
ZnSe on CdSe	Zn-OA Zn-LA Zn-SA TOP-Se TBP-Se	200 - 240 °C	260 °C	0.28 – 1.5 nm (1 – 1.96 MLs)
CdS on CdSe	Cd-OA TOP-S ODE-S	240 - 270 °C	>300 °C	0.3 – 1.7 nm (1 – 5 MLs)
CdS on CdTe	Cd-OA Cd-ODPA TOP-S	250 - 270 °C	>300 °C	0.3 – 1.7 nm (1 – 5 MLs)
ZnS on CdSe-ZnSe	Zn-OA Zn-SA TOPS	250 °C	270 °C	0.3 (1 ML)
ZnS on CdSe-CdS	Zn-OA TOP-S	270 °C	unknown	0.3 (1 ML)

Table 1.5: typical synthesis parameters and nominal shell thickness range for multi-phase NCs.
(shell thickness was estimated according to paragraph 1.8.4)

1.6 Diffusion Experiments

1.6.1 Materials

Methanol (>99.8%), acetone (>99.8%), 1-octadecene (ODE, 90%) were obtained from Sigma-Aldrich; heat transfer fluid (Terminol-66) was obtained from Dow Chemical Company. CdSe-ZnSe and CdSe-CdS core-shell NCs were synthesized according to procedures described in previous paragraphs.

1.6.2 Samples preparation

Core-shell NCs were washed twice with methanol and precipitate with acetone, in order to remove unreacted species, then they were re-dispersed in ODE. The new colloidal solution was divided in a certain number of identical samples; different heat treatments were applied to each sample.

1.6.3 Heat treatments

A bath of thermal transfer fluid was heated to the desired heat treatment temperature. The NC sample, sealed in a test tube in inert atmosphere, was immersed into the bath for the selected heat treatment time.

1.7 Ligands exchange

In this work, original ligands on the surface of synthesized NCs (typically long-chain carboxylic acids and alkylphosphines) were exchanged with short thiols and inorganic ligands (recently introduced by Talapin group^{56,64,65}), with the aim to explore different NC/surface ligands combinations, finding the more suitable ones for applications presented in Chapters 2 and 3.

1.7.1 Materials

3-mercaptopropionic acid (MPA, >99%) , mercaptoacetic acid (MAA, > 98%), sodium sulfide nonahydrate (Na_2S , 99.9%), ammonium sulfide (40-48% solution in water), ammonium hydroxide (28-30% NH_3 solution in water), sodium hydroxide (NaOH, 97%), methanol (>99.8%), ethanol (>99.5%), acetone (>99.8%), n-hexane (>95%) were obtained from Sigma-Aldrich; SnS_4^{4-} and $\text{Sn}_2\text{S}_6^{4-}$ were obtained according the methods described by Kovalenko et al⁵⁶.

1.7.2 Exchange with thiols

0.1 mmol of NCs were washed twice with methanol, precipitated with acetone and re-dissolved in 4 ml of n-hexane; 0.2 mmol of new ligand (MPA or MAA) were added; the NCs started aggregation/flocculation almost immediately; the suspension was vigorously stirred for 30-60 minutes. Then the suspension was divided in two test tubes; 2 ml of n-hexane and 2 ml of acetone were added to each tube, vigorously mixed, then centrifuged for 5 minutes. The precipitate (formed at the bottom of the test tubes) was then washed and centrifuged/precipitated twice with n-hexane; then it was dispersed in 2 ml ethanol or methanol. To dissolve NCs in water, NCs dispersion in ethanol or methanol was centrifuged; the precipitate was dissolved in a 5 ml NaOH solution in water (pH > 12) or in a 5 ml NH_4OH solution in water (pH > 12).

1.7.3 Exchange with metal-chalcogenide complexes and chalcogenide ligands

0.1 mmol of NCs were washed twice with methanol, precipitated with acetone and re-dissolved in 4 ml of n-hexane; 0.1 mmol of new ligand (SnS_4^{4-} , $\text{Sn}_2\text{S}_6^{4-}$ or Na_2S) were mixed with NaOH or NH_4OH solution in water (5 ml, pH > 12) and added to the NCs solution in n-hexane. NCs in hexane formed a colored phase above the aqueous solution; the two phases were vigorously stirred until the aqueous phase becomes colored and the upper n-hexane phase becomes transparent (typical time: 30-120 minutes). All the liquid was divided in two test tubes, about 4 ml of n-hexane were added to each tube, vigorously mixed, then centrifuged for 5 minutes. The colored precipitate (formed at the bottom of the test tubes) was washed twice with n-hexane, then was dissolved in a 5 ml NaOH solution in water (pH > 12) or in a 5 ml NH_4OH solution in water (pH > 12).

1.8 Characterization

1.8.1 Optical characterization

Absorption and photoluminescence spectra were acquired at regular intervals during synthesis of single-phase NCs; after every half grown ML during shell growth of core-shell NCs and at regular time intervals during diffusion experiments. Small aliquots (generally 0.1 or 0.15 ml) were extracted from reaction solution, diluted in 2 ml n-hexane and placed in a cuvette (Plastibrand® standard disposable PMMA cuvette, pathlength 10 mm). A Perkin-Elmer Lambda Bio 20 spectrophotometer was used to record UV-VIS absorption spectra, in wavelength range between 300 and 800 nm, with a resolution of 0.5 nm. A cuvette filled with clean solvent was used as “blank” reference sample. Photoluminescence spectra were acquired through an OceanOptics SD2000 spectrophotometer, in wavelength range between 250 and 850 nm, with a resolution of 0.36 nm, using a LED as excitation source (emission wavelengths: 300 and 320 nm).

First exciton wavelength λ (corresponding to the lowest energy absorption peak) was determined taking the minimum of the second derivative of the absorption spectrum (applying the Savitzky-Golay method in ThermoGalactic Grams/AI 7.02).

Emission wavelength was determined from peak position of photoluminescence spectrum, fitted with gaussian or log-normal curves, using ThermoGalactic Grams/AI 7.02.

1.8.2 Size evaluation: size curves

For cadmium-based chalcogenides NCs (CdS, CdSe and CdTe), relations linking first exciton peak wavelength λ , molar extinction coefficient ε and diameter D are known and extensively used in literature. It was therefore possible to estimate their size and concentration into a colloidal suspension, once known λ (determined from absorption spectra), using the following relations:

$$\text{for CdS}^{66} \quad D = (-6.6521 \times 10^{-8})\lambda^3 + (1.9557 \times 10^{-4})\lambda^2 - (9.2352 \times 10^{-2})\lambda + 13.29$$

$$\varepsilon = 21536 \times D^{2.3}$$

$$\text{for CdSe}^{67} \quad D = (1.6297 \times 10^{-9})\lambda^4 - (2.8574 \times 10^{-6})\lambda^3 + (1.8873 \times 10^{-3})\lambda^2 - (0.5474)\lambda + 59.61$$

$$\varepsilon = 155507 + (1.6297 \times 10^{-13}) \times e^{E_{1s}/0.1055}$$

$$\text{for CdTe}^{66} \quad D = (9.8127 \times 10^{-7})\lambda^3 - (1.7147 \times 10^{-3})\lambda^2 + (0.4277)\lambda - 194.84$$

$$\varepsilon = 10043 \times D^{2.12}$$

where λ and E_{1s} are the respectively wavelength and the energy of first exciton peak. Concentration C was subsequently estimated using Lambert-Beer's law: $C = A/(\varepsilon \cdot \lambda)$, where A is the optical density at the first exciton peak energy.

1.8.3 Size evaluation: Transmission Electron Microscopy

In case of other compounds (such as zinc chalcogenides) for which sizing curves are not available in literature, it was only possible to estimate their size through effective mass approximation methods (as explained in paragraph 1.8.5), or to measure it through Transmission Electron Microscopy (TEM). It was not possible to estimate their concentration.

TEM samples preparation: diluted solution of NCs in n-hexane were obtained washing original solutions twice in methanol, precipitating with acetone, then re-dissolving in n-hexane. Samples were prepared by drop-casting these diluted solutions on TEM grids (Electron Microscopy Science CF-200 carbon/copper); images were acquired using a Philips EM208 Transmission Electron Microscope. NCs size were directly measured on TEM images, using an ImageJ software.

1.8.4 Core-shell nanocrystals size evaluation: Concentric Shell Model

In this work core-shell NCs size was estimated after knowing (a) the original core dimension; (b) the thickness and composition of every shell monolayer; (c) the number of overgrown monolayers. Assuming a complete reaction of shell precursors and an exclusively heterogeneous nucleation of concentric shells on the core nuclei, the total radius of the core-shell nanoparticles was estimated multiplying the n number of grown monolayers for the monolayer thickness ML , and adding this number to the initial core radius r_c (using a procedure similar to the Concentric Shell Model - CSM - described by van Embden et al.^{9,39}). The amount of precursors needed for overgrowing a shell of known thickness τ on a core of a given radius r_c was calculated from the required increase in volume ΔV :

$$\Delta V = \frac{4}{3}\pi (r_c + \tau)^3 - \frac{4}{3}\pi r_c^3 \quad (1.7)$$

The necessary moles of precursors were calculated from this volume using the density ρ (crystal density of bulk compounds). In SILAR shell growth methods, it is possible to find the amount of precursors needed for the growth of every atomic monolayer (ML) by setting $\tau = ML$. One ML is defined³⁹ as the thickness equal to half of the a lattice constant (for zinc-blende crystal structure) or half of the c lattice constant (for wurtzite crystal structures) of the bulk semiconductors. Values of crystal densities, lattice parameters and ML thickness of compounds evaluated in this study are shown in table 1.6. Correction factors can be introduced to take into account different precursor reactivity. In this work, zinc precursor was injected in 1.5 : 1 molar ratio respect to selenium precursor (when growing ZnSe shells).

1.8.5 Core-shell and alloyed nanocrystals bandgap simulation

As previously discussed, apparent bandgap energy of core-shell NCs depends both on core size, shell thickness, E_G of the two bulk materials and relative CB and VB band offsets; in alloyed NCs, bandgap energy depends also on composition. To predict expected optical properties of these complex NCs (and have a guideline on some experimental data interpretation), first exciton transition energy was calculated according to a modified effective mass approximation method described by Schloss et al.⁶⁸; electron and hole effective masses m_e^* and m_h^* , bulk material bandgap E_G , VB and CB positions (E_{VB} and E_{CB} – expressed as energy respect to vacuum) and electric permittivity ϵ used in these calculations are reported in table 1.7.

compound	crystal structure	a (Å)	c (Å)	ML thickness (nm)	ρ (g/cm ³)
CdS	wurtzite	4.14	6.72	0.34	4.821
	zinc-blende	5.83		0.29	4.855
CdSe	wurtzite	4.30	7.01	0.35	5.662
	zinc-blende	6.08		0.30	5.664
CdTe	zinc-blende	6.48		0.32	5.856
ZnS	wurtzite	3.82	6.26	0.31	4.086
	zinc-blende	5.41		0.27	4.087
ZnSe	zinc-blende	5.67		0.28	5.262

Table 1.6: crystal structure, crystal density, lattice parameters and ML thickness of compounds used in this work^{59,60}

compound	E_G (eV)	E_{CB} (eV)	E_{VB} (eV)	m_e^*	m_h^*	ϵ
CdS ^{60,62,68,69}	2.48	-4.77	-7.25	0.21	0.8	6.23
CdSe ^{60,62,69}	1.75	-4.95	-6.7	0.13	0.43	5.23
CdTe ^{60,62}	1.51	-4.5	-6.01	0.12	0.42	7.1
ZnSe ^{60,62,70}	2.72	-4.06	-6.78	0.18	0.53	5.9

Table 1.7: values of E_G , E_{CB} , E_{VB} , m_e^* , m_h^* and ϵ used in this work

1.8.6 IR spectra of surface ligands

Original ligands: NC samples were taken directly from synthesis solution, washed twice with methanol, precipitated with acetone and re-dissolved in n-hexane, then drop-casted on a IR-transparent window (NaCl or ZnSe crystal).

After ligands exchange: ligands-exchanged samples (prepared as described in paragraphs 1.7.2 - 1.7.3) were drop-casted on a ZnSe crystal from methanol or ethanol dispersions.

In both cases, after solvent evaporation, the IR-transparent window was placed into a sample holder inside the experimental chamber of a Thermo Nicolet Nexus 470 FT-IR spectrometer (operated through a Nicolet Instruments Omnic 5.2 software); IR spectra were acquired between 4000 and 500 cm⁻¹ at a resolution of 0.48 cm⁻¹.

Results and Discussion

1.9 Results

1.9.1 Shared green chemistry synthesis approach

It was possible to synthesize different typologies of nanocrystals (from single-phase to alloyed and/or complex heterostructures) using a simple, common system. One solvent (1-octadecene) and two stabilizing ligands (oleate for cations, trioctylphosphine for anions) were shared for almost all performed synthesis. The only exception were CdTe NCs, that were synthesized from a mixture of cadmium oleate and cadmium octadecylphosphonate as cadmium source. All these objects were successfully synthesized only with air-stable, safe reagents.

1.9.2 Synthesis and optical properties of single-phase nanocrystals

ZnSe, CdS, CdSe and CdTe NCs were successfully obtained. Size ranges and fluorescence wavelength λ_E are reported in table 1.8. TEM images of CdS, CdSe and CdTe NCs are shown in Fig. 1.7; absorption spectra of different sized CdS, CdSe and CdTe NCs are reported in Fig. 1.8.

compound	λ_E range (nm)	size range
ZnSe	360 – 420 nm	2.6 – 4.0 nm
CdS	380 – 470 nm	2.4 – 5.6 nm
CdSe	460 – 590 nm	1.8 – 3.9 nm
CdTe	570 – 660 nm	3.3 – 4.5 nm

Table 1.8: 1^{st} absorption peak wavelength and size range for synthesized single-phase NCs. Cd-based NCs size was determined according to size curves reported in paragraph 1.8.2; ZnSe NCs size was estimated through effective mass approximation (paragraph 1.8.5)

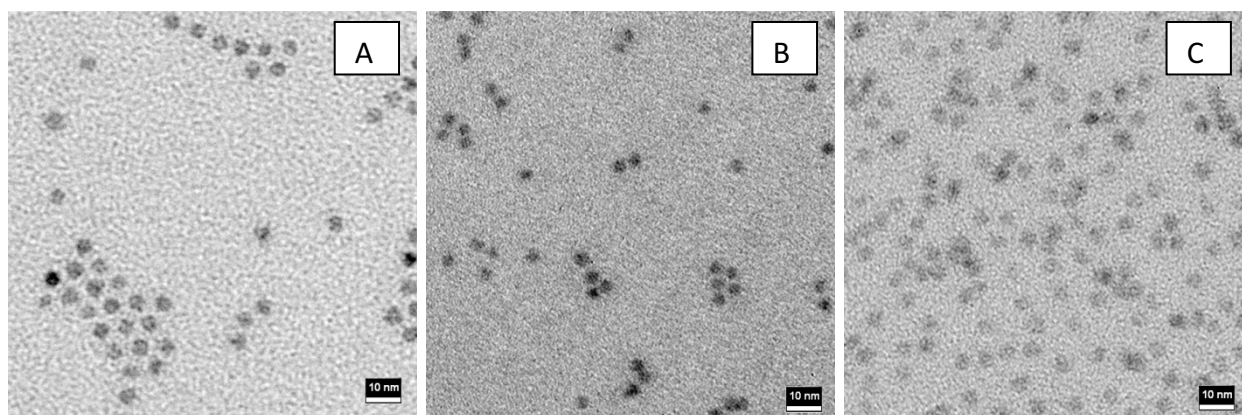


Fig. 1.7: TEM images of single-phase NCs:
 (A) CdS ($d \approx 5$ nm) (B) CdSe ($d \approx 3.3$ nm) (C) CdTe ($d \approx 4$ nm)

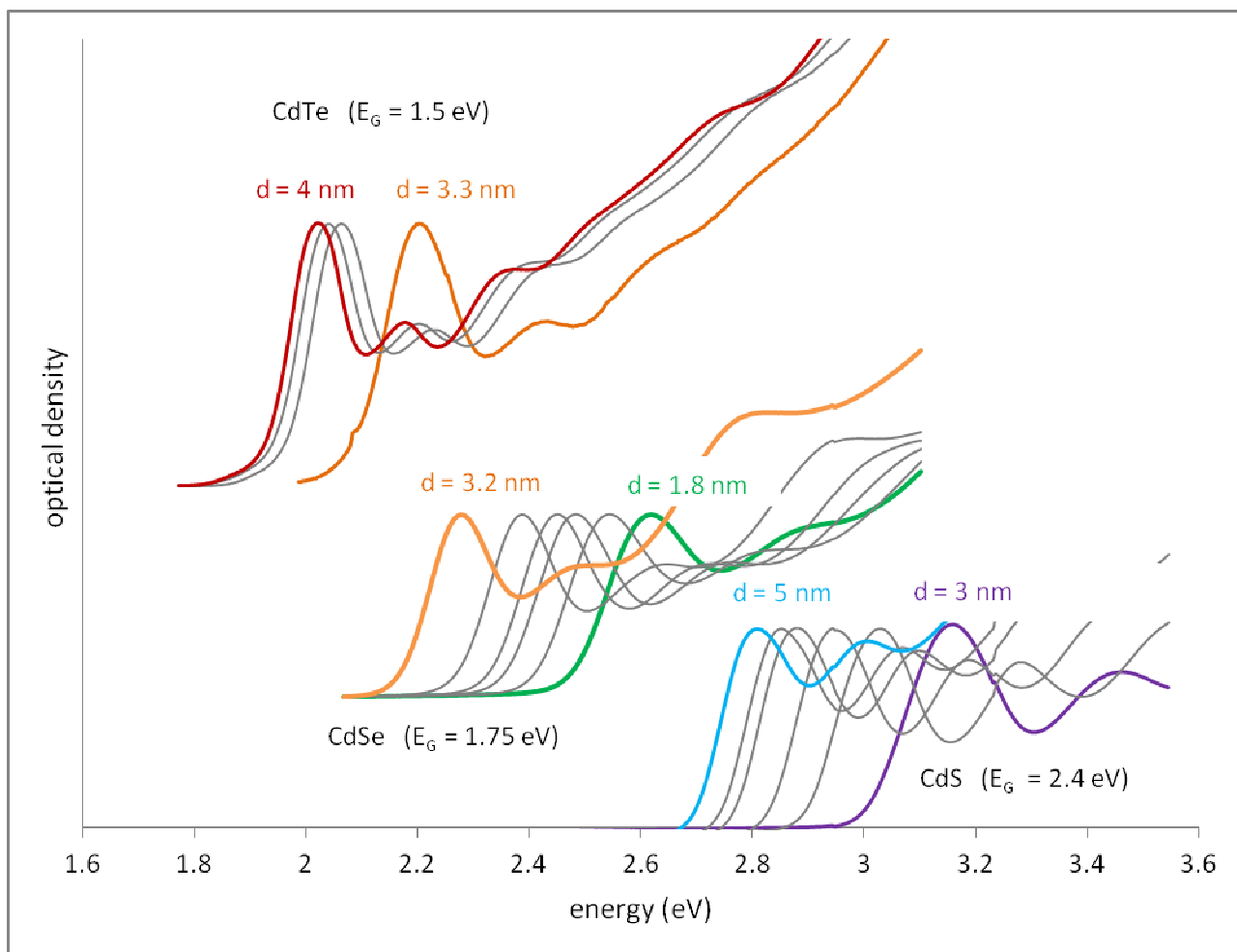


Fig. 1.8: absorption spectra of different sized, single-phase NCs (CdTe, CdSe and CdS)

1.9.3 Synthesis and optical properties of core-shell nanocrystals

Different core-shell or multi-shell NCs were successfully synthesized, mostly via SILAR methods. Compositions, emission wavelengths and sizes are shown in table 1.9.

composition	λ_E range (nm)	expected size (nm)	measured size (nm)
CdSe-ZnSe	570 - 580 nm	6.66 \pm 0.35	5.63 \pm 0.42
CdSe-CdS	570 - 630 nm	6.64 \pm 0.35	6.25 \pm 0.68
CdTe-CdS	620 – 850 nm	7.24 \pm 0.6	7.29 \pm 0.9
CdTe-CdSe	620 – 720 nm	4.75 \pm 0.6	n/m
CdSe-ZnSe-ZnS	570 - 580 nm	6.16 \pm 0.35	n/m
CdSe-CdS-ZnS	570 - 620 nm	6.03 \pm 0.35	n/m

Table 1.9: fluorescence wavelength range (from shell thickness = 0, to the maximum shell thickness value), expected and measured size (at maximum shell thickness) for synthesized core-shell NCs.

Expected size was estimated according to a CSM model (as explained in paragraph 1.8.4)

Measured size was determined from TEM images (as explained in paragraph 1.8.3.)

Some of these core-shell systems (CdSe-ZnSe, CdSe-CdS, CdTe-CdS) were synthesized as promising “building blocks” for the realization of an intermediate-band material (as explained in Chapter 3). CdSe-ZnSe core-shells were synthesized initially as an ideal system, then rejected primarily due to interdiffusion problems. Nevertheless, it was easy to grow thin ZnSe shells (modifying available techniques^{44,71,72}), while the growth of thicker shells was difficult, giving often irregular shaped NCs. Synthesis of CdSe-CdS core-shells are extensively reported in literature^{39-41,73} and their synthesis was easily reproducible and gave spherical-shaped nanoparticles, even if thicker shells were grown. Few synthesis techniques for CdTe-CdS core shells are reported^{74,75}; this system appears to be more difficult to obtain in spherical shape; synthesis often gave flowers, tetragonal or irregular shaped nanocrystals. It was possible to obtain nearly-spherical shaped CdTe-CdS NCs only using a mixture of Cd-OA and Cd-ODPA as cation sources. Other core-shell systems (CdS-ZnS, CdSe-CdS, CdTe-CdSe, CdSe-CdS-ZnS, CdSe-ZnSe-ZnS) were tested as phosphors for LED-based illumination devices (as explained in Chapter 2).

TEM images of CdSe-ZnSe, CdSe-CdS, CdTe-CdS are shown in Figs. 1.9 - 1.10; expected and measured diameters as a function of nominal shell thickness are summarized, for these three systems, in Fig. 1.12

Evolution of absorption and emission spectra during shell growth are reported for CdSe-ZnSe, CdSe-CdS and CdTe-Cds in Figs. 1.12 - 1.14

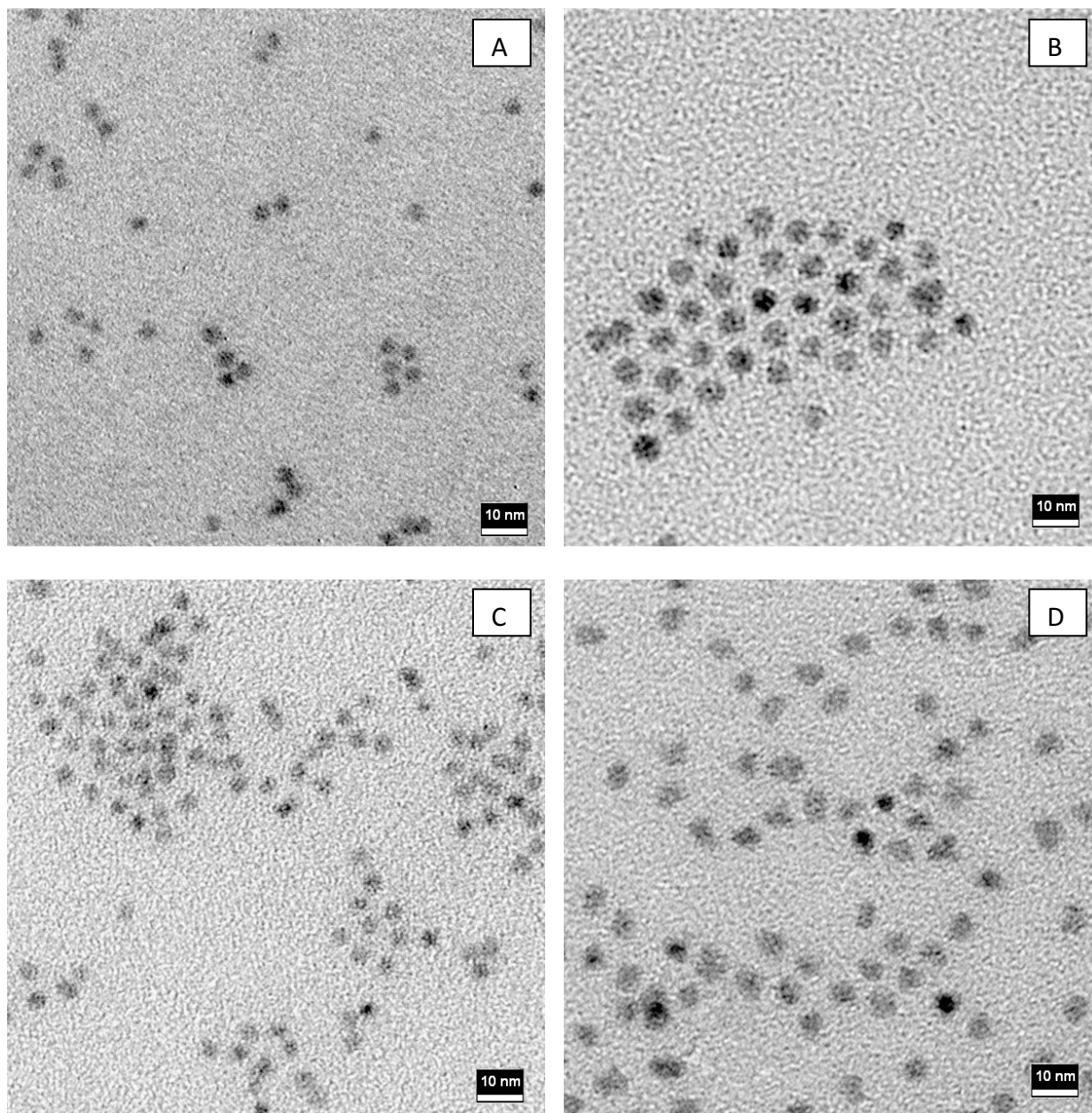


Fig. 1.9: (A) CdSe "core"NCs;
(B) CdSe-CdS core-shell NCs (nominal shell thickness: 5 MLs);
(C) CdSe-ZnSe core-shell NCs (nominal shell thickness: 3 MLs);
(D) CdSe-ZnSe core-shell NCs (nominal shell thickness: 6 MLs)

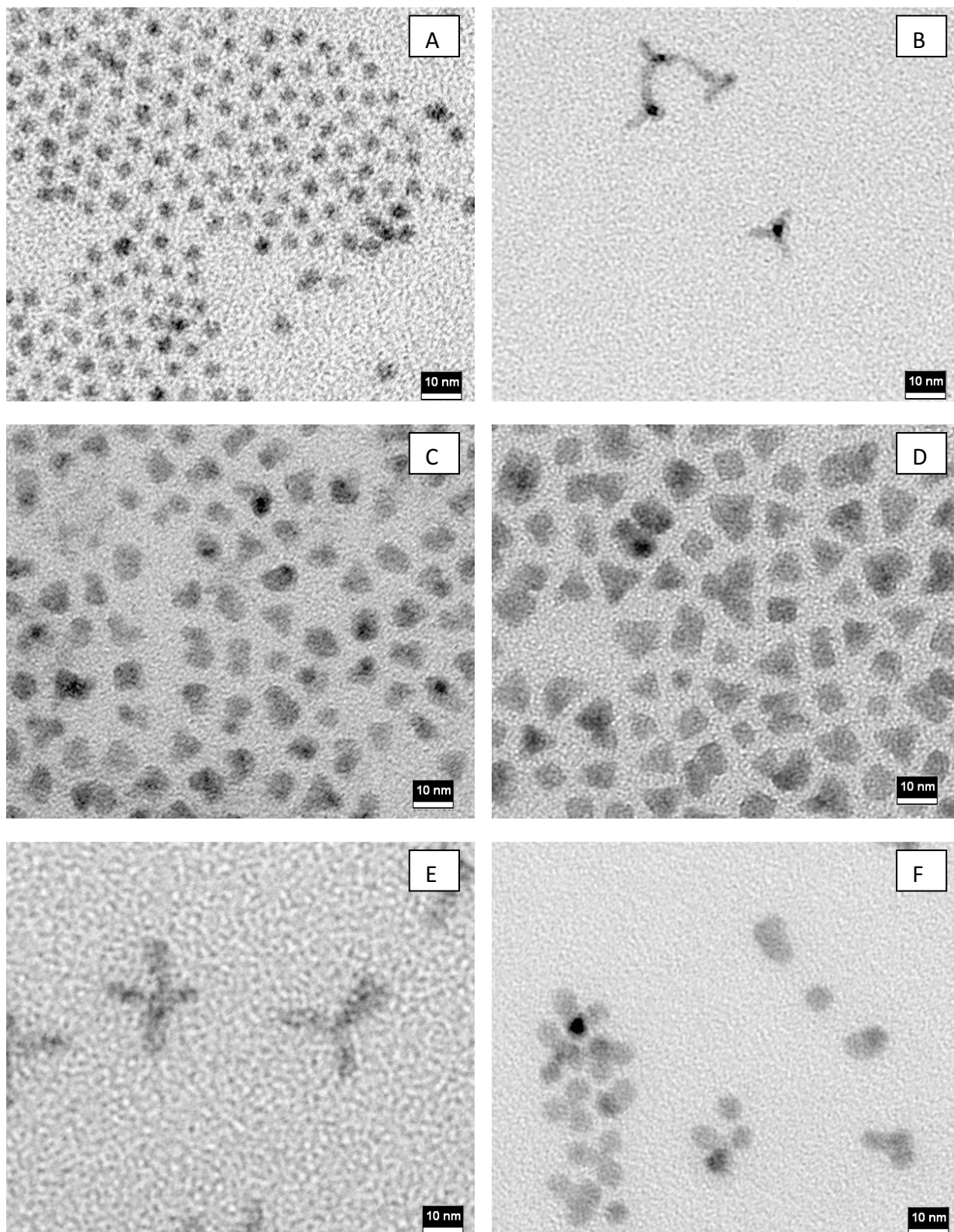


Fig. 1.10: (A) CdTe spherical “core” NCs; (B) CdTe tetrapod-shaped “core” NCs
 (C) CdTe-CdS core-shell “nearly-spherical” NCs (nominal shell thickness: 5 MLs)
 (D) CdTe-CdS core-shell NCs, cubic and tetragonal-shaped
 (E) CdTe-CdS tetrapod-shaped, multi-phase NCs
 (F) CdTe-CdSe “flower-shaped”, multi-phase NCs

CdSe-based systems (Fig. 1.9)

- CdSe NCs shown in Fig 1.9 (A) were used as “cores” for core-shell NCs shown in Fig. 1.9 (B), (C) and (D). Their expected diameter (according Jasieniak et al.⁶⁷ sizing curve) is 3.3 ± 0.4 nm; the average measure diameter from TEM images is 3.4 ± 0.3 nm, giving an average (measured/expected) size ratio of 1.03.
- CdSe-CdS core shell NCs, with a nominal thickness of 5 CdS MLs, shown in Fig. 1.9 (B), have an expected diameter (calculated with a CSM model, as explained in paragraph 1.8.4) of 6.6 ± 0.4 nm; their TEM measured diameter is 6.3 ± 0.7 . Average (measured/expected) size ratio is 0.95
- CdSe-ZnSe core shell NCs shown in Fig. 1.9 (C) (nominal thickness of 3 ZnSe MLs) have an expected diameter (CSM model) of 5.0 ± 0.4 nm; measured diameter is 4.8 ± 0.5 nm, giving an average size ratio of 0.96.
- CdSe-ZnSe core shell NCs shown in Fig. 1.9 (D) (nominal thickness of 6 ZnSe MLs) have an expected diameter (CSM model) of 6.7 ± 0.4 nm; measured diameter is 5.7 ± 0.4 nm, giving an average size ratio of 0.85.

CdTe-based systems (Fig. 1.10)

- Spherical CdTe NCs, shown in Fig 1.10 (A), were used as “cores” for CdTe-CdS core-shell nanocrystals shown in Fig. 1.10 (C) and (D); they were synthesized using a mixture of cadmium oleate and cadmium octadecylphosphonate as cation source ; their expected diameter (according Yu et al.⁶⁶ sizing curve) is 3.9 ± 0.4 nm; the average measure diameter from TEM images is 4.1 ± 0.6 nm, giving an average (measured/expected) size ratio of 1.05.
- CdTe nano-tetrapods shown in Fig 1.10 (B) were used as “cores” for multi-phase NCs shown in Fig. 1.10 (E) and (F); they were synthesized using cadmium oleate only as cation source. Their expected diameter (according Yu et al.⁶⁶ sizing curve) should be around 4.8 ± 0.5 nm; their shape not spherical; their arms length range between 6 and 8 nm.
- CdTe-CdS core shell NCs shown in Fig. 1.10 (C) - the only ones with a nearly spherical shape - have a nominal thickness of 5 CdS MLs. CdS shell was grown using cadmium oleate as cadmium source. Their expected diameter (calculated with a CSM model) is 7.2 ± 0.4 nm; measured diameter on TEM images is 7.4 ± 0.9 nm; giving an average (measured/expected) size ratio of 1.03.
- CdTe-CdS, cubic /tetragonal core shells shown in Fig. 1.10 (D), were synthesized using a mixture of cadmium oleate and cadmium octadecylphosphonate as shell cadmium source. Their expected diameter (nominal shell thickness: 5 MLs, calculated with a CSM model) is 7.2 ± 0.4 nm; size was not measured on TEM images due to irregular shapes.
- CdTe-CdS and CdTe-CdSe irregular-shaped multi-phase NCs, shown in Fig. 1.10 (E) and (F) respectively, were synthesized from CdTe nano-tetrapods cores shown in Fig. 1.10 (B). Their expected diameter was not calculated

Measured sizes are in good agreement with predicted sizes, as one can see in Fig. 1.11. CdSe NCs and CdSe-based core-shell systems were easily obtained in spherical shape using cadmium and zinc oleate as cation sources. The shape of CdTe NCs seems to be strongly related on precursor used: spherical NCs were obtained only using Cd-ODPA as cation source (alone, or mixed with Cd-OA): if Cd-OA was used as the only cation source, CdTe grew in the form of nano-tetrapods. Overgrowing CdS or CdSe shells on CdTe nano-tetrapod gave tetrapod or flower-shaped nano-heterostructures. When spherical CdTe NCs were used as “cores”, it was possible to overgrow a nearly-spherical CdS shell using Cd-OA as the only cation source; if also Cd-ODPA was used, the shell grew in cubic or tetragonal shape. The effect of anion sources (TOPS and/or TOPSe were used in all the performed synthesis) on shape was not investigated. Fig. 1.11 summarizes the expected and measured diameters as a function of nominal shell thickness (expressed in monolayers – MLs) for the three examined systems.

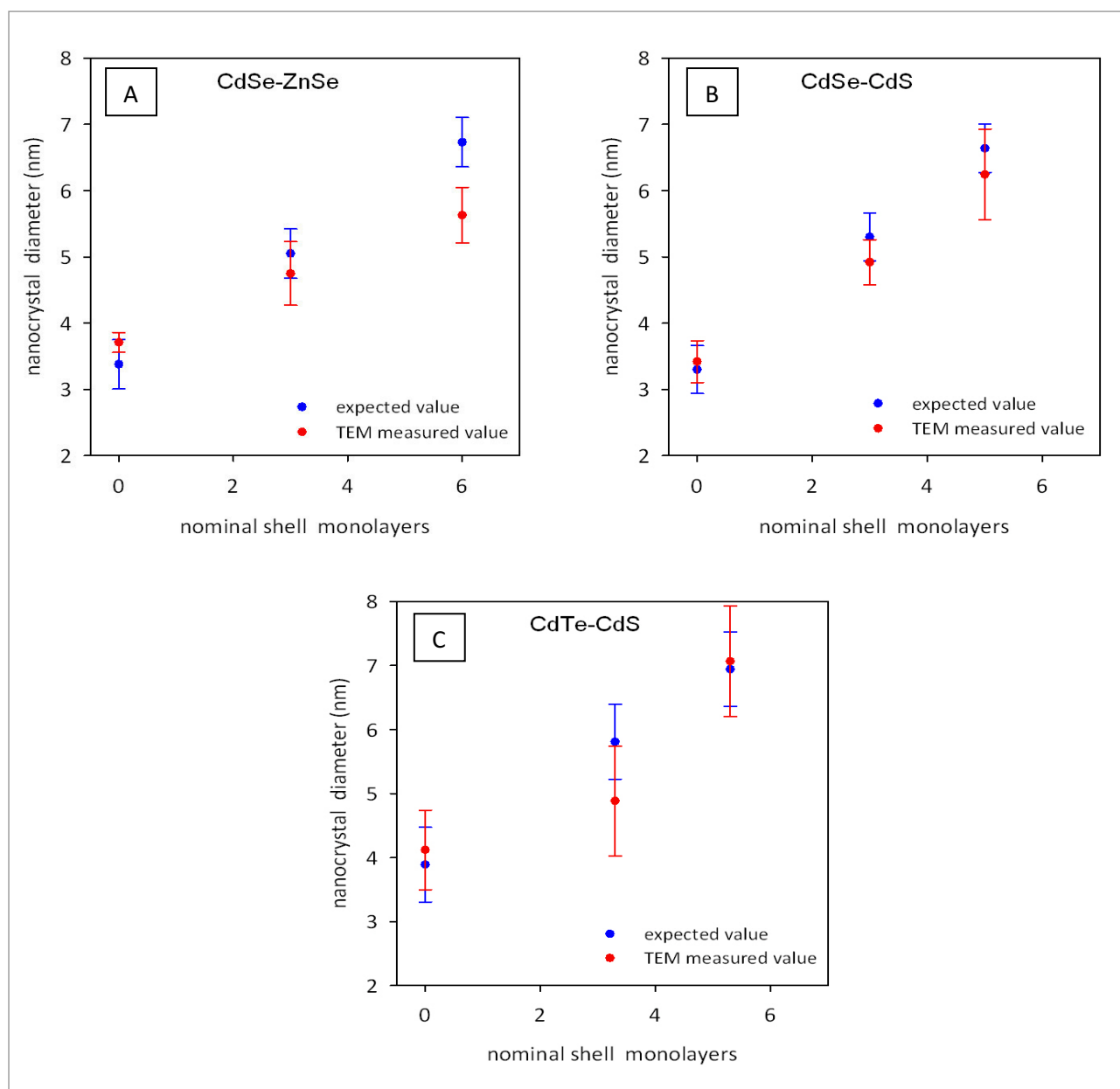


Fig. 1.11: expected and measured diameter as a function of nominal shell thickness (expressed in MLs) for (A) CdSe-ZnSe (B) CdSe-CdS (C) CdTe-CdS

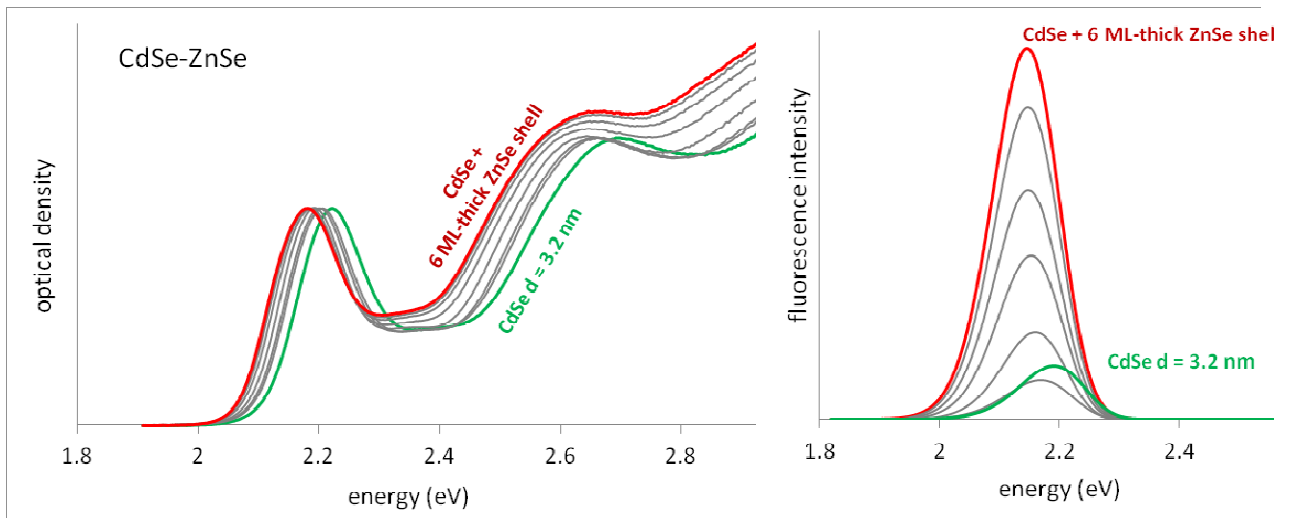


Fig. 1.12: evolution of absorption spectra (left) and photoluminescence spectra (right) after overgrowing ZnSe shell on CdSe NCs with diameter of 3.2 nm. Each curve between CdSe (green) and 6ML-thick shell (red) represents a shell layer with nominal thickness of half-ML (in absorption spectra) or one ML (in photoluminescence spectra)

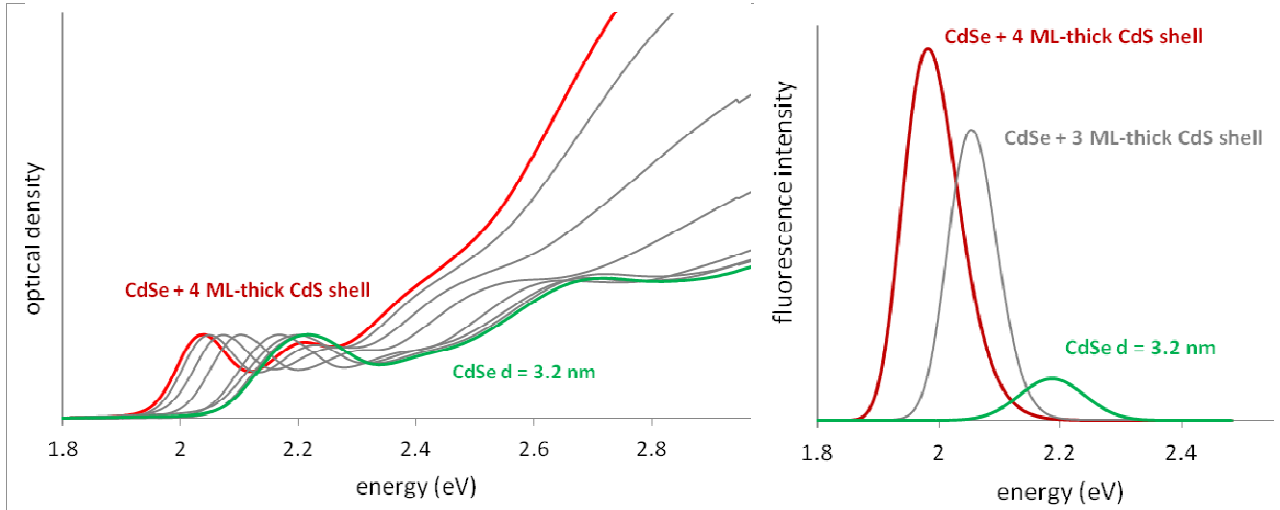


Fig. 1.13: evolution of absorption spectra (left) and photoluminescence spectra (right) after overgrowing CdS shell on CdSe NCs with diameter of 3.2 nm. Each curve in absorption spectra between CdSe (green) and 4ML-thick shell (red) represents a shell layer with nominal thickness of half-ML

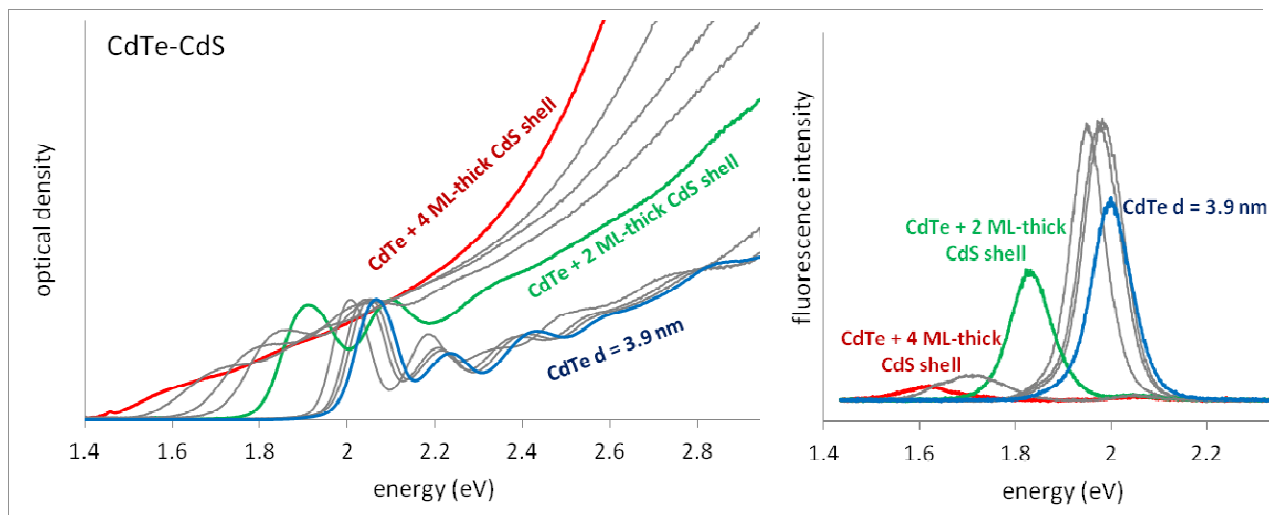


Fig. 1.14: evolution of absorption spectra (left) and photoluminescence spectra (right) after overgrowing CdS shell on CdTe NCs with diameter of 3.9 nm. Each curve between CdTe (blue) and 4ML-thick shell (red) represents a shell layer with nominal thickness of half-ML.

Different behaviours can be noticed between Type-I confinement regime [from CdTe (blue) to 2ML-thick shell (green)] and Type-II confinement regime [from 2ML-thick shell (green) to 4ML-thick shell (red)]

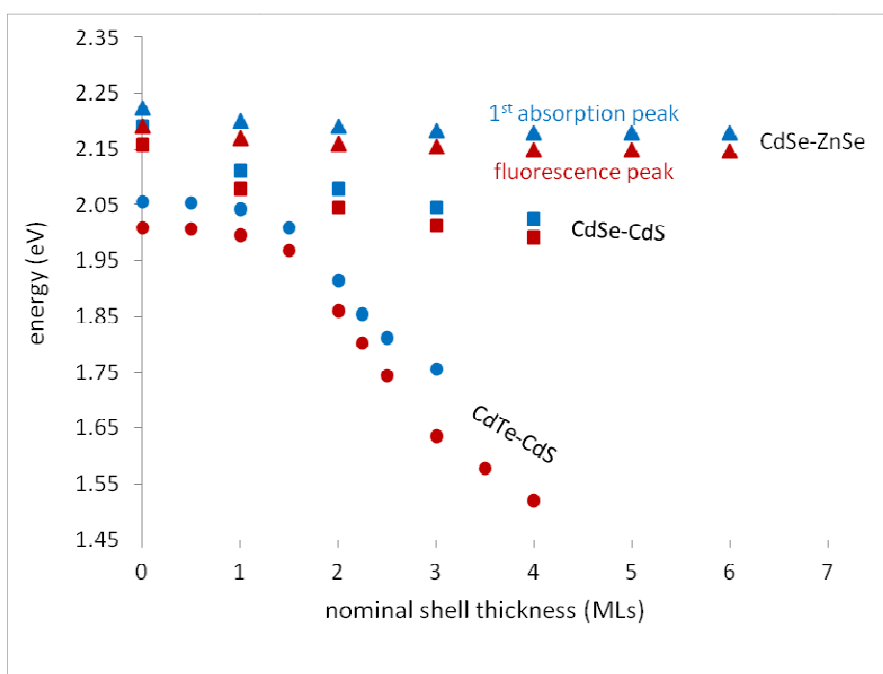


Fig. 1.15: evolution of 1st absorption peak position (blue) and fluorescence peak position (red) during shell growth, for CdSe-ZnSe (triangles), CdSe-CdS (squares) and CdTe-CdS (circles).

- CdSe-ZnSe (Fig. 1.12) and CdSe-CdS (Fig. 1.13) systems:

Growth of ZnSe and CdS shells on CdSe NCs causes a bathochromic shift of first absorption peak and fluorescence peak (corresponding to a decrease of nanocrystal apparent bandgap). The spectra maintain their overall shape, while the optical density at lower wavelength seems to rise proportionally to the shell thickness. Similar shifts have already been reported for CdSe-ZnSe^{38,44} and CdSe-CdS core-shell NCs^{37,40,46}, and motivated with a partial leakage of the exciton into the shell. The decrease seems more evident for a CdS shell, as it can be noticed in Fig. 1.15. This trend can be explained by an effective mass model: both these systems can be labeled as *quasi-Type-I* core-shells (see paragraph 1.2.2-d); as a consequence of the different band offsets (schematically represented in Fig. 1.16) CdSe-CdS does not confine electrons in the core (while CdSe-ZnSe does); on the other side, CdSe-CdS confines holes in the core (while CdSe-ZnSe does not); since the electron effective mass is smaller than the hole effective mass in both systems (see table 1.7, p. 24), the confining potential term of the electron has more importance in the final effective bandgap energy. The CdS shell growth causes a decrease in electron confining potential term, which was higher in the original CdSe NCs with respect to the hole confining potential term, that decreases with the growth of a ZnSe shell. Therefore, at the same thickness, growing a CdS shell should cause a more evident bandgap reduction than a ZnSe one.

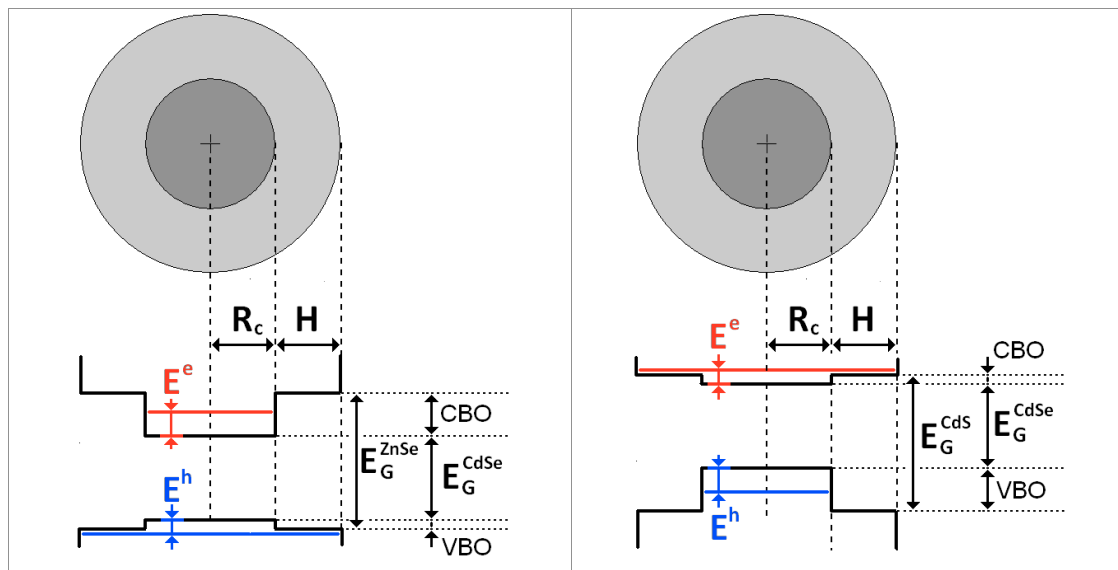


Fig. 1.16: schematic representation of CdSe-ZnSe (left) and CdSe-CdS (right) core-shell heterostructures, with core radius R_c and shell thickness H ; CBO is the CB offset of the bulk compounds; VBO is the VB offset of the bulk compounds; E^e the electron energy (respect to the CB bottom of bulk CdSe); E^h the hole energy (respect to the VB top of bulk CdSe); E_G^{CdSe} the bulk CdSe bandgap energy; E_G^{CdS} the bulk CdS bandgap energy. The NC apparent bandgap is given by $E_G^{CdSe} + E^e + E^h$

- CdTe-CdS system (Fig. 1.14)

Growth of CdS shell on CdTe NCs causes initially (up to the 2nd ML) a behavior similar to that reported for the previous systems; after that point, the apparent bandgap decrease become more pronounced and the spectra do not maintain their overall shapes; shell growth is also accompanied by spectral

broadening and fluorescence intensity reduction, while the distinctive peaks in the absorption spectra are replaced with a featureless absorption tail. According to Kim and co-workers¹⁸, these are typical features of *Type-II* core-shell structure. CdTe-CdS system exhibit a large valence band offset (1.21 eV), while a relatively small difference (0.22 eV) exists between conduction bands. Moreover, the CdTe valence band position resides at an energy higher than the CdS valence band position, respect to vacuum level (as schematized in Fig. 1.17). In the case of bulk CdTe-CdS interfaces, such alignment would nominally correspond to a *Type-II* confinement, in which the hole is confined in the core and the electron in the shell. The situation, however, changes in these nano-heterostructures, in which the alignment of the energy states is determined also by confinement energies: once fixed core size, it is possible to switch between *Type-I* and *Type-II* confinement regime by increasing the shell thickness (as it can be seen in Fig. 1.17):

- if the shell is thin enough, the electron is distributed over the entire NC, while the hole resides primarily in the core (*Type-I* confinement);
- for a shell thick enough, the electron wave function becomes localized primarily in the shell, while the hole remains in the core (*Type-II* confinement).

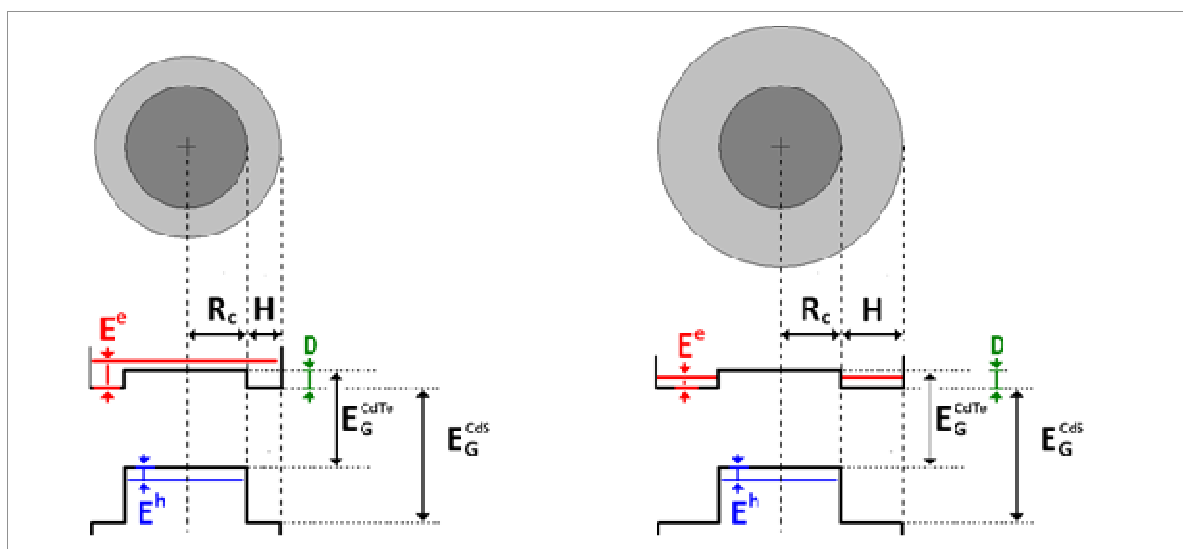


Fig. 1.17: schematic representation of possible configurations of CdTe-CdS core-shell NCs:

Type-I confinement (left) or *Type-II* confinement (right).

R_c is the CdTe core radius; H the CdS shell thickness; D the CB offset between bulk CdTe and bulk CdS; E^e the electron energy (respect to the CB bottom of bulk CdS); E^h the hole energy (respect to the VB top of bulk CdTe); E_G^{CdTe} the bulk CdTe bandgap energy; E_G^{CdS} the bulk CdS bandgap energy

The transition between *Type-I* and *Type-II* confinement takes place for thinner shell at larger core sizes (as it can be noticed in Fig. 1.18). For the largest CdTe cores ($d = 4.5$ nm), the emission peak shows an energy even lower than the bulk CdTe bandgap, as it can be seen in Fig. 1.18. This can be motivated by a recombination taking place by a LUMO level situated at an energy lower than the CdTe conduction band and a HOMO level situated near the top of the CdTe valence band.

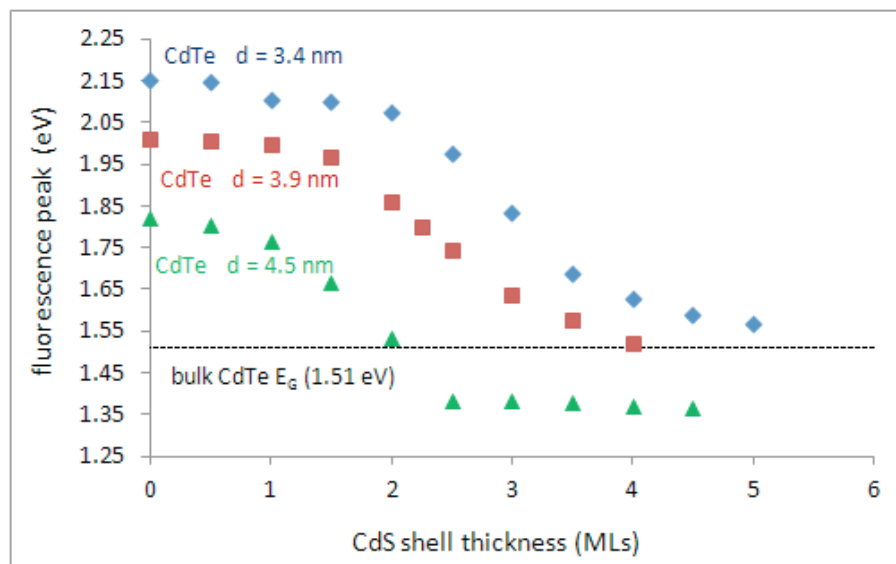


Fig. 1.18: evolution of fluorescence peak position during CdS shell growth on CdTe NCs with different diameters: 3.4 nm (blue), 3.9 nm (red) and 4.5 nm (green). Bulk CdTe bandgap (1.51 eV) is displayed as a horizontal dotted line.

1.9.4 Synthesis of alloyed nanocrystals

Alloyed or partially alloyed NCs were successfully synthesized, through simple, hot injection techniques or via heat treatments in solution of pre-synthesized core-shell systems. Precursors molar ratio used in synthesis, emission wavelength (λ_E), shape and size of synthesized objects are shown in table 1.10. Shape and size were assessed via TEM imaging (shown in Fig 1.19) only for some of these formulations. These partially alloyed NCs, thanks to their high fluorescence efficiency and their simple synthetic techniques, were successfully tested as phosphors for illumination devices (as explained in Chapter 2).

composition	precursors ratio	λ_E range (nm)	shape	size range (nm)
$\text{Cd}_{1-x}\text{Zn}_x\text{S-ZnS}$	Zn/Cd = 20	410 - 415	n/m	n/m
	Zn/Cd = 3.35	415 - 420		
	Zn/Cd = 1	420 - 440		
	Zn/Cd = 0.33	430 - 475		
$\text{Cd}_{1-x}\text{Zn}_x\text{Se-ZnSe}$	Zn/Cd = 40	527	mostly spherical	6-10 nm
	Zn/Cd = 20	521	spherical	6-10 nm
$\text{CdSe}_{1-x}\text{S}_x\text{-CdS}$	S/Se = 9	538	mostly spherical	3-4 nm
	S/Se = 20	515	spherical	4-5 nm

Table 1.10: composition, precursor molar ratio, fluorescence wavelength range, shape and measured size range for synthesized alloyed NCs.

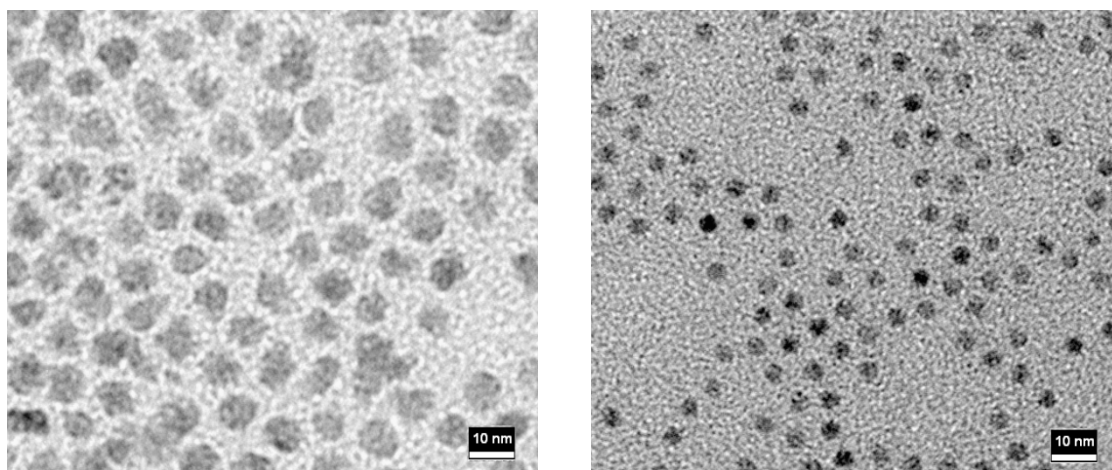


Fig. 1.19: TEM images of alloyed NCs: (left) $\text{Cd}_{1-x}\text{Zn}_x\text{Se-ZnSe}$ NCs; (right) $\text{CdSe}_{1-x}\text{S}_x\text{-CdS}$ NCs

1.9.5 Heat treatment effect on nanocrystals bandgap

Heat treatments on CdSe-ZnSe and CdSe-CdS core-shell nanoparticles caused hypsochromic shifts of the first absorption peak, corresponding to an increase of the nanocrystal apparent bandgap (as it can be seen in Fig. 1.20); this can be motivated by the alloying of the two materials: CdSe/ZnSe or CdSe/CdS alloys should have bandgap energies between that of CdSe and those of ZnSe and CdS, respectively (and this energy should be related to the chemical composition of the alloy, according to Vegard's law). Since ZnSe and CdS have bandgap energies higher than that of CdSe, alloying causes a hypsochromic shift of the first absorption peak respect to its original position.

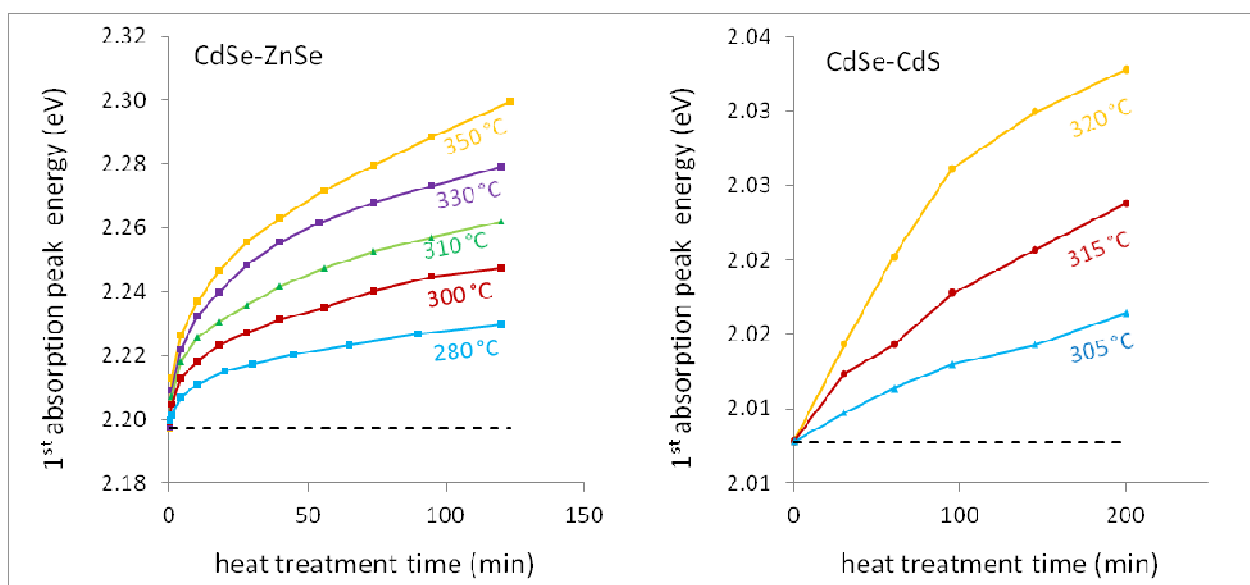


Fig. 1.20: 1st absorption peak position as a function of heat treatment time for:
 - CdSe-ZnSe core-shell NCs (Left - temperatures between 280 °C and 350 °C)
 - CdSe-CdS core-shell NCs (Right - temperatures between 305 °C and 320 °C)

The observed bandgap increase is way more remarkable in CdS-ZnSe system, at same heat treatment conditions, respect to CdSe-CdS system (as it can be noticed in Fig. 1.21). This can be explained by the E_G difference between CdSe and ZnSe, that is larger than the one between CdSe and CdS. Furthermore, some authors^{9,17} suggest that in common anion systems (such as CdSe-ZnSe) the diffusion of the smaller cations should be more efficient between tetrahedral interstitial states; it can be therefore speculated that the alloying process in CdSe-ZnSe NCs is easier than in CdSe-CdS NCs.

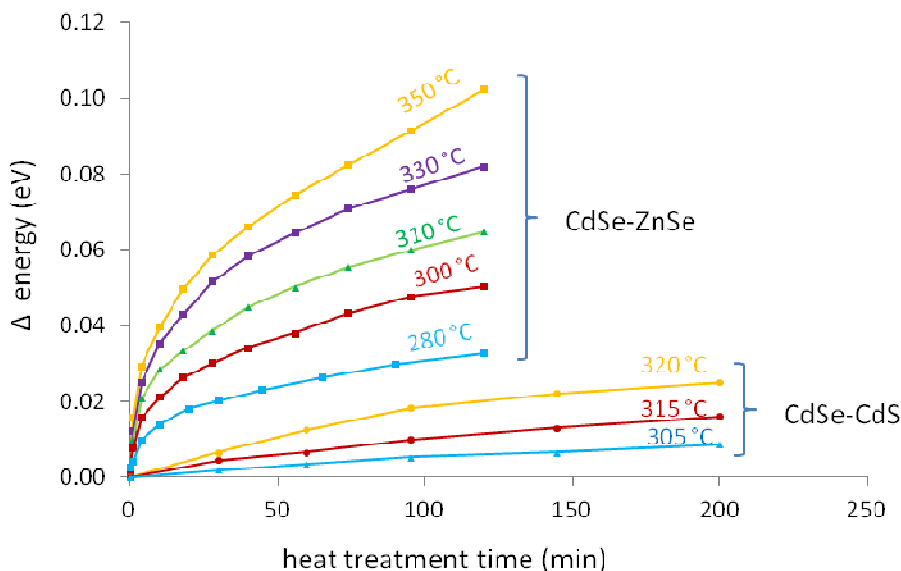


Fig. 1.21: hypsochromic shift of bandgap energy as a function of heat treatment time for:
 - CdSe-ZnSe (temperatures between 280 °C and 350 °C)
 - CdSe-CdS core-shell NCs (temperatures between 305 °C and 320 °C)

1.9.6 Bandgap simulation

Apparent bandgap energies E_G of CdSe-ZnSe and CdSe-CdS core-shell NCs, as well as CdZnSe and CdSeS alloyed NCs, were simulated via effective mass approximations.

Fig. 1.22 shows E_G of CdSe-ZnSe and CdSe-CdS core-shell NCs as a function of initial core diameter, for different shell thicknesses (from bare core NC, with thickness = 0, to a shell thickness of 5 nm). It is possible to notice how the shell thickness influence on bandgap is more remarkable at smaller core diameters, and that CdS shells, at the same core diameter, cause larger bathochromic shifts than ZnSe shells. This agrees with experimental data (see paragraph 1.9.3), that are limited to a narrow region of core diameters d ($3 < d < 3.5$) and shell thicknesses h ($0 < h < 1.6$). Simulations allowed to cover a wider region of core diameters and shell thicknesses, not accessible through simple colloidal synthesis.

Fig. 1.23 shows E_G of CdZnSe and CdSeS alloyed NCs as a function of NC diameter, for different compositions (from pure CdSe to pure ZnSe or CdS). Larger particles seem to be more affected by diffusion; CdZnSe system (large E_G difference between CdSe and ZnSe) is more affected than CdSeS. In these cases, simulations allowed to establish relations between bandgap, composition and size.

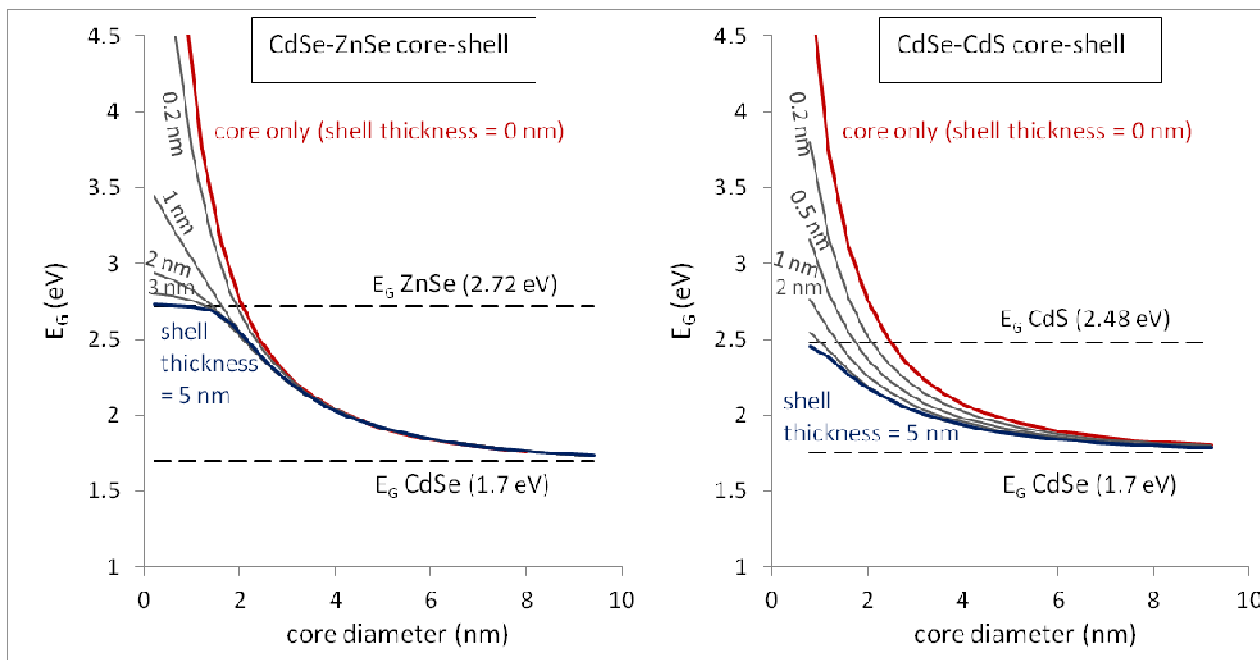


Fig. 1.22: bandgap energy simulation for CdSe-ZnSe (left) and CdSe-CdS (right) core-shell NCs as a function of core diameter, for different shell thicknesses (red = no shell; blue = max simulated shell thickness)

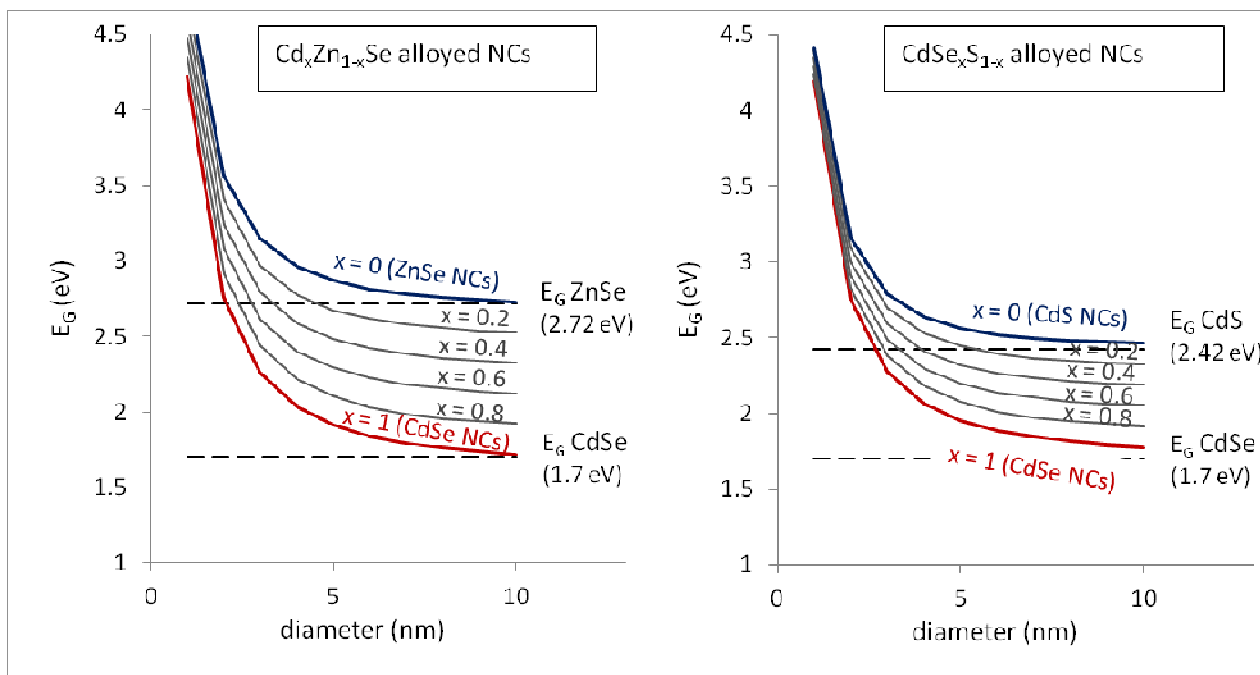


Fig. 1.23: bandgap energy simulation for Cd_xZn_{1-x}Se (left) and CdSe_xS_{1-x} (right) alloyed NCs as a function of NCs diameter, for different alloy compositions (red line: x = 0, pure CdSe; blue line: x = 1, pure ZnSe or CdS)

1.9.7 IR spectra of surface ligands

IR absorption spectra of Cd-based NCs with original ligands, compared with IR absorption spectrum of cadmium oleate are shown in Fig. 1.24 ; IR absorption spectrum of ZnSe NCs with original ligands, compared with IR absorption spectrum of zinc oleate are shown in Fig. 1.25.

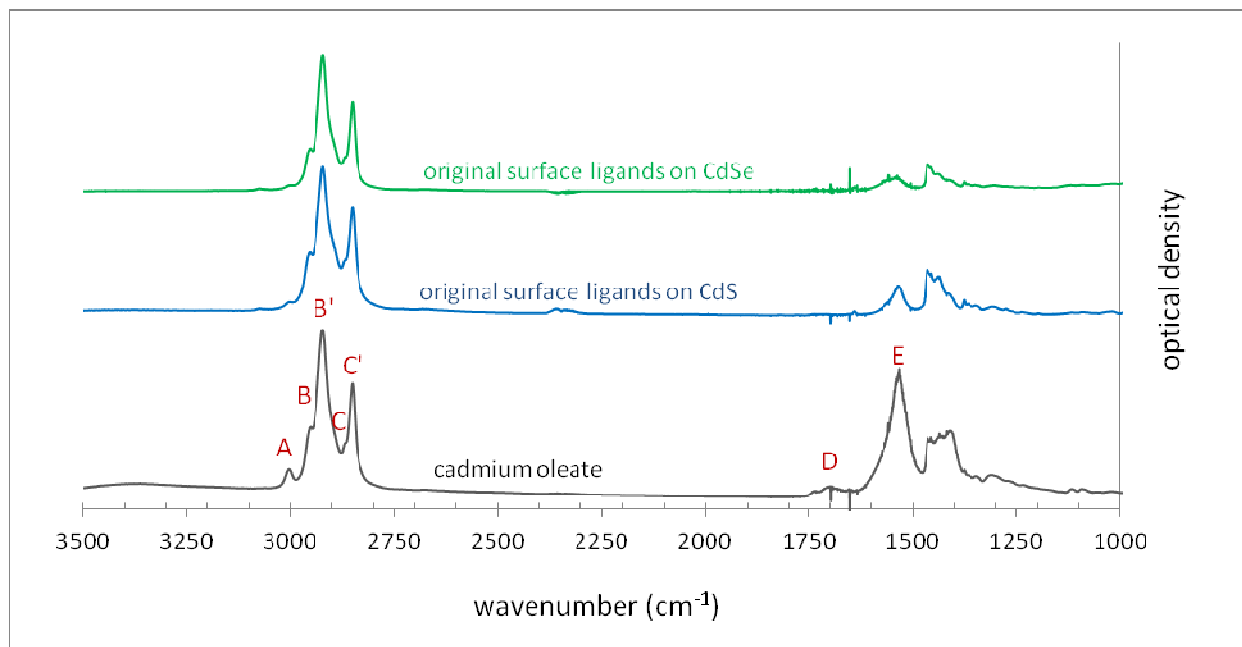


Fig. 1.24: IR absorption spectra of original surface ligands on CdSe NCs (green) and CdS NCs (blue) compared with IR absorption spectrum of cadmium oleate (black)

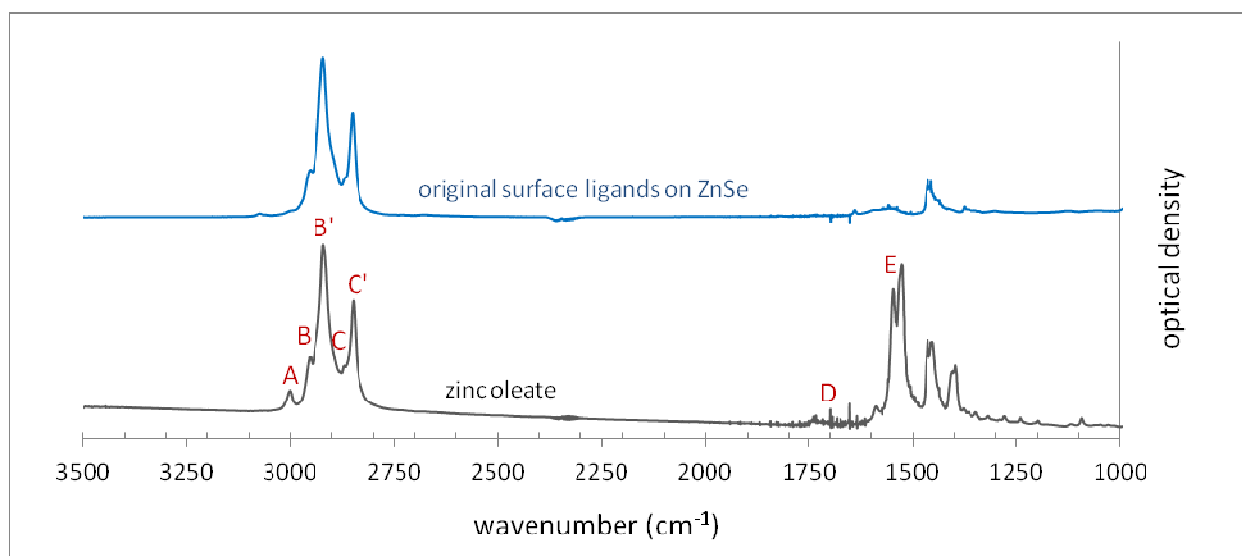


Fig. 1.25: IR absorption spectrum of original surface ligands on ZnSe NCs (blue) compared with IR absorption spectrum of zinc oleate (black)

IR absorption spectra of original surface ligands on NCs samples appear very similar to those of cadmium oleate (see Fig. 1.24) and zinc oleate (see Fig. 1.25); they show typical vibration frequencies of metal-oleate complexes⁷⁶⁻⁷⁸:

- (A) 3005 cm^{-1} – stretch of C-H group close to C=C group;
 (B) 2955 cm^{-1} - asymmetric CH_3 stretch (C) 2923 cm^{-1} - asymmetric CH_2 stretch
 (B') 2870 cm^{-1} - symmetric CH_3 stretch (C') 2853 cm^{-1} - symmetric CH_2 stretch
 (D) 1705 cm^{-1} - C=O stretch (E) 1535 cm^{-1} - asymmetric COO^- stretch

It is possible to identify original surface ligands as oleate ions (de-protonated oleic acid, see Fig. 1.26), most likely bound on surface metal atoms in a bidentate mode (note the asymmetric COO^- stretch at 1535 cm^{-1}); in fact, other signatures such as the broad, “hilly” region between 3500 and 2300 cm^{-1} (related to O-H stretch) or the strong C=O stretch at 1705 cm^{-1} , are not noticeable in the IR absorption spectrum of NCs; this also confirms the absence of “free” (not de-protonated) oleic acid (confront cadmium oleate and oleic acid IR spectra in Fig 1.27), meaning that the preliminary washing procedure removed any possible excess/unreacted ligand that could have remained in solution after synthesis.

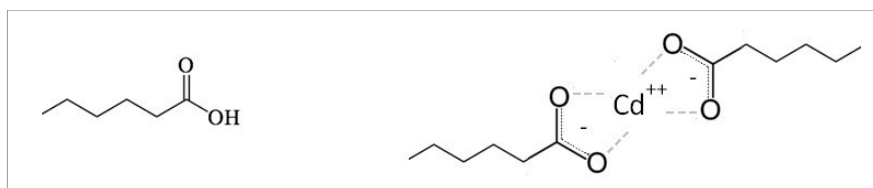


Fig. 1.26: free carboxylic acid (left) and metal-carboxylate complex (right)

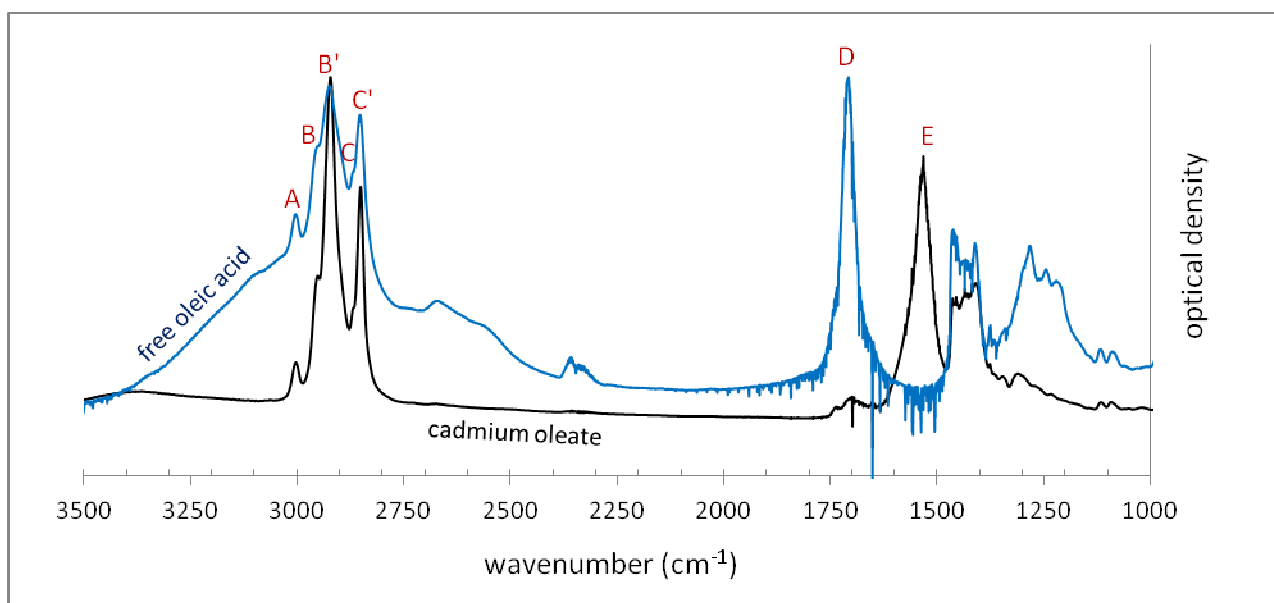


Fig. 1.27: IR absorption spectra of oleic acid(blue) and cadmium oleate (black)

Confronting IR spectra of CdS NCs before and after the original ligands/MAA exchange procedure (Fig. 1.28), it is possible to notice: (i) the disappearance of asymmetric and symmetric CH_3 stretches; (ii) a reduction in intensity of asymmetric and symmetric CH_2 stretches; (iii) the appearance of a strong $\text{C}=\text{O}$ stretch signal; these vibrational frequencies are consistent with MAA functional groups: IR spectra of MAA-covered NCs and MAA are very similar (see Fig. 1.29); the $\text{C}=\text{O}$ stretch signal suggests that the MAA is bound via the sulfur atom, not through the cadmium-mercaptoacetate complex (see Fig. 1.30). Similar results were obtained from MPA on CdS NCs, and MAA and MPA on CdSe, CdTe, CdSe-ZnSe, CdSe-CdS and CdTe-CdS NCs.

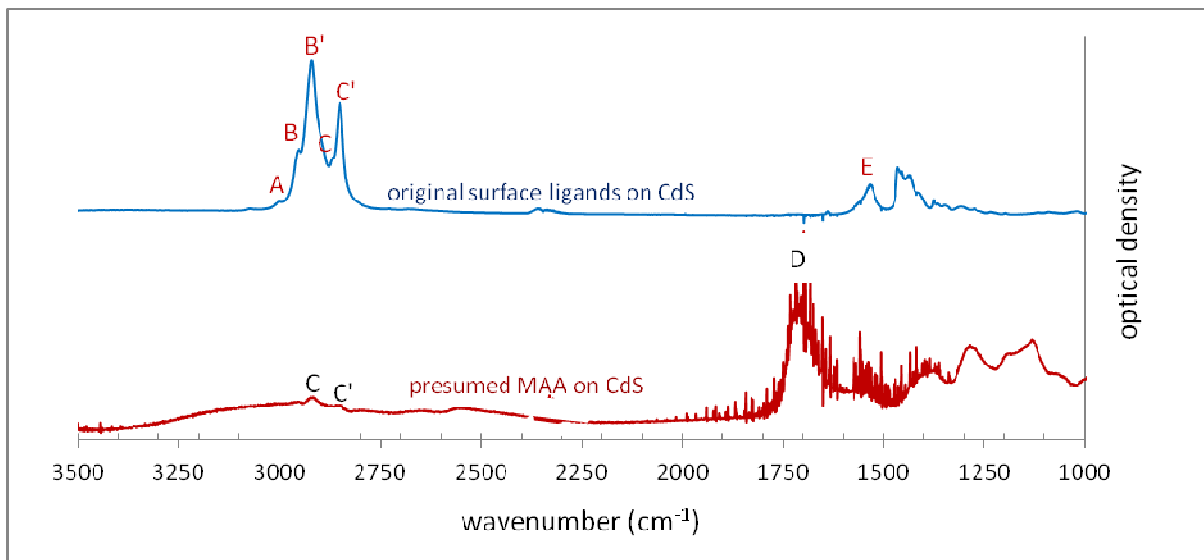


Fig. 1.28: IR absorption spectra of original surface ligands on CdS NCs (blue) and new surface ligands (presumably mercaptoacetic acid) on CdS NCs after ligand exchange procedure (red)

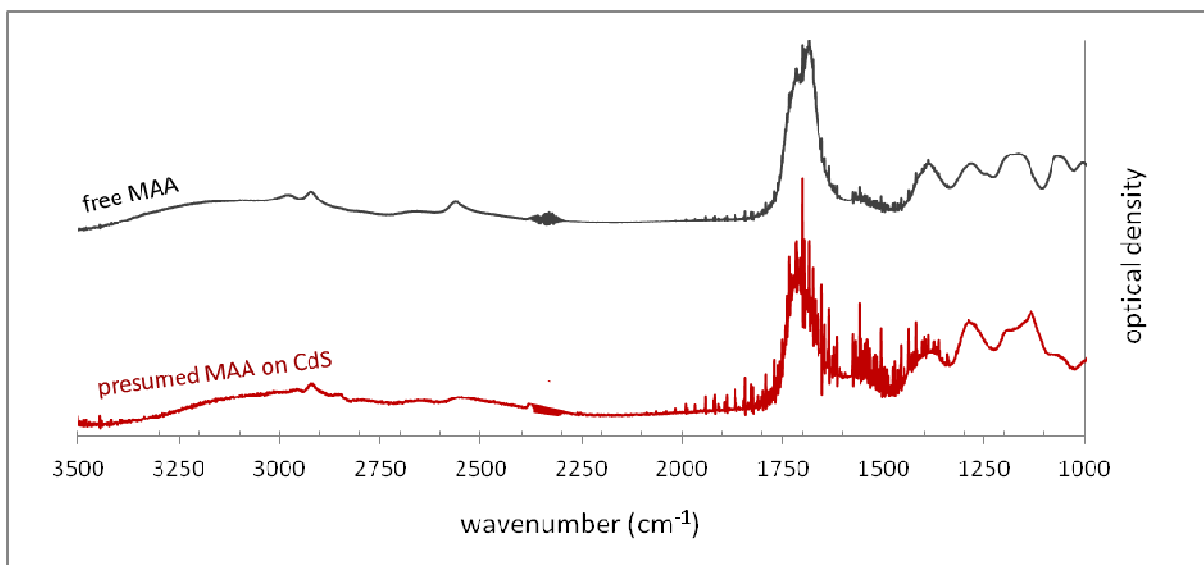


Fig. 1.29 IR absorption spectra of mercaptoacetic acid (black) and new surface ligands (presumably mercaptoacetic acid) on CdS NCs after ligand exchange procedure (red)

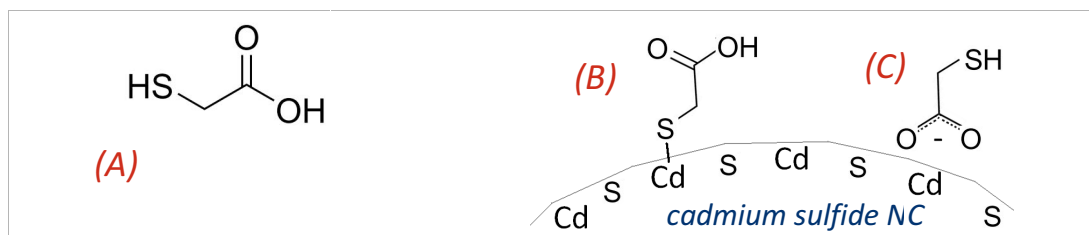


Fig. 1.30: mercaptoacetic acid (A) and two possible configuration for its surface adsorption on CdS NCs: acetic acid thiolate (B) and cadmium-mercaptoacetate (C). IR spectra suggest that mercaptoacetic acid is adsorbed on CdS NCs surface in configuration (B)

Confronting IR spectra of CdSe NCs before and after the original ligands/ SnS_4^{4-} exchange procedure (Fig. 1.31), it is possible to notice the disappearance of all IR peaks. This is compatible with an inorganic ligand, transparent to IR frequencies. Similar results were obtained from SnS_4^{4-} , $\text{Sn}_2\text{S}_6^{4-}$ and S^{2-} on CdTe and CdSe-CdS NCs.

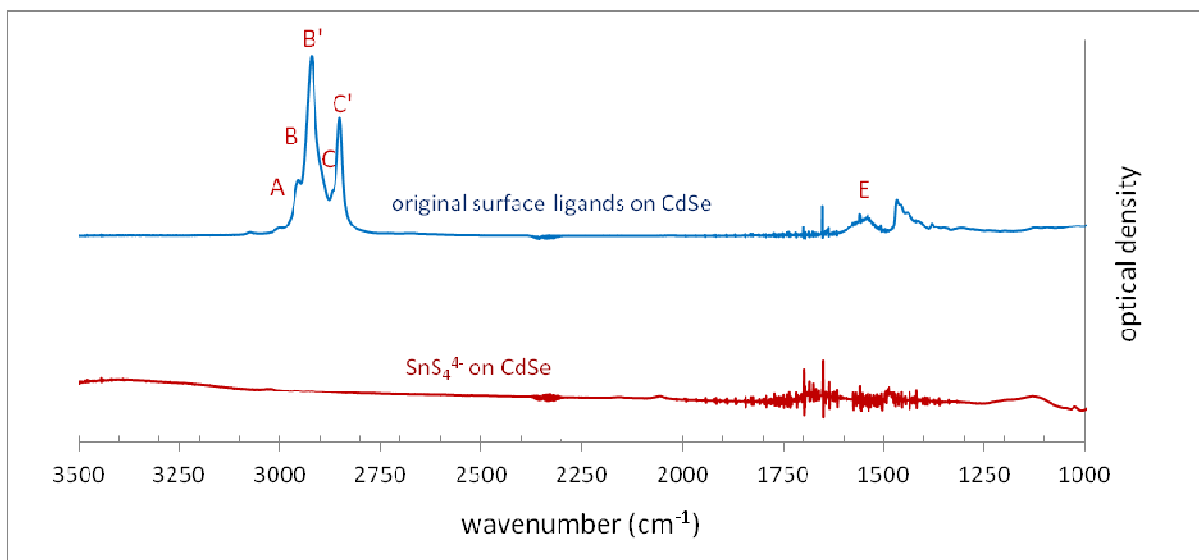


Fig. 1.31: IR absorption spectra of original surface ligands on CdSe NCs (blue) and new surface ligands (presumably SnS_4^{4-}) on CdSe NCs after ligand exchange procedure (red)

1.9.8 Effectiveness of ligands exchange procedures

Ligands exchange procedures were applied to CdSe, CdS, ZnSe, CdSe-CdS, CdSe-ZnSe, CdTe-CdS NCs and some of their alloys (CdSeS and CdZnSe NCs). Exchanging procedure were successful for:

- *Thiols*: (MAA and MPA) on all tested NCs; according to IR data, de-protonated MAA or MPA are bound on these NCs surface as acetic or propionic acid thiolates;
- *Inorganic ligands*: (SnS_4^{4-} , $\text{Sn}_2\text{S}_6^{4-}$ and S^{2-}): on CdSe, CdTe and CdSe-CdS only

1.9.9 Solubility in water and stability: effect of counter-ion

Inorganic ligands coated NCs were soluble in water and generally were stable for some days; after this time, they precipitated out of the solution and formed aggregates. MAA and MPA coated NCs can be solubilized in water after deprotonation of ligand's carboxylic group in basic environment. Two bases were used to rise the solution pH: (1) a 28-30% NH_3 solution in water; (2) NaOH solution in water. In case (1), the carboxylate counter-ion was NH_4^+ , in case (2) Na^+ . If NH_4^+ was used, thiol-stabilized NCs dissolved completely in a time ranging from some minutes to several weeks (CdTe-based NCs being the less resistant, CdS-based or CdS coated NCs being the more resistant). The resulting solution was transparent, without any noticeable precipitates (in case of dissolution of NCs containing Se or S), or with white precipitates (in case of dissolution of NCs containing Te). This cannot be explained by a photo-catalyzed reduction of thiol ligands (as observed by Aldana et al.⁷⁹), that should produce a coloured precipitate (clusters of NCs) and that should affect CdS and CdSe more than CdTe (thiol acts as a hole trap/electron donor: according to Wuister⁸⁰, thiol redox level is located inside CdSe E_G , but outside CdTe E_G – this influences also photoluminescence, as will be discussed in Chapter 2, paragraph 2.5.5). In Fig. 1.32 it is possible to compare the absorption spectrum of original ligands-coated CdTe NCs, dissolved in n-hexane, with the absorption spectra of MPA-coated CdTe NCs with NH_4^+ as counter ion, dissolved in water.

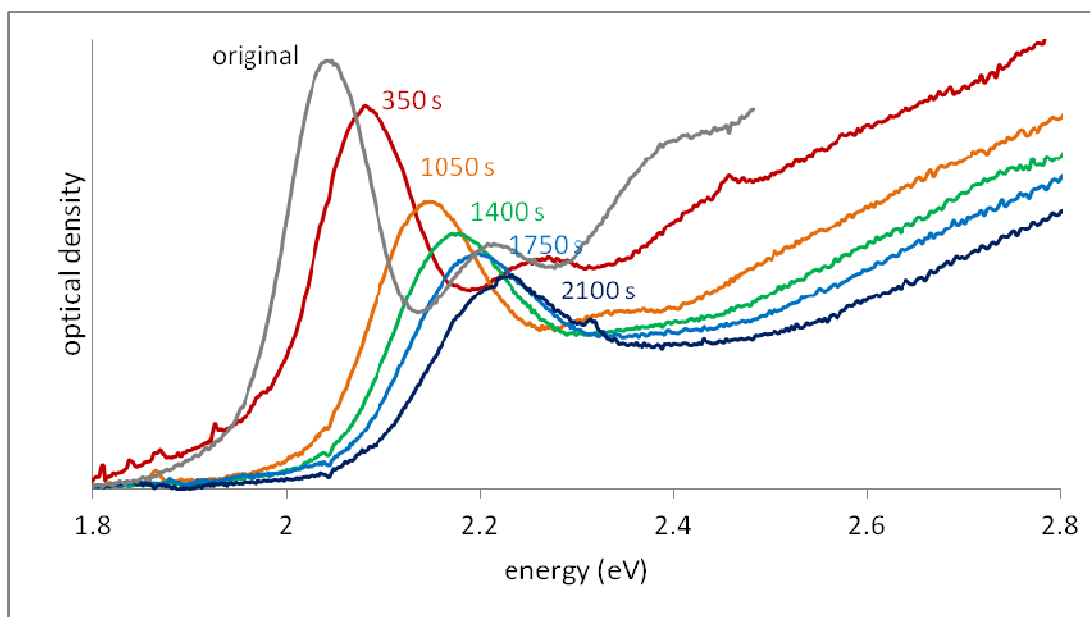


Fig 1.32: *absorption spectrum of CdTe NCs with original ligands (grey) compared to absorption spectra (collected after different times, shown in seconds over the plots) of CdTe NCs with MPA, NH_4^+ as counter ion (colored plots)*

An evolution of absorption spectra (hypsochromic shifts respect to the original) can be appreciated in a very short time: first exciton absorption energy shifts from 2.05 eV to 2.25 eV in about 35 minutes. This hypsochromic shift can be interpreted as a reduction of NCs dimension (dissolution). According to previously examined sizing curves (paragraph 1.8.2, p. 22), for these CdTe NCs (original diameter ≈ 1.9 nm) this hypsochromic shift means a diameter reduction of 0.5 nm (26% of original size) in about an

hour. In order to explain these observations, it can be speculated that when NCs were exposed to NH_4^+ they started dissolving due to the formation of $[\text{Cd}(\text{NH}_3)_6]^{2+}$, that is soluble in water⁸¹. Furthermore, one can suppose that in case of dissolution of NCs containing Se or S (clear solution), the other dissolution products are soluble in water, while in case of dissolution of Te-containing NCs, the other dissolution byproduct were not soluble in water (forming a white precipitate). If the clear solutions (dissolution of NCs containing Se or S) were heated, thus causing evaporation of ammonia, the formation of a white precipitate was noticed (most likely cadmium hydroxide, insoluble in water). It can also be supposed that CdS NCs and CdS-coated NCs (such as core-shells with CdS as shell material) were more resistant respect to this dissolution, since tellurides and selenides (such as CdTe and CdSe) tend to be less stable than the corresponding compounds of sulfur or oxygen⁸¹ (such as CdS or CdO).

1.10 Conclusions and Future Developments

1.10.1 Results summary

Different typologies of nanocrystals (single-phase, alloyed and complex heterostructures) were successfully synthesized using a simple, common systems: one solvent (1-octadecene) and two stabilizing ligands (oleate or octadecylphosphonate for cations, trioctylphosphine for anions). Only air-stable, safe reagents were utilized. Optical properties (absorption and fluorescence spectra and peak positions) were monitored during synthesis, shell growth and heat treatments; nanocrystal sizes were estimated and measured. It was possible to exchange the original ligands with shorter ones (thiols or inorganic ligands) and to simulate the bandgaps of complex nano-heterostructures via effective-mass approximation.

These results were propaedeutic to understand key relationships between synthesis parameters, dimensions, composition, surface ligands and optical properties of nanocrystals, thus laying the guidelines for the work described in the following chapters of this thesis.

1.10.2 Future developments

The semiconductor nanocrystals synthesized and characterized in this chapter will be used as “building blocks” for novel materials presented in Chapter 2 and Chapter 3. On the synthesis side, several improvement could be sought. Single surfactant, phosphine-free synthesis (already reported for single-phase NCs) could be developed for multi-phase NCs, lowering the synthesis costs and complexity; better synthesis techniques could be developed for CdTe-CdS system (aiming at spherical shapes); simpler synthesis techniques (one-step instead of multi-step) could be developed for high-quality core-shell systems.

References

- (1) Ekimov, A. I.; Onushchenko, A. A. *Journal of Experimental and Theoretical Physics* **1981**, *34*, 345-348.
- (2) Talapin, D. V.; Lee, J.-S.; Kovalenko, M. V.; Shevchenko, E. V. *Chemical Reviews* **2010**, *110*, 389-458.
- (3) Murray, C. B.; Noms, D. J.; Bawendi, M. G. *Journal of American Chemical Society* **1993**, *115*, 8706-8715.
- (4) Efros, A. L.; Rosen, M. *Annual Review of Materials Science* **2000**, *30*, 475-521.
- (5) Klimov, V. I. *Annual Review of Physical Chemistry* **2007**, *58*, 635-673.
- (6) Brus, L. *The Journal of Physical Chemistry* **1986**, *90*, 2555-2560.
- (7) Ekimov, A. I.; Hache, F.; Ricard, D.; Flytzanis, C.; Polytechnique, E.; Minchen, T. U. *Journal of the Optical Society of America B* **1993**, *10*, 100-107.
- (8) Bagga, A.; Chattopadhyay, P.; Ghosh, S. *Physical Review B* **2006**, *74*, 1-7.
- (9) Van Embden, J.; Jasieniak, J.; Gomez, D. E.; Mulvaney, P.; Giersig, M. *Australian Journal of Chemistry* **2007**, *38*, 457-471.
- (10) Issac, A.; Von_Borczykowski, C.; Cichos, F. *Physical Review B* **2005**, *71*, 161302.
- (11) Kraus, R. M.; Lagoudakis, P. G.; Müller, J.; Rogach, A. L.; Lupton, J. M.; Feldmann, J.; Talapin, D. V.; Weller, H. *The Journal of Physical Chemistry B* **2005**, *109*, 18214-18217.
- (12) Klimov, V. I. *The Journal of Physical Chemistry B* **2000**, *104*, 6112-6123.
- (13) Hill, N. A.; Whaley, K. B. *The Journal of Chemical Physics* **1994**, *100*, 2831.
- (14) Bullen, C.; Mulvaney, P. *Langmuir* **2006**, *22*, 3007-13.
- (15) Katari, J. E. B.; Colvin, V. L.; Alivisatos, A. P. *The Journal of Physical Chemistry* **1994**, *98*, 4109-4117.
- (16) Dorfs, D.; Eychmuller, A.; Rogach, A. L. In *Semiconductor Nanocrystal Quantum Dot*; SpringerWienNewYork, 2008; pp. 101-118.
- (17) Reiss, P.; Protière, M.; Li, L. *Small* **2009**, *5*, 154-68.
- (18) Kim, S.; Fisher, B.; Eisler, H.-J.; Bawendi, M. *Journal of the American Chemical Society* **2003**, *125*, 11466-7.
- (19) deMello Donegá, C. *Chemical Society reviews* **2011**, *40*, 1512-46.
- (20) Dorfs, D.; Franzl, T.; Osovsky, R.; Brumer, M.; Lifshitz, E.; Klar, T. A.; Eychmüller, A. *Small* **2008**, *4*, 1148-52.
- (21) Balet, L. P.; Ivanov, S. a; Piryatinski, a; Achermann, M.; Klimov, V. I. *Nano Letters* **2004**, *4*, 1485-1488.
- (22) Bernard, J. E.; Zunger, A. *Physical Review B* **1986**, *34*, 5992-5995.
- (23) Bernard, J. E.; Zunger, A. *Physical Review B* **1987**, *36*, pp. 3199-3228.
- (24) Protière, M.; Reiss, P. *Small* **2007**, *3*, 399-403.
- (25) Zhong, X.; Feng, Y.; Knoll, W.; Han, M. *Journal of the American Chemical Society* **2003**, *125*, 13559-63.
- (26) Bailey, R. E.; Nie, S. *Journal of the American Chemical Society* **2003**, *125*, 7100-6.
- (27) LaMer, V. K.; Dinegar, R. H. *Journal of the American Chemical Society* **1950**, *72*, 4847-4854.
- (28) Park, J.; Joo, J.; Kwon, S. G.; Jang, Y.; Hyeon, T. *Angewandte Chemie (Int. Ed.)* **2007**, *46*, 4630-60.
- (29) Murray, C. B.; Kagan, C. R.; Bawendi, M. G. *Annual Review of Materials Research* **2000**, *30*, 545-610.
- (30) Schmelzer, J. W. P. *Nucleation theory and applications*; Wiley-VCH, 2005.
- (31) Vossmeier, T.; Katsikas, L.; Giersig, M.; Popovic, I. G.; Diesner, K.; Chemseddine, A.; Eychmüller, A.; Weller, H. *The Journal of Physical Chemistry* **1994**, *98*, 7665-7673.
- (32) Talapin, D. V.; Rogach, A. L.; Kornowski, A.; Haase, M.; Weller, H. *Nano Letters* **2001**, *1*, 207-211.

- (33) Hambrock, J.; Becker, R.; Birkner, A.; Weiß, J.; Fischer, R. A. *Chemical Communications* **2002**, 68-69.
- (34) Jana, N. R.; Peng, X. *Journal of the American Chemical Society* **2003**, *125*, 14280-1.
- (35) Seo, W. S.; Jo, H. H.; Lee, K.; Park, J. T. *Advanced Materials* **2003**, *15*, 795-797.
- (36) Park, J.; An, K.; Hwang, Y.; Park, J.-G.; Noh, H.-J.; Kim, J.-Y.; Park, J.-H.; Hwang, N.-M.; Hyeon, T. *Nature Materials* **2004**, *3*, 891-5.
- (37) Hines, M. a; Guyot-Sionnest, P. *The Journal of Physical Chemistry* **1996**, *100*, 468-471.
- (38) Danek, M.; Jensen, K. F.; Murray, C. B.; Bawendi, M. G. *Chemistry of Materials* **1996**, *8*, 173-180.
- (39) Van Embden, J.; Jasieniak, J.; Mulvaney, P. *Journal of the American Chemical Society* **2009**, *131*, 14299-309.
- (40) Peng, X.; Schlamp, M. C.; Kadavanich, A. V.; Alivisatos, a P. *Journal of the American Chemical Society* **1997**, *119*, 7019-7029.
- (41) Mekis, I.; Talapin, D. V.; Kornowski, A.; Haase, M.; Weller, H. *The Journal of Physical Chemistry B* **2003**, *107*, 7454-7462.
- (42) Bae, W. K.; Char, K.; Hur, H.; Lee, S. *Chemistry of Materials* **2008**, *20*, 531-539.
- (43) Jang, E.; Jun, S.; Pu, L. *Chemical Communications* **2003**, 2964-5.
- (44) Reiss, P.; Bleuse, J.; Pron, A. *Nano Letters* **2002**, *2*, 781-784.
- (45) Dabbousi, B. O.; Rodriguez-Viejo, J.; Mikulec, F. V.; Heine, J. R.; Mattoussi, H.; Ober, R.; Jensen, K. F.; Bawendi, M. G. *The Journal of Physical Chemistry B* **1997**, *101*, 9463-9475.
- (46) Xie, R.; Kolb, U.; Li, J.; Basché, T.; Mews, A. *Journal of the American Chemical Society* **2005**, *127*, 7480-8.
- (47) Li, J. J.; Wang, Y. A.; Guo, W.; Keay, J. C.; Mishima, T. D.; Johnson, M. B.; Peng, X. *Journal of the American Chemical Society* **2003**, *125*, 12567-75.
- (48) Yu, W. W.; Peng, X. *Angewandte Chemie (International ed. in English)* **2002**, *41*, 2368-2371.
- (49) Peng, Z. A.; Peng, X. *Journal of the American Chemical Society* **2001**, *123*, 183-4.
- (50) Van Embden, J.; Mulvaney, P. *Langmuir* **2005**, *21*, 10226-33.
- (51) Yang, Y. A.; Wu, H.; Williams, K. R.; Cao, Y. C. *Angewandte Chemie (Int. Ed.)* **2005**, *44*, 6712-5.
- (52) Qu, L.; Peng, Z. A.; Peng, X. *Nano Letters* **2001**, *1*, 333-337.
- (53) Bullen, C. R.; Mulvaney, P. *Nano Letters* **2004**, *4*, 2303-2307.
- (54) Li, L. S.; Pradhan, N.; Wang, Y.; Peng, X. *Nano Letters* **2004**, *4*, 2261-2264.
- (55) Liu, H.; Owen, J. S.; Alivisatos, A. P. *Journal of the American Chemical Society* **2007**, *129*, 305-12.
- (56) Kovalenko, M. V.; Bodnarchuk, M. I.; Zaumseil, J.; Lee, J.-S.; Talapin, D. V. *Journal of the American Chemical Society* **2010**, *132*, 10085-92.
- (57) Dong, A.; Ye, X.; Chen, J.; Kang, Y.; Gordon, T.; Kikkawa, J. M.; Murray, C. B. *Journal of the American Chemical Society* **2011**, *133*, 998-1006.
- (58) Talapin, D. V.; Murray, C. B. *Science* **2005**, *310*, 86-9.
- (59) Adachi, S. In *Properties of Group-IV, III-V and II-VI Semiconductors*; John Wiley & Sons, Ltd, 2005; pp. 1-21.
- (60) Adachi, S. In *Properties of Group-IV, III-V and II-VI Semiconductors*; John Wiley & Sons, Ltd, 2005; pp. 147-172.
- (61) Bang, J.; Park, J.; Lee, J. H.; Won, N.; Nam, J.; Lim, J.; Chang, B. Y.; Lee, H. J.; Chon, B.; Shin, J.; Park, J. B.; Choi, J. H.; Cho, K.; Park, S. M.; Joo, T.; Kim, S. *Chemistry of Materials* **2010**, *22*, 233-240.
- (62) Adachi, S. In *Properties of Group-IV, III-V and II-VI Semiconductors*; John Wiley & Sons, Ltd, 2005; pp. 103-145.

- (63) Adachi, S. In *Properties of Group-IV, III-V and II-VI Semiconductors*; John Wiley & Sons, Ltd, 2005; pp. 195-209.
- (64) Kovalenko, M. V.; Scheele, M.; Talapin, D. V. *Science* **2009**, *324*, 1417-20.
- (65) Nag, A.; Kovalenko, M. V.; Lee, J.-S.; Liu, W.; Spokoyny, B.; Talapin, D. V. *Journal of the American Chemical Society* **2011**, *133*, 10612-20.
- (66) Yu, W. W.; Qu, L.; Guo, W.; Peng, X. *Chemistry of Materials* **2003**, *15*, 2854-2860.
- (67) Jasieniak, J.; Smith, L.; Van Embden, J.; Mulvaney, P.; Califano, M. *The Journal of Physical Chemistry C* **2009**, *113*, 19468-19474.
- (68) Schooss, D.; Mews, A.; Eychmüller, A.; Weller, H. *Physical Review B* **1994**, *49*, 17072-17078.
- (69) Horley, P.; Gorley, V.; Gorley, P.; Gonzalezhernandez, J.; Vorobiev, Y. *Thin Solid Films* **2005**, *480-481*, 373-376.
- (70) Nikesh, V. V.; Lad, A. D.; Kimura, S.; Nozaki, S.; Mahamuni, S. *Journal of Applied Physics* **2006**, *100*, 113520.
- (71) Reiss, P.; Carayon, S.; Bleuse, J. *Physica E* **2003**, *17*, 95-96.
- (72) Reiss, P. *Synthetic Metals* **2003**, *139*, 649-652.
- (73) Talapin, D. V.; Mekis, I.; Götzinger, S.; Kornowski, A.; Benson, O.; Weller, H. *The Journal of Physical Chemistry B* **2004**, *108*, 18826-18831.
- (74) Demenezes, F.; Brasiljr, A.; Moreira, W.; Barbosa, L.; Cerar, C.; Ferreira, R.; Defarias, P.; Santos, B. *Microelectronics Journal* **2005**, *36*, 989-991.
- (75) Dirin, D. N.; Vasiliev, R. B.; Sokolikova, M. S.; Gaskov, A. M. *Inorganic Materials* **2010**, *47*, 23-28.
- (76) Wu, N.; Fu, L.; Su, M.; Aslam, M.; Wong, K. C.; Dravid, V. P. *Nano Letters* **2004**, *4*, 383-386.
- (77) Lee, D. H.; Condrate, R. A.; Lacourse, S. W. C. *Journal of Materials Science* **2000**, *35*, 10.
- (78) Shukla, N. *Journal of Magnetism and Magnetic Materials* **2003**, *266*, 178-184.
- (79) Aldana, J.; Wang, Y. a; Peng, X. *Journal of the American Chemical Society* **2001**, *123*, 8844-50.
- (80) Wuister, S. F.; Donega, C. D. M.; Meijerink, A. *Journal of Physical Chemistry B* **2004**, *108*, 17393-17397.
- (81) Greenwood, N. N.; Earnshaw, A. *Chemistry of the Elements, 2nd ed.*; Reed Educational and Professional Publishing Ltd., 1997.

CHAPTER 2

Semiconductor Nanocrystals as phosphors in LED-based white lighting devices

This chapter presents part of a research work (not entirely covered in this thesis), whose aim is to combine a blue or UV Light Emitting Device (used as the optical excitation source) with a semiconductor NCs/polymer composite lens (used as green, yellow and red phosphors) to obtain a cost effective white lighting device.

The introduction of this chapter (paragraphs 2.1 - 2.2) deals with basic Light Emitting Diodes concepts; experimental work, focused on characterization and optimization of nanocrystals optical properties (absorption spectra, emission wavelength and fluorescence quantum yield) is described in paragraphs 2.3 - 2.4; finally (paragraphs 2.5 - 2.6) relations between optical properties, nanostructure and surface ligands are presented and discussed.

Introduction

2.1 Light Emitting Diodes

Light Emitting Diodes (LEDs), first introduced as technological application of electroluminescence in early 1960s¹, can be simply defined^{2,3} as *p-n* junctions that emit light when forward-biased: negative and positive charge carriers recombine within the junction, releasing energy in the form of photons. The color of the emitted light (related to the frequency ν of the released photon) depends on the energy gap E_G of the semiconductor used in the junction, according to the well known Planck-Einstein relation:

$$h\nu = E_G \quad (2.1)$$

2.1.1 White emission from LED-based devices

LEDs are promising replacements for conventional light sources, thanks to their high efficiency, reliability and long life time⁴. However, even if commercial LEDs are available in a broad range of pure colors, mixed colors, as white, require combining at least two pure colors⁵. Two approaches are possible to generate a white emission:

- (i) Mixing red, green and blue emitting LEDs. This approach show high efficiency and good color rendering index, but elevate fabrication cost and complexity^{4,5}
- (ii) Combining UV or blue emitting LEDs with phosphors^{6,7}. The LED emitter is used as the optical excitation source; some of its light is absorbed by the phosphors, that re-emit shorter frequencies (green, yellow and red), producing white light. This approach seems to be more promising for the development of simple and cost effective white illumination devices⁴.

2.1.2 White emission from LED/phosphors devices : state of the art

In commercially available devices, a blue emitting gallium nitride (GaN)³ or indium-gallium nitride (InGaN)⁸ LED is used as the excitation source and cerium-doped yttrium-aluminum granates (YAG : Ce+3) as yellow phosphors⁴. This mixture of blue and yellow produces white light; nevertheless, the color rendering index is sometimes low, due to the lack of red emission, and the color purity varies with input power⁴. To overcome these problems, near-UV InGaN emitters can be used⁷, and different typologies of phosphors have been evaluated:

- (i) other inorganic formulations, such as silver or copper/aluminum doped metal chalcogenides (ZnS:Ag, ZnS:Cu,Al and ZnCdS:Ag) or europium/manganese-doped alkaline earth silicates (Sr₃MgSi₂O₈:Eu,Mn), used as blue, green, yellow and red emitters^{6,7,9}.
- (ii) organic dyes¹⁰ or π -conjugated polymers¹¹

2.2 Semiconductor Nanocrystals as Phosphors

Instability and narrow absorption properties of organic phosphors and broad emission spectra of inorganic ones makes sometimes difficult to access precisely the desired color ⁵. Semiconductor nanocrystals have been regarded as promising candidates thanks to their high fluorescence quantum yield, size-tunable bandgap, narrow emission spectrum (FWHM \approx 30 nm compared to 50-100 nm of inorganic phosphors ⁹) and broad absorption spectrum ^{4,5}. This last feature (high density of absorbing states from their bandgap to UV region) permits the simultaneous excitation of different wavelength-emitting phosphors with a single light source.

2.2.1 Polymer/NCs composite materials

Several groups ^{4,5,12,13} showed the possibility to incorporate semiconductor nanocrystals inside different polymeric matrix (poly-methyl and poly-lauryl methacrylates). The resulting composite material is a promising candidate to be used as down-converting phosphor, if coupled with commercial blue or UV LED emitter, to obtain a cost effective white (or color-controlled) light emission device, as schematized in Fig. 2.1.

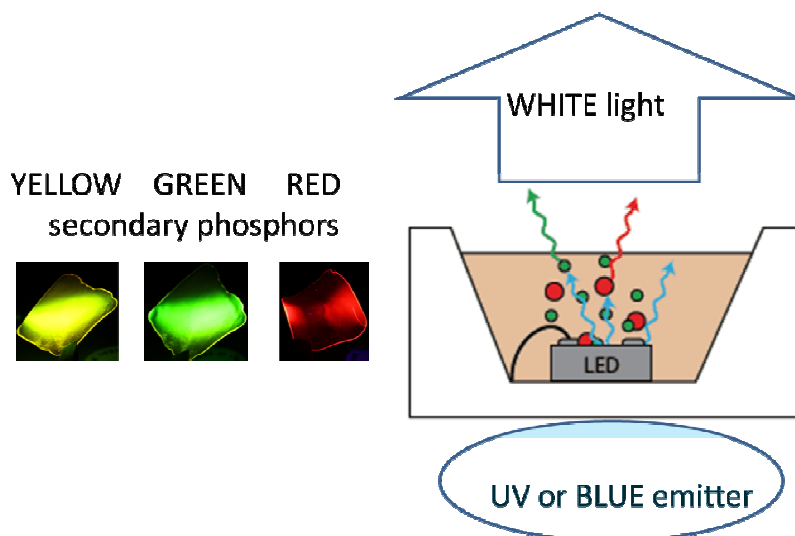


Fig. 2.1: example of a white lighting device based on blu/UV LED emitter coupled with secondary phosphors lenses (yellow, green and red emitting composite materials based on polymer/semiconductor NCs)

Experimental Section

2.3 Fluorescence Properties Characterization

2.3.1 Materials

3-mercaptopropionic acid (MPA, >99%), methanol (>99.8%), ethanol (>99.5%), acetone (>99.8%), n-hexane (>95%), fluorescein (fluorescence grade), rhodamine 6G (fluorescence grade), sodium hydroxide (NaOH, >97%), chloroform (99%), chlorobenzene (99%), polymethylmetacrylate pellets (PMMA, Mw =120,000), were obtained from Sigma-Aldrich. The following compounds were synthesized in the form of colloidal nanocrystals, according to techniques described in Chapter 1:

- CdS, CdS-ZnS and Cd_xZn_{1-x}S ($\lambda_{PL} < 500 \text{ nm}$)
- CdSe-ZnSe, Cd_xZn_{1-x}Se-ZnSe, CdSe-CdS, CdSe_xS_{1-x}-CdS ($500 < \lambda_{PL} < 630 \text{ nm}$)
- CdTe and CdTe-CdS ($\lambda_{PL} > 600 \text{ nm}$)

2.3.2 Fluorescence wavelength measurement

Photoluminescence spectra of diluted colloidal solutions were acquired through an OceanOptics SD2000 spectrophotometer, in the wavelength range between 250 and 850 nm, with a resolution of 0.36 nm, using a UV LED (emission wavelengths: 300 and 320 nm) as excitation source. Fluorescence wavelength was determined from peak position of photoluminescence spectra, fitted with gaussian or log-normal curves using ThermoGalactic Grams/AI 7.02.

2.3.3 Fluorescence quantum yield measurement

Fluorescence Quantum Yield (QY) of the samples was determined according to the comparative method described by Williams et al.¹⁴. Using a standard reference with known QY (QY_R), it was possible to calculate the QY of the samples (QY_S):

$$QY_S = \frac{F_S}{F_R} \cdot \frac{A_R}{A_S} \cdot \frac{I_R}{I_S} \cdot \frac{n_S^2}{n_R^2} \cdot QY_R \quad (2.2)$$

where F_R and F_S are the integrated fluorescence intensities, A_R and A_S the absorbances at the excitation wavelength, I_R and I_S the relative intensities of the exciting light and n_R and n_S the refractive indexes (of the reference and of the sample respectively). Photoluminescence spectra were acquired through an OceanOptics SD2000 spectrophotometer, equipped with an Oriel/Cornerstone 130 monochromator; a Newport model 6266 – 360 W Xenon lamp was used as excitation source. Measures were performed on diluted colloidal solution (optical density at excitation wavelength < 0.1) to minimize re-absorption effects. Commercial dyes (rhodamine 6G and fluorescein, with a reported QY of 68% and 78% respectively) in ethanol were used as standard references. From three to six different excitation wavelengths λ_{exc} (400 nm, 420 nm, 460 nm, 500 nm, 520 nm, 540 nm) were used for each sample (depending on sample's absorption properties); rhodamine 6G was used as standard

reference for $\lambda_{exc} = 500, 520$ and 540 nm; fluorescein for $\lambda_{exc} = 400, 420$ and 460 nm; the final QY was averaged from the obtained values.

2.3.4 Ligands exchange

Original ligands were exchanged with MPA to make NCs water-soluble and to measure QY variation.

General procedure: 0.1 mmol of nanoparticles were washed twice with methanol, precipitated with acetone and re-dissolved in 4 ml of n-hexane; 0.1 mmol of new ligand (MPA) were added; the NCs started aggregation/flocculation almost immediately; the suspension was vigorously stirred for 30-60 minutes. Then the suspension was divided in two test tubes; 2 ml of n-hexane and 2 ml of acetone were added to each tube, vigorously mixed, then centrifuged for several minutes. At this point, a colored precipitate appeared in the bottom of the test tubes: the precipitate was then washed and centrifuged/precipitated twice with n-hexane, then it was dispersed in 4 ml of 0.1 M NaOH solution in water.

2.4 Polymer/Nanocrystals Composite Fabrication

NCs with desired emission wavelength and fluorescence QY were blended into polymers by dissolving NCs (with original surface ligands) and PMMA pellets into chloroform or chlorobenzene (as shown in Fig. 2.2, left); the mixture was then tape-casted or spin coated on glass substrates (Fig 2.2, center); the solvent was allowed to evaporate at room temperature, leaving the NCs homogeneously dispersed inside a solid, transparent polymer lens (shown in Fig 2.2, right). Fabrication details, optical characterization of the lenses and LED-lens coupling are not object of this work.

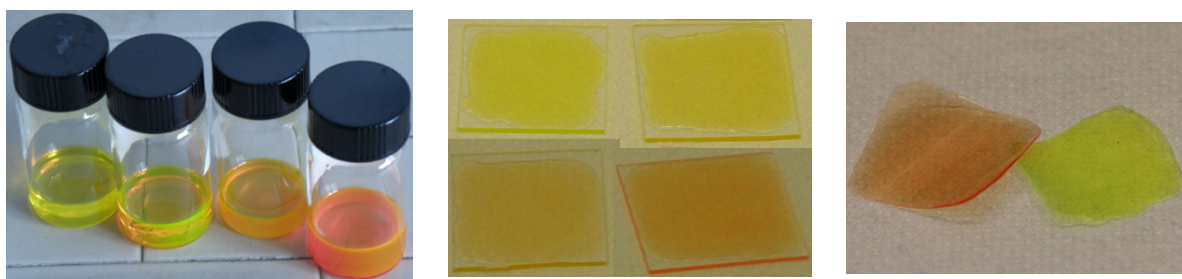


Fig. 2.2: *fabrication steps of a NCs/polymer composite (credit to S. Zanon):*

Left: solution of colloidal NCs and polymer pellets in chloroform

Center: mixture casted on glass substrates

Right: transparent polymer matrix lenses

Results and Discussion

2.5 Results

2.5.1 Fluorescence wavelength and fluorescence quantum yield

Colloidal nanocrystals with an emission wavelength ranging from 400 nm to 700 nm, covering all the visible spectrum were successfully synthesized; the highest fluorescence quantum yields were achieved between 530 and 600 nm (green to orange/red), as it can be noticed in Figs. 2.3 – 2.4.

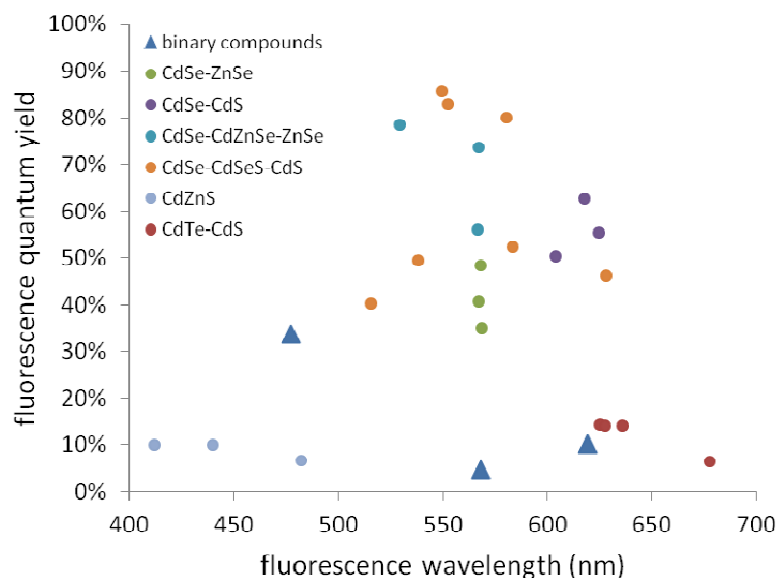


Fig. 2.3: fluorescence QY as a function of fluorescence wavelength for all synthesized nanocrystals

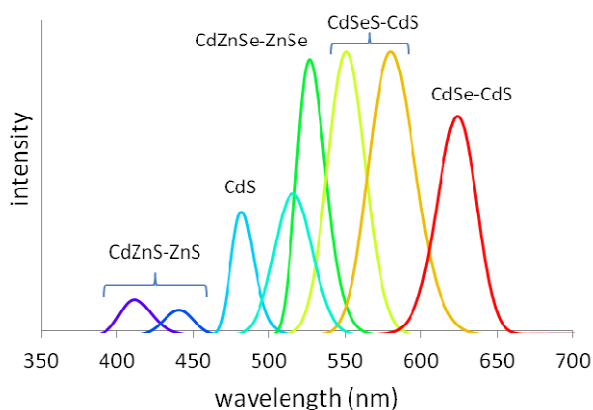


Fig. 2.4: fluorescence spectra of some NCs emitting in the visible range. (Intensities are scaled according to QY)

2.5.2 Shell growth and diffusion influence on fluorescence wavelength

Growth of ZnSe and CdS shells on CdSe NCs and growth of CdS shell on CdTe caused a bathochromic shift of first absorption peak and fluorescence peak (corresponding to a decrease of nanocrystal apparent bandgap), as previously discussed in Chapter 1. Alloying between core and shell materials in CdSe-ZnSe and CdSe-CdS core-shells nanoparticles caused hypsochromic shifts of the fluorescence peaks (corresponding to an increase in the nanocrystal apparent bandgap), as previously discussed in Chapter 1.

2.5.3 Shell growth influence on fluorescence quantum yield

Both CdS and ZnSe shells causes an increase in the original CdSe fluorescence QY; this increase appears to be related to shell thickness, as shown in Fig. 2.5. An initial decrease is noticeable after the growth of the first atomic layer, followed by a linear increase up to a maximum (QY \approx 48%, for ZnSe shell, thickness \approx 1.2 nm; QY \approx 62% for CdS shell, thickness \approx 1.3 nm); after this maximum, QY decreases again to 35% and 57%, for ZnSe and CdS shell respectively.

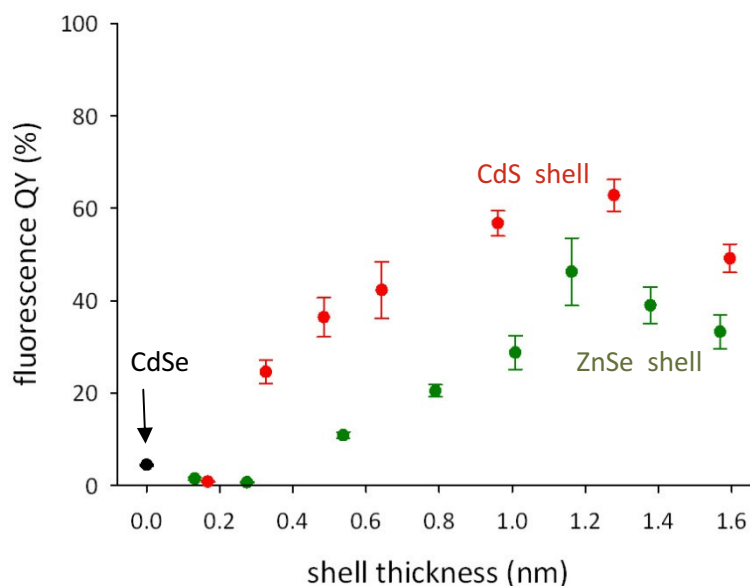


Fig. 2.5: fluorescence QY as a function of shell thickness for CdSe-ZnSe (green) and CdSe-CdS (red) core-shell NCs

The original QY of CdSe NCs is low, due to the presence of surface states (that act as non-radiative recombination pathways). After overgrowing an inorganic shell, initially these non-radiative recombination sites are covered, leading to an increase of QY; then the difference in lattice parameters between the two materials results in local strain at the interface and formation of stacking faults (that act, again, as non-radiative recombination sites), leading to a decrease of QY. A similar trend was already observed in literature for CdSe-CdS¹⁵ and CdSe-ZnS¹⁶ systems. The difference observed for different shell material is likely due their different lattice mismatch respect to core material: CdS shell on CdSe (lattice mismatch \approx 4.4 %¹⁷) leads to an higher fluorescence QY respect to a ZnSe shell (lattice mismatch \approx 6.7 %¹⁷) at the same shell thickness; nevertheless, also the different

band offsets cannot be ignored. Both systems are *quasi-Type-I* core-shells (see Chapter 1, paragraph 1.2.2-d, p. 10): CdSe-CdS does not confine negative charges in the core (while CdSe-ZnSe does); on the other hand, CdSe-CdS confines positive charges in the core (while CdSe-ZnSe does not); this implies different electron or hole distribution functions at the same shell thickness, effecting radiative (probability function overlaps) or non-radiative (trap sites or redox species on the surface) recombination pathways.

2.5.4 Diffusion influence on fluorescence quantum yield

As previously discussed, an inorganic shell increases fluorescence QY (covering non-radiative recombination sites on surface), but lattice mismatch between core and shell materials leads to interface strains and formation of defects (that cause a decrease of QY). It is possible to reduce local lattice mismatch by applying a heat treatment that causes a mutual diffusion of core and shell materials, creating an alloyed layer. This leads to an initial increase of fluorescence QY, as shown in Fig. 2.6. After this initial increase, fluorescence QY decreases again, most likely due to the formation of a complete alloyed, one-phase structure (loss of the core-shell structure, and consequently access of the charge carriers to the defective surface structure); the effect is more noticeable at higher temperatures, where diffusion is faster.

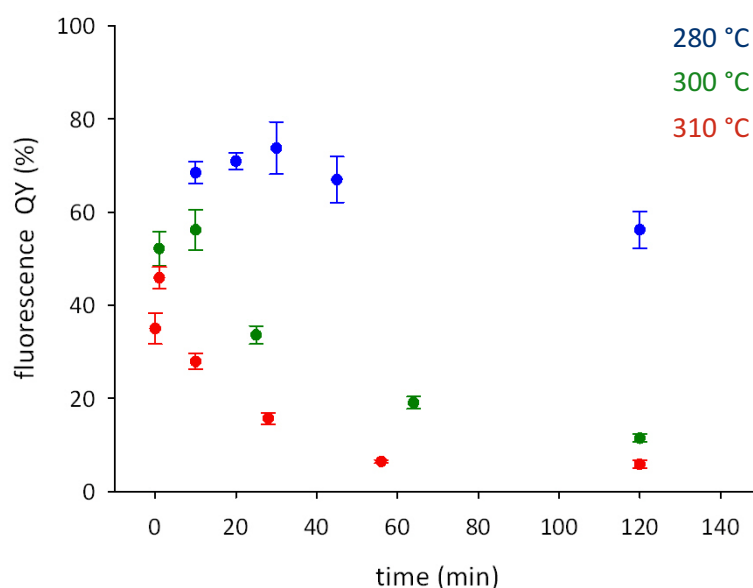


Fig. 2.6: fluorescence QY as a function heat treatment time, at different temperature: 280 °C (blue), 300 °C (green) and 310 °C (red) for CdSe-ZnSe core-shell NCs

2.5.5 Surface ligands influence on fluorescence quantum yield

Effect of MPA was evaluated on different typologies of NCs, as shown in Fig. 2.7. NCs with original surface ligands (oleic acid and trioctylphosphine) behave as previously discussed: CdSe NCs have low fluorescence QY ($\approx 5\%$); core-shell NCs higher (CdSe-ZnSe: QY $\approx 35\%$, CdSe-CdS: QY $\approx 57\%$); partially alloyed core-shells show the highest measured QYs (Cd_xZn_{1-x}Se-ZnSe: QY $\approx 79\%$; CdSe_xS_{1-x}-CdS:

QY \approx 86 %). The situation changes when original surface ligands are replaced with MPA: CdSe does not show any measurable fluorescence; both core-shell systems show measurable fluorescence QYs; not alloyed CdSe-CdS seems to behave better than not alloyed CdSe-ZnSe, while the fluorescence is nearly completely quenched in alloyed CdSe-CdS NCs, oppositely to alloyed CdSe-ZnSe ones, that retain about 75% of their original QY value.

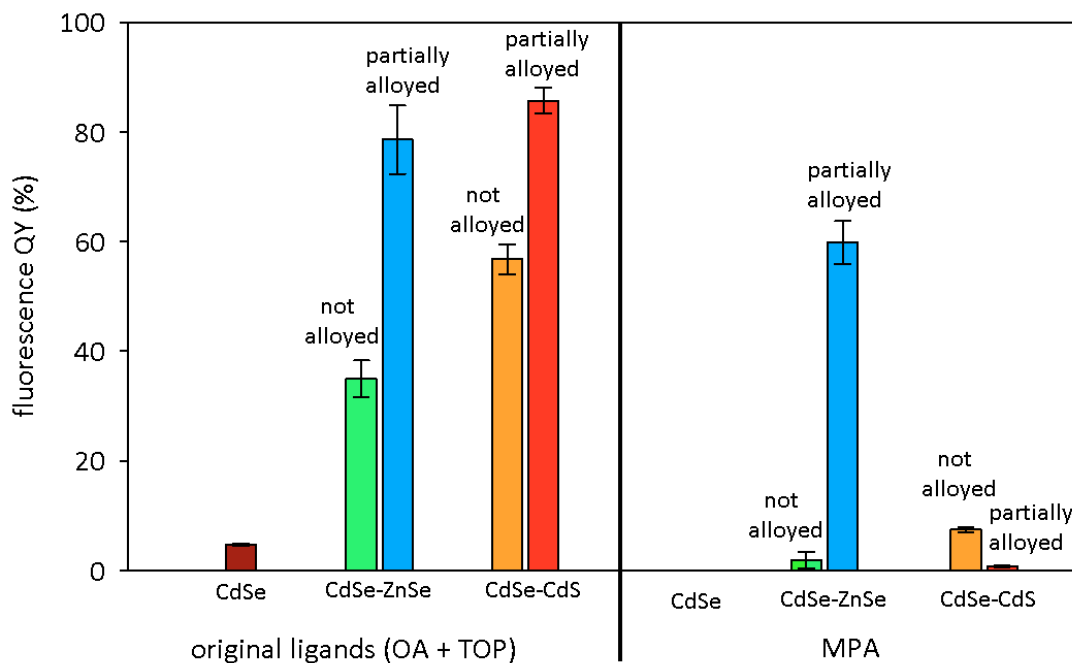


Fig. 2.7: fluorescence QY of different NCs, with original ligands (left) or MPA (right) on their surface

Thiols (such as MPA) are known to quench fluorescence by introducing trap states on the surfaces¹⁸. Shell material, as already discussed, confines charge carriers inside the heterostructure, insulating them from surface. Alloyed CdSe-ZnSe system shows the best QY with surface thiols, most likely due the high conduction band offset between CdSe and ZnSe, that insulates electron inside the structure. Also non-alloyed CdSe-ZnSe system should behave similarly; instead it shows a low QY in presence of MPA. This can be motivated by the relative core/shell diameter ratio: in the studied non-alloyed CdSe-ZnSe system (with a core/shell volume ratio of 1/7), the initial diameter ratio (core)/(core+shell) is about 1/2. After diffusion of zinc into CdSe lattice and cadmium into ZnSe lattice, it is possible to view: (i) the core as a Cd-rich CdZnSe alloy, that become smaller while the diffusion move forward; (ii) the shell as a Zn-rich CdZnSe alloy, that become thicker. Therefore, the effective (core)/(core+shell) diameter ratio becomes smaller than the original one, as the diffusion goes on. As a results, it is possible to imagine the electrons as: (1) confined into a large core by a large conduction band offset, but a thin shell - in the “non-alloyed” situation (i.e. electrons are likely able to tunnel and be scavenged by the surface thiols); (2) confined by a smaller conduction band offset, but by a large shell - in the “alloyed” situation (i.e. electrons are not likely able to tunnel to the surface). On the other hand, CdSe-CdS (that does not insulate electron inside the structure due small conduction band offset between CdSe and CdS) seems to not retain its high fluorescence QY if MPA is on its surface. In this situation, one can suppose that an alloyed system behaves even worse: alloying lowers its already small conduction band offset, allowing the electron to tunnel and be captured by surface traps.

It is also possible to evaluate the effect of different shell thickness and composition on the same CdSe core, with original ligands or in presence of thiols, as shown in Fig. 2.8. With original surface ligands (oleic acid and trioctylphosphine), as previously discussed, the low fluorescence QY ($\approx 5\%$) of bare CdSe NCs can be enhanced overgrowing a CdS shell; QY increases to a maximum (in this case for 4 ML-thick shell – QY $\approx 60\%$), then decreases due to formation of stacking faults.

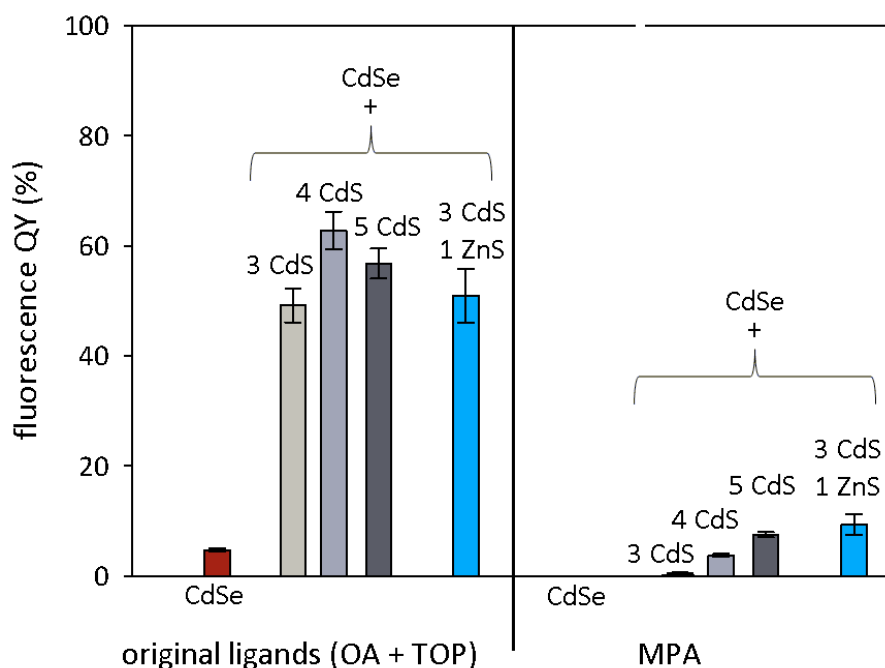


Fig 2.8: fluorescence QY of CdSe NCs (red), CdSe-CdS core shell with different shell thickness (grey bars: numbers refer to shell thickness, expressed in MLs) and CdSe-CdS-ZnS core-multishell (blue bar: numbers refer to shell thickness, expressed in MLs, with original ligands (left) or MPA (right) on their surface.

It can be noticed that a mixed CdS-ZnS shell, at the same nominal thickness, grants a lower QY ($\approx 50\%$) than a CdS shell ($\approx 60\%$). This can be motivated by the larger lattice mismatch of the mixed composition shell (lattice mismatch between ZnS and CdSe $\approx 11\%$, between CdS and ZnS $\approx 6.8\%$ - while between CdSe and CdS is only $\approx 4\%$), that introduces additional interface stresses and possible defects in the structure. The situation, again, changes in presence of MPA on the surface: CdSe, as expected, does not show any measurable fluorescence, while QY in CdSe-CdS NCs seems proportional to shell thickness (better electron confining inside the heterostructure); in this case, mixed shell seems to behave better at the same nominal thickness (confront “4 CdS” – QY $\approx 4\%$ - with “3 CdS – 1 ZnS” – QY $\approx 10\%$ - in Fig. 2.8). This can be motivated by a greater conduction band offset between ZnS and CdSe, that insulates electrons from surface thiols.

Finally, it was observed that fluorescence QY of CdTe NCs is not influenced negatively by surface thiols, as it can be noticed in Fig. 2.9-A. On the contrary, QY of CdTe NCs increases in presence of MPA, showing an opposite behavior respect to CdSe NCs (where fluorescence QY is completely quenched in presence of MPA). According to Wuister¹⁹, redox level of thiols should be located above the top of CdSe VB, but below the top of CdTe VB (positions of these bands respect to vacuum level, according to Adachi^{20,21}, are shown in Fig 2.9-B); that being so, the thiol redox level can act as trap inside the CdSe bandgap, competing with radiative recombination events; this does not apply to CdTe. The increase of QY after original ligands exchange with MPA (observed in this work for CdTe NCs) can be motivated by a better coverage of surface states by MPA respect to original ligands (oleic acid and especially trioctylphosphine), that have a larger steric effect than smaller thiols.

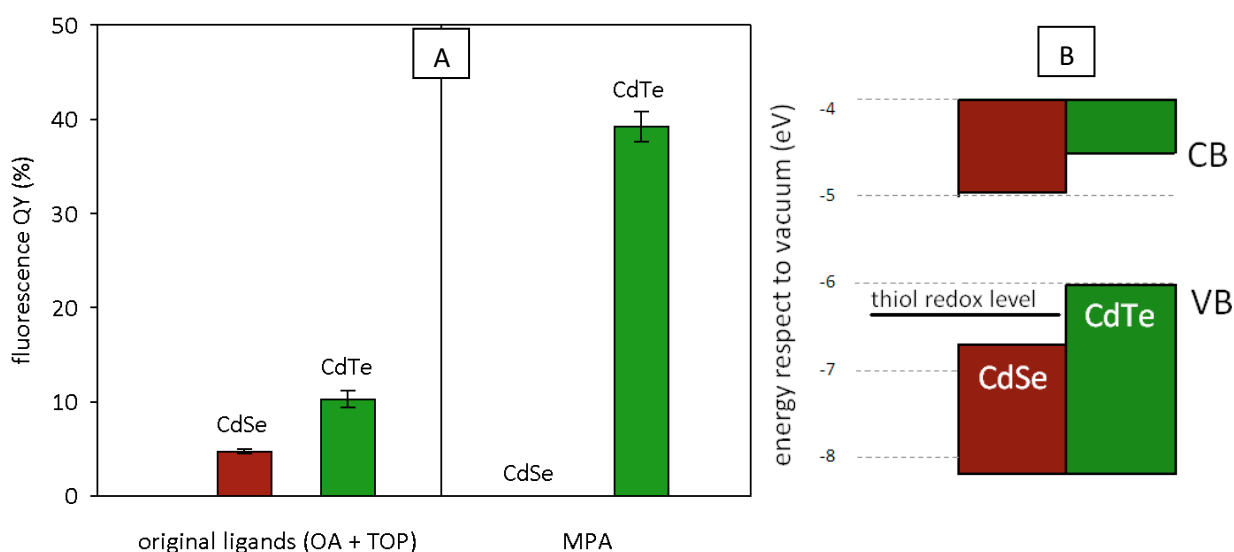


Fig. 2.9: (A) fluorescence QY of CdSe NCs (red) and CdTe NCs (green), with original ligands (left) or MPA (right) on their surface

(B) bulk CdSe (red) and CdTe (green) band positions respect to vacuum energy level; thiol redox level (black horizontal line), according to Wuister¹⁹, is inside CdSe forbidden energy bandgap.

2.6 Conclusion and Future Developments

2.6.1 Results summary

Different typologies of NCs with desired optical properties (color – i.e. fluorescence wavelength, and efficiency – i.e. fluorescence quantum yield) were successfully synthesized and characterized.

Fluorescence wavelength (related to phosphor's color) was tuned by:

- (i) changing the size of single-phase NCs
- (ii) modifying the composition of single phase NCs
- (iii) changing one of more materials, or their relative sizes in multi-phase NCs
- (iv) mutual diffusion of core and shell materials

Fluorescence quantum yield (related to phosphor's conversion efficiency) was tuned by:

- (i) overgrowing different thickness and composition inorganic shell
- (ii) mutual diffusion of core and shell materials
- (iii) replacing original surface organic ligands with different ones

Among synthesized objects, the best formulations tested were CdSe-based, partially alloyed core-shell NCs. CdS based shells gave better results in wavelength control and achievable QY, while ZnSe based shell gave higher QYs with thiols as surface ligands. Using these formulations, it was possible to cover efficiently a wide range of the visible spectrum: NCs with emission wavelength between 520 and 610 nm, and state of the art QYs (between 60% and 85%) were successfully obtained.

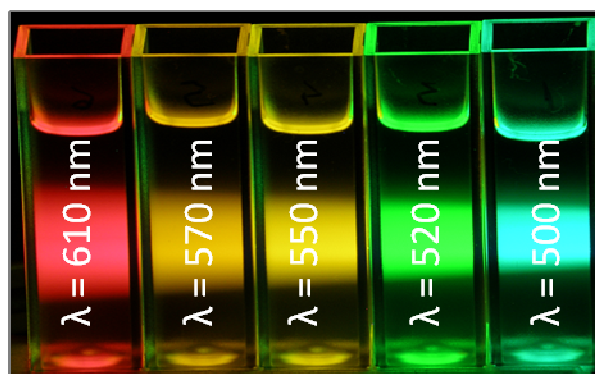


Fig. 2.10: CdSeS-CdS partially alloyed core-shell NCs in colloidal solution, excited with UV light ($\lambda = 360$ nm), displaying different fluorescence wavelengths thanks to combined effects of different size and composition

2.6.2 Future developments: NCs/polymer composite material

After blending different typologies of NCs into PMMA matrix, lenses with different emission wavelengths were obtained. Example of these solid lenses, excited with UV light (360 nm) and emitting at different wavelengths are displayed in Fig. 2.11. In the future, these lenses could be characterized, tested and integrated as secondary phosphors into LED-based white lighting system.

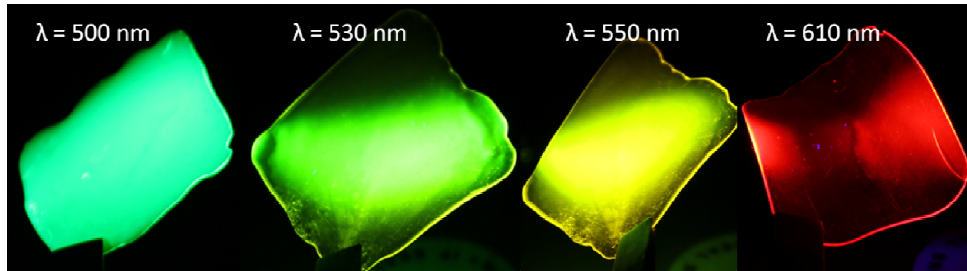


Fig. 2.11: *CdSeS-CdS partially alloyed core-shell NCs embedded in solid PMMA lenses, excited with 360 nm light, displaying different fluorescence wavelengths*

References

- (1) Black, J.; Lockwood, H.; Mayburg, S. *Journal of Applied Physics* **1963**, *34*, 178.
- (2) Ponce, F. A.; Bour, D. P. *Nature* **1997**, *386*, 351-359.
- (3) Steigerwald, D.; Rudaz, S.; Liu, H.; Kern, R. S.; Gotz, W.; Fletcher, R. *Jom* **1997**, *49*, 18-23.
- (4) Chung, W.; Park, K.; Yu, H. J.; Kim, J.; Chun, B.-H.; Kim, S. H. *Optical Materials* **2010**, *32*, 515-521.
- (5) Lee, J.; Sundar, V. C.; Heine, J. R.; Bawendi, M. G.; Jensen, K. F. *Advanced Materials* **2000**, *12*, 1102-1105.
- (6) Lee, S.; Seo, S.-Y. In *Proceedings of SPIE*; SPIE, 2001; Vol. 4445, pp. 82-92.
- (7) Kim, J. S.; Jeon, P. E.; Park, Y. H.; Choi, J. C.; Park, H. L.; Kim, G. C.; Kim, T. W. *Applied Physics Letters* **2004**, *85*, 3696.
- (8) Nakamura, S.; Mukai, T.; Senoh, M. *Applied Physics Letters* **1994**, *64*, 1687.
- (9) Sato, Y.; Takahashi, N.; Sato, S. *Japanese Journal of Applied Physics* **1996**, *35*, L838-L839.
- (10) Guha, S.; Haight, R. A.; Bojarczuk, N. A.; Kisker, D. W. *Journal of Applied Physics* **1997**, *82*, 4126.
- (11) Hide, F.; Kozodoy, P.; DenBaars, S. P.; Heeger, A. J. *Applied Physics Letters* **1997**, *70*, 2664.
- (12) Khanna, P.; Singh, N. *Journal of Luminescence* **2007**, *127*, 474-482.
- (13) Bomm, J.; Büchtemann, A.; Fiore, A.; Manna, L.; Nelson, J. H.; Hill, D.; Sark, W. G. J. H. M. van Beilstein *Journal of Nanotechnology* **2010**, *1*, 94-100.
- (14) Williams, A. T. R.; Winfield, S. A.; Miller, J. N. *The Analyst* **1983**, *108*, 1067.
- (15) Peng, X.; Schlamp, M. C.; Kadavanich, A. V.; Alivisatos, a P. *Journal of the American Chemical Society* **1997**, *119*, 7019-7029.
- (16) Xie, R.; Kolb, U.; Li, J.; Basché, T.; Mews, A. *Journal of the American Chemical Society* **2005**, *127*, 7480-8.
- (17) Adachi, S. In *Properties of Group-IV, III-V and II-VI Semiconductors*; John Wiley & Sons, Ltd, 2005; pp. 1-21.
- (18) Aldana, J.; Wang, Y. a; Peng, X. *Journal of the American Chemical Society* **2001**, *123*, 8844-50.
- (19) Wuister, S. F.; Donega, C. D. M.; Meijerink, A. *Journal of Physical Chemistry B* **2004**, *108*, 17393-17397.
- (20) Adachi, S. In *Properties of Group-IV, III-V and II-VI Semiconductors*; John Wiley & Sons, Ltd, 2005; pp. 147-172.
- (21) Adachi, S. In *Properties of Group-IV, III-V and II-VI Semiconductors*; John Wiley & Sons, Ltd, 2005; pp. 195-209.

CHAPTER 3

QD-based Intermediate Band Solar Cell from colloidal Semiconductor Nanocrystals

This chapter discusses the application of semiconductor NCs as “building blocks” to develop a nano-structured multiphase material characterized by an electronic intermediate band located within the semiconductor bandgap. This kind of material (that would be very attracting for photovoltaic applications) has shown to be feasible by enclosing semiconductor nanocrystals into a wider bandgap semiconductor (termed host material).

Basic concepts of an intermediate band material, intermediate band solar cell and intermediate band solar cell based on quantum dots are described in the theoretical introduction (paragraphs 3.1.1 - 3.1.2). The following section presents a possible realization scheme for an intermediate band material, dealing with design issues (paragraphs 3.2.1 - 3.2.5), then describing experimental work (paragraphs 3.3.1 - 3.3.6). Results are presented and discussed in the final section of the chapter (3.4 - 3.5).

Introduction

3.1 Intermediate Band Material

An intermediate band (IB) material is characterized by the existence of energy states, or bands, located within the energy gap between conduction band (CB) and valence band (VB) of a conventional semiconductor^{1,2}.

3.1.1 Intermediate band solar cell

The “Intermediate Band Solar Cell” (IBSC) and its working principles were originally theorized by Luque and Martí in 1997³. The presence of the IB leads to the generation of one extra electron-hole pair when two below-bandgap photons are absorbed³. One photon (*photon 1*) pumps an electron from the VB to the IB while a second photon (*photon 2*) pumps an electron from the IB to the CB. This electron-hole pair adds to those produced conventionally by photons with energy $> E_G$, that excite electrons directly from the VB to the CB (*photon 3*)⁴. The three possible absorption processes in a IB material are schematically represented in Fig. 3.1

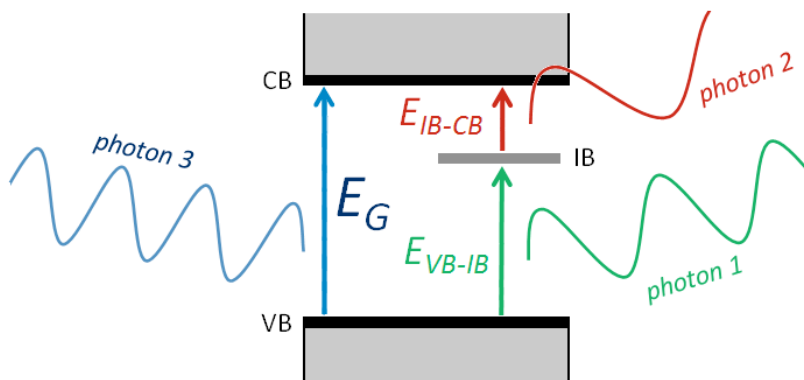


Fig. 3.1: energy bands and possible absorption processes in a IB-material

It can be shown that the voltage supplied by the cell is still limited by the CB-VB bandgap, and not by any of the lower bandgaps², overcoming the problem of increasing the solar cell photocurrent without degrading its voltage⁵. The limiting conversion efficiency of the IB approach reaches 47% at 1 sun (about 63% at full solar concentration^{3,6}), comparing with 43% of two-bandgap tandem solar cell at 1 sun (55% at full solar concentration).

3.1.2 Quantum dots-based intermediate band solar cell (QD-ISBC)

Quantum dots have been proposed to implement an ISBC ⁷. A three dimensional, ordered array of semiconductor nanocrystals (referred as “dot material”), located inside another, higher bandgap semiconductor (referred as “barrier” or “host material”) can be suitable to produce an IB material ^{5,8-10}. The IB would arise within the bandgap of the barrier material from the confined electronic states of the NCs; delocalization of the electrons in the IB could be achieved by increasing the NC density until the electron wave functions have significant overlap and become delocalized ². This geometry is known as “Quantum Dot Supracrystal” (QDS - schematically represented in Fig 3.2). There have been already a number of reported 3D ordered QDS ¹¹⁻¹³, grown by Molecular Beam Epitaxy; it has been only under this approach that, so far, working IBSC have been manufactured ^{4,14}.

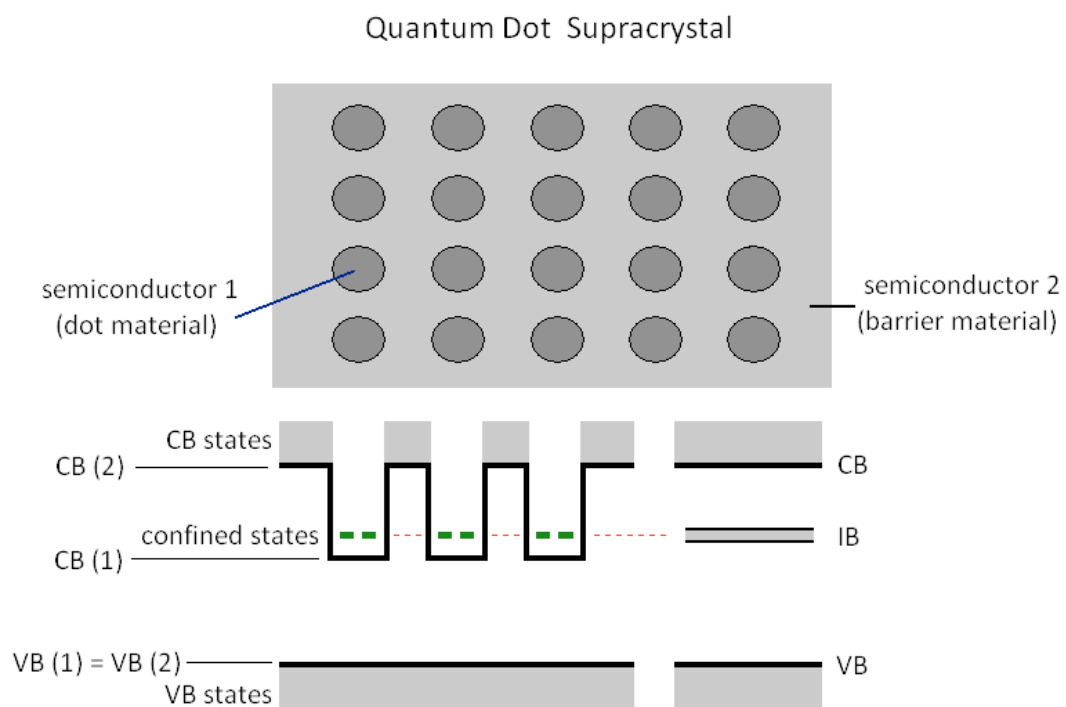


Fig. 3.2: Quantum Dot Supracrystal and its possible electronic bands configuration (in case of VB alignment between dot and barrier material)

An alternative, novel approach to obtain such QDS by simple, low-cost methods would be starting from colloidal synthesized core-shell semiconductor NCs. These synthesis could be carried out at near-ambient temperature and pressure, as explained in Chapter 1. This proposed fabrication approach will be illustrated in the next section (paragraphs 3.2.1 – 3.3.5)

Realization Scheme

3.2 QD-ISBC from colloidal nanocrystals

The final aim of the work described in this chapter is to realize a Quantum Dot Supracrystal (schematically represented in Fig. 3.3, right) through self-assembly and densification of core-shells NCs (schematically represented in Fig. 3.3, left), obtained by colloidal synthesis. The realization of this supracrystal is a multi-step process: (i) material choice; (ii) colloidal synthesis of core-shell NCs; (iii) surface ligands exchange; (iv) assembly; (v) heat treatment/densification. The following paragraphs (3.2.1 - 3.2.5) discuss some theoretical and practical matters regarding the *design* stage of these steps.

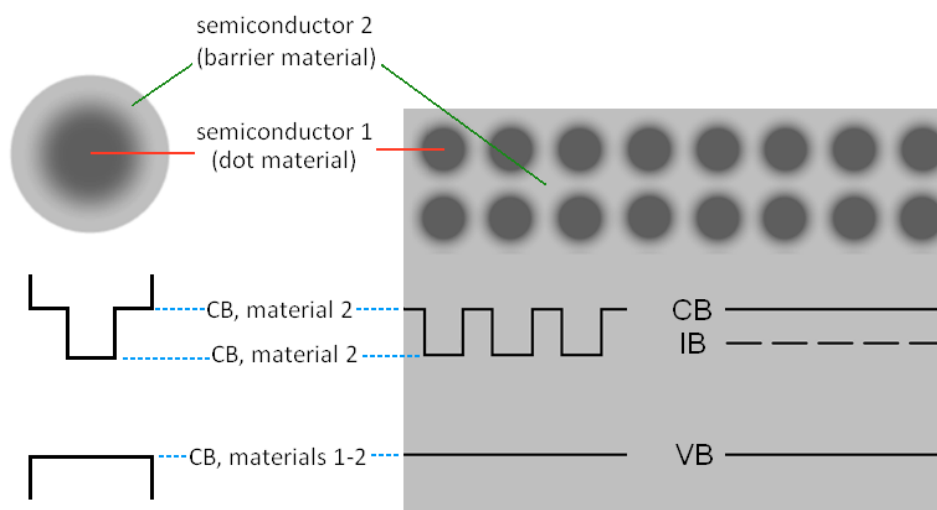


Fig. 3.3: two-phase core-shell semiconductor nanocrystal (left) and nano-structured multiphase material composed of semiconductor nanocrystals embedded into a wider bandgap semiconductor (right)

3.2.1 Materials choice

Selecting the material couple is a complex process; both *ideal* electronic requirements and *practical* synthesis limitations have to be faced. The operation of an ideal IB solar cell depends on a material with three bands: a conduction band (CB), a valence band (VB) and an intermediate band (IB); the positions of which, in this approach, depend on (i) the chosen semiconductor couple; (ii) dot material dimension and (iii) dot interspacing. The *ideal* electronic requirements for a QD-ISBC material, according to Levy et al.¹⁵, are the followings:

- (1) The barrier material must have a bandgap E_G between 1.43 eV and 2.56 eV (this would approximately guarantee a theoretical maximum efficiency above 60%³).
- (2) The offset between the VB (or, alternatively the CB) edges of dot material and barrier material must be negligible.
- (3) The offset between the other band edges must be greater than $(0.48 * E_G - 0.22 \text{ eV})$.

These three points will be considered as the *ideal criteria 1,2 and 3* to choose the couple *dot material – barrier material* to synthesize the *core-shell* nanocrystals that will be used as “building blocks”. Additional *practical* issues have to be evaluated:

- i) Colloidal synthesis of dot-barrier material couple in form of core-shell NCs should be available in literature and possibly meet green chemistry principles.
- ii) Lattice mismatch between dot and barrier material should be as low as possible, to ease the shell growth.
- iii) Inter-diffusion between dot and barrier material should be negligible at heat treatment temperature.

These three additional points will be considered as the *practical criteria i, ii and iii*. Materials evaluated for this work were chosen among II-VI semiconductors. Crystal structure, effective lattice constant (= lattice parameter a for zinc-blende crystals, $=(\sqrt{3}a^2c)^{1/3}$ for wurtzite crystals) bandgap energy E_G and CB and VB positions respect to the vacuum level are shown in Table 3.1; E_G and band offsets are graphically represented in Fig 3.4.

compound	crystal structure	a^* (Å)	E_G (eV)	E_{CB} (eV)	E_{VB} (eV)
CdS ¹⁶⁻²⁰	wurtzite	5.84	2.42	-4.77	-7.25
CdSe ¹⁶⁻¹⁹	wurtzite	6.07	1.75	-4.95	-6.7
CdTe ¹⁶⁻¹⁸	zinc-blende	6.48	1.51	-4.5	-6.01
ZnS ¹⁶⁻¹⁸	wurtzite	5.4	3.75	-3.9	-7.65
ZnSe ^{16-18,21}	zinc-blende	5.67	2.72	-4.06	-6.78
ZnTe ¹⁶⁻¹⁸	zinc-blende	6.01	2.27	-3.68	-5.95

Table 3.1: crystal structure, effective lattice constant a^* , bandgap energy E_G and bands position E_{CB} and E_{VB} (of CB and VB respectively, expressed as energy respect to vacuum level) of II-VI compounds evaluated in this work

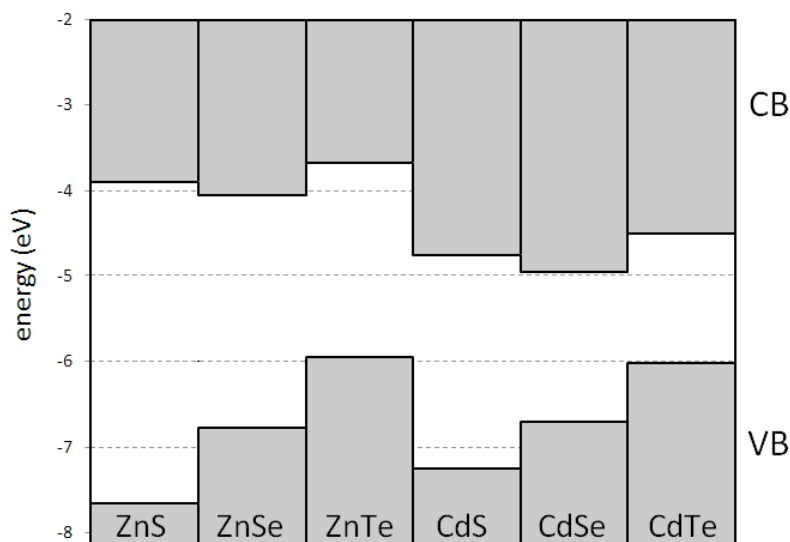


Fig. 3.4: CB and VB positions respect to the vacuum level of II-VI compounds evaluated in this work (values from Adachi¹⁶⁻¹⁸)

3.2.2 Dot material choice

An ideal dot material should be easily obtainable through green, colloidal chemistry methods in the form of spherical-shaped NCs; its bandgap should be as small as possible (in order that it would be possible, by changing dot size, to tune its absorbance properties in a wider region, from near-IR to visible spectrum). Therefore, the best candidates as dot material, among these II-VI semiconductor compounds, are CdTe and CdSe.

3.2.3 Barrier material choice

(i) Ideal requirements

Among these II-VI semiconductors, *criterion 1* would limit the possible choices between CdTe ($E_G = 1.51$ eV), CdSe ($E_G = 1.75$ eV), ZnTe ($E_G = 2.27$ eV) and CdS ($E_G = 2.42$ eV). Nevertheless, since both CdTe and CdSe are already good candidates as dot material (and, more important, choosing CdTe or CdSe as barrier material would leave no appropriate dot material among II-VI semiconductors), ZnTe and CdS appear to be the only suitable possibilities (if we consider just *criterion 1*). CdS shell nearly respects *criterion 2*, if overgrown on CdSe or CdTe dots (CB offset: 0.18 eV and 0.27 eV respectively), but meets *criterion 3* only if coupled with CdTe (VB offset: 1.27 eV). Considering *criterion 2*, ZnTe appears to be the ideal choice for CdTe-ZnTe dot-barrier pair (VB offset: 0.06 eV); moreover, it is also possible to consider ZnSe ($E_G = 2.72$), which, despite being slightly out of range for *criterion 1*, would be the perfect choice if coupled with CdSe dots (VB offset: 0.08 eV). Summarizing, CdTe-CdS dot-barrier pair meets all 3 criteria; CdSe-CdS and CdTe-ZnTe meets criteria 1 and 2; CdSe-ZnSe only criterion 2.

(ii) *Practical considerations*

Criteria i and *ii* limit the practical available options: CdTe-ZnTe pair, despite meeting *criteria 1* and *2*, is not easy to synthesize in form of colloidal core-shell nanocrystals (only one synthesis method reported²²); ZnTe itself is not easy obtainable without using air-sensitive precursors^{23,24}. *Criterion ii* discourage the CdTe-CdS choice (that was meeting *criteria 1,2* and *3*), favoring instead CdSe-CdS and CdSe-ZnSe pairs. *Criterion iii* excludes CdSe-ZnSe pair: this heterostructure start interdiffusing already at 270 °C (in common-anion systems, according to van Embden et al.²⁵, the diffusion of the smaller cations is more efficient between tetrahedral interstitial states).

Therefore, it has been decided to synthesize CdSe-ZnSe, CdTe-CdS and CdSe-CdS systems; finally, most of the experimental work was carried out on latter system, that was: (a) the easier to synthesize in spherical form; (b) the harder to interdiffuse; (c) the easier to characterize by fluorescence spectroscopy.

3.2.4 Organic ligands removal

Organic ligands (oleic acid and trioctylphosphine) used in the synthesis step remain bound on NCs surface (as discussed in Chapter 1, pp. 15,40,41), and can represent a physical barrier to the external shell material sintering process. A previous study²⁶ shows that long chain carboxylic acids remain bound on NC surfaces up to temperatures higher than 400 °C, well above their boiling points (about 300 °C). Therefore, they are not easily removed by applying a heat treatment (at least not without exposing the heterophasic core-shell nanocrystal to an unwanted alloying process). In this work, it was preferred to chemically substitute them with short chain thiols, to ease their subsequent removal by means of heat treatment. The selected ligands have lower boiling point (between 100 and 220 °C), and are known to be desorbed from the surface of CdS nanocrystals between and 190 and 250 °C²⁷.

3.2.5 Heat treatment design

The final heat treatment application had to be conceived to sinter the external shell material while preserving the nano-heterostructure (that is avoid the alloying of core and shell materials). Sintering can be seen as a densification method based on atomic diffusion²⁸; being a thermally activated process, diffusion occurs much faster at higher temperatures. In most sintering processes, the material is heated to a sintering temperature T_s , below the melting point T_M (usually $T_s \approx 2/3 T_M$). The atoms diffuse across the boundaries of crystallites, fusing the particles together and therefore creating bigger crystallites. The driving force for this process is the change in free energy E , which has two contributes: (i) the decrease in surface area and (ii) the lowering of the surface free energy (by the replacement of solid-vapor interfaces with solid-solid interfaces). If the size of the particle is small (or if the radius of curvature is large), these effects become very large in magnitude, leading to sintering and even melting at lower temperatures. It is also known that melting temperature of nano-sized crystals decreases with dimension; Goldstein and co workers²⁷ reported a difference between bulk CdS melting temperature and nano-sized CdS melting temperature larger than 1000 K for crystallite with a radius below 2 nm. According to their work, CdS crystallites with a diameter ranging between 6-7 nm (about the size of nano-heterostructures used in this work, whose external material is CdS) should have a melting temperature $T_M \approx 825$ °C; therefore a good sintering T temperature for these crystallites should be ≈ 550 °C.

3.2.6 Monitoring the nanostructure evolution during heat treatments

The optimal sintering temperature and time were determined experimentally, following the bandgap evolution of CdS NCs and CdSe-CdS core-shell NCs during the heat treatments via fluorescence spectroscopy.

3.3 Experimental

3.3.1 Materials

3-mercaptopropionic acid (MPA, >99%) , mercaptoacetic acid (MAA, > 98%), methanol (>99.8%), ethanol (>99.5%), acetone (>99.8%), n-hexane (>95%), cadmium sulfide powder (CdS, > 99%), cadmium selenide powder (CdSe, >99%) were obtained from Sigma-Aldrich. CdSe-ZnSe, CdSe-CdS and CdTe-CdS core-shell NCs, CdS and ZnSe single-phase NCs were synthesized and characterized as explained in Chapter 1.

3.3.2 Ligands exchange procedure

0.1 mmol of core-shell nanoparticles (CdSe-ZnSe, CdSe-CdS or CdTe-CdS) or 0.1 mmol of single-phase NCs (CdS or ZnSe) were washed twice with methanol, precipitated with acetone and re-dissolved in 4 ml of n-hexane; 0.1 mmol of new ligand (MPA or MAA) were added; the NCs started aggregation/flocculation almost immediately; the suspension was vigorously stirred for 30-60 minutes. Then the suspension was divided in two test tubes; 2 ml of n-hexane and 2 ml of acetone were added to each tubes, vigorously mixed, then centrifuged for several minutes. At this point, a colored precipitate appeared in the bottom of the test tubes: the precipitate was then washed and centrifuged/precipitated twice with n-hexane , then it was dispersed in 2 ml ethanol or methanol

3.3.3 Assembly

Glass microscope slides (Corning, 75x25 mm, plain, purchased from Sigma-Aldrich) were cleaned by two-step sonications (5 minutes ultrasonic cleaning in acetone, dried with nitrogen flow, then 5 minutes ultrasonic cleaning in 2-propanol, finally dried with nitrogen flow; a Branson 2200 Ultrasonic Cleaner was used). Samples were then cut into 5mm x 5mm pieces and heated to 50 °C on a hot plate. Ligand-exchanged NCs were drop casted on hot glass substrates from ethanol or methanol dispersion (generally 2 drops for a 5x5 mm glass substrate); after solvent evaporation, samples (shown in Fig 3.5) were removed from the hot plate.

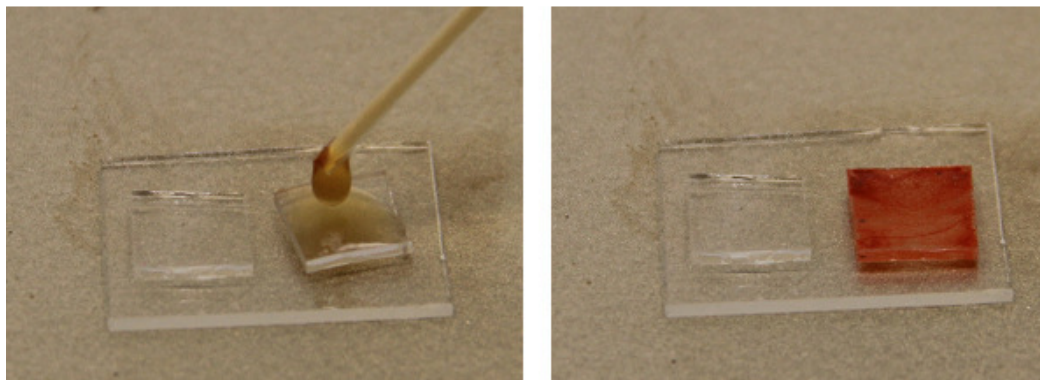


Fig. 3.5: (left) drop casting of NCs suspension on a 5x5 mm glass substrate (right): sample after solvent evaporation

3.3.4 Heat treatments

Heat treatments were performed in a Linn High Therm VMK 1800 furnace; NCs assembled on 5x5 mm glass substrates were put on aluminum oxide holders and heated to 300 °C, 350 °C, 400 °C and 500 °C, for times between 0.5 and 120 minutes.

3.3.5 Fluorescence wavelength measurement

Fluorescence spectra of as-deposited samples, of heat-treated samples and of commercial available CdS and CdSe powders were acquired through an Renishaw InVia Raman Microscope equipped with a RenCam CCD detector, operated by a Renishaw Wire 3 software; peak positions were determined by fitting spectra with log-normal curves (using ThermoGalactic Grams/Al 7.02). Excitation sources were an Omicron Bluephoton® 480 mW diode laser emitting at 405 nm, a SpectraPhysics 50 mW argon-ion laser emitting at 514.5 nm and a Renishaw HP NIR 300 mW diode laser emitting at 785 nm.

Results and Discussion

3.4 Heat Treatments

3.4.1 Heat treatment effect on single-phase NCs

CdS NCs were heated to 300, 350 and 400 °C for times between 0 and 50 minutes. Fig. 3.6 summarizes the bandgap energy (determined from fluorescence data) as a function of heating times.

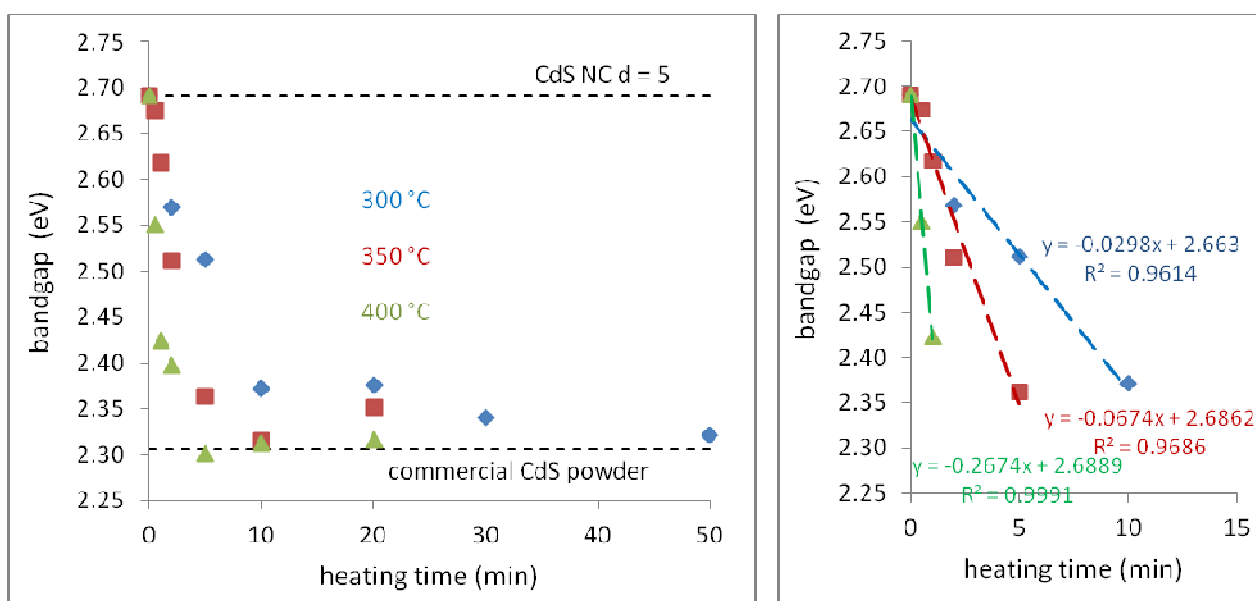


Fig. 3.6 - (left): bandgap energy of CdS NCs as a function of heat treatment time for three different temperatures: 300 °C (blue); 350 °C (red) and 400 °C (green);
- (right): linear interpolations of first experimental points give kinetic constants k

Dotted lines represent: (upper dotted line) apparent bandgap of CdS NC (with a diameter $d = 5$ nm);
(bottom dotted line) bandgap of commercial CdS powder

One can see that the apparent bandgap of the CdS NC decreases with heat treatment time, down to a value that is comparable to the one registered from commercial-available CdS powder. This bandgap energy decrease is consistent with an increase in crystallite dimension (NCs merging together); being the nanocrystal apparent bandgap E_{NC} the sum of bulk material bandgap E_G , electron confining potential E_E and hole confining potential E_H , when increasing the NC size, both E_E and E_H decrease, leading to a decrease of E_{NC} . When crystallite become larger than Bohr radius, E_{NC} approaches the value of the bulk material E_G (as schematized in Fig. 3.7).

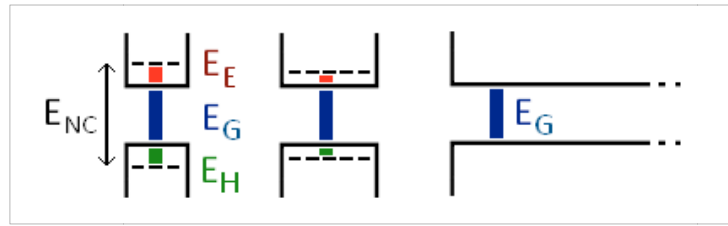


Fig. 3.7: schematization of apparent bandgap decrease with increasing NC size: apparent bandgap E_{NC} is represented by the sum of bulk material bandgap E_G (blue), electron confining potential E_E (red) and hole confining potential E_H (green)

It is possible to notice that this decrease is faster at higher temperatures, as it should be, since sintering is a thermal activated process. It is possible to find a kinetic constant k for every temperature by linearly interpolating the first experimental points; for a thermally activated process, an Arrhenius plot (which is $\ln(k)$ as a function of $1/T$) should give a straight line, from which the activation energy E_A can be determined. The gradient of the linear interpolation of the Arrhenius plot gives $-E_A/R$; in principle, it is therefore possible to estimate the activation energy.

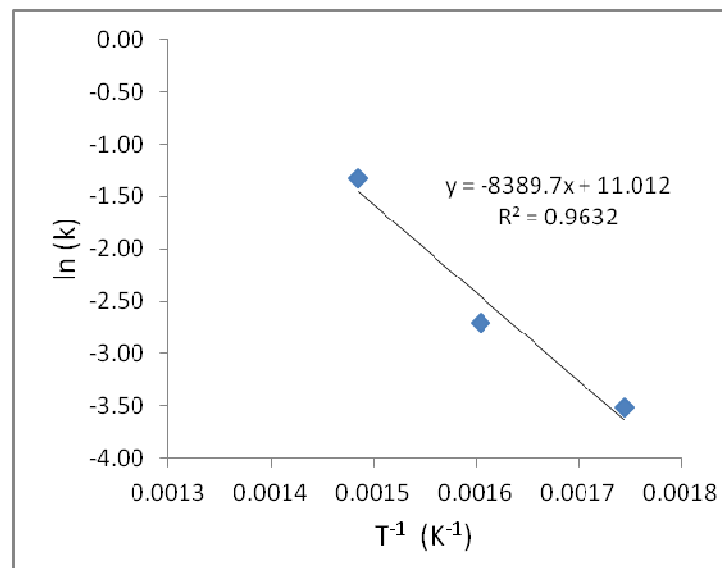


Fig. 3.8: Arrhenius plot ($\ln(k)$ as a function of $1/T$) for bandgap energy variation (initial, linear part) in CdS NCs.

For the case examined here, i.e. for sintering of CdS NCs with a diameter of about 5 nm, only three data points are available and no strong conclusion can be drawn. Nevertheless, under reasonable assumption that the process behaves like a thermally activated process, the activation energy E_A can be estimated to be in the range of 70 kJ/mol. It can be concluded that it is possible to increment CdS NCs size, most likely via a sintering process, through heat treatments.

3.4.2 Heat treatment effect on multi-phase NCs

Fig. 3.9 summarizes the apparent bandgap energy (determined from fluorescence data) as a function of heating times for CdSe-CdS NCs heated at 300, 350, 400 and 500 °C. It can be seen that during heat treatment the apparent bandgap of CdSe-CdS core-shell NC initially decreases down to a common value, then increase to energies even higher than the original NC apparent bandgap. It can be noticed that both variation are faster at higher temperatures. The bottom energy bandgap threshold is higher than the bandgap of commercial-available CdSe powder (1.75 eV), leading to the likely conclusion that CdSe cores are not merging together. The initial bandgap energy decrease is consistent with an increase in shell dimension (the external material is merging together). Given the particular band offset of CdSe-CdS heterojunction (represented in Fig. 3.10, left), and being the nanocrystal apparent bandgap E_{NC} the sum of (i) bulk material bandgap E_G ; (ii) electron confining potential E_E and (iii) hole confining potential E_H , this implies that after merging the external material (CdS) only E_E should decrease, while E_H should not (hole remain confined into CdSe quantum wells - as schematized in Fig. 3.10, right).

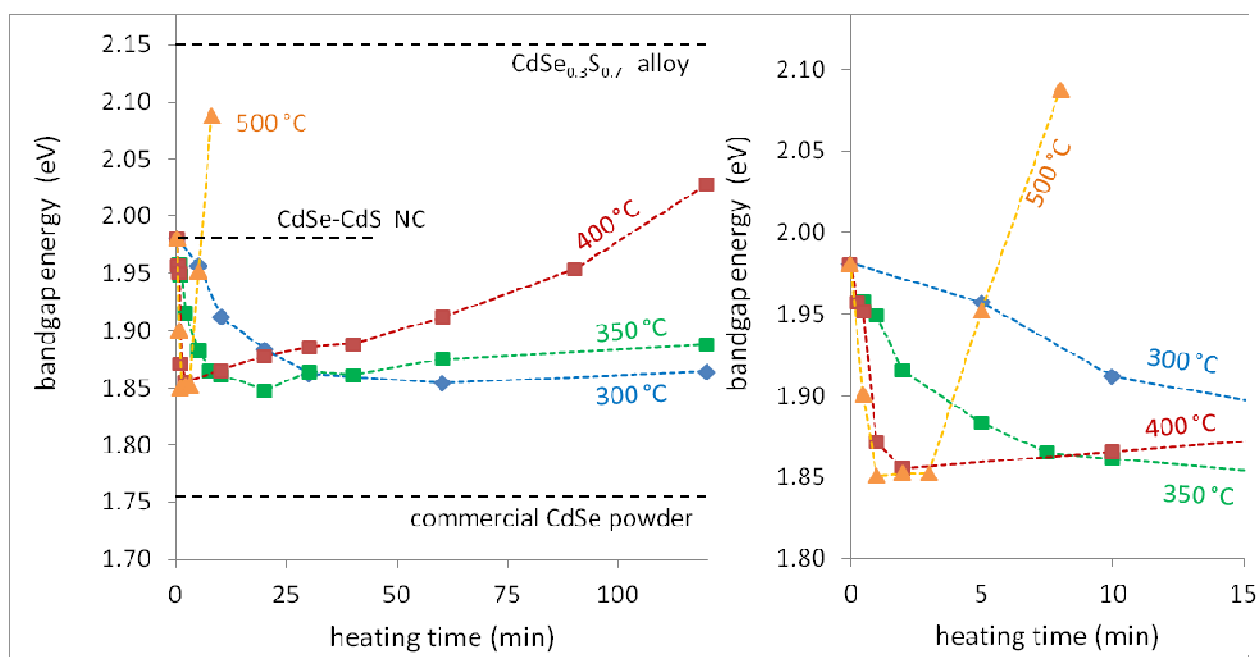


Fig. 3.9 - (left): bandgap energy of CdSe-CdS core-shell NCs as a function of heat treatment time for different temperatures: 300 °C (blue); 350 °C (green); 400 °C (red) and 500 °C (orange);
- (right): detail of the first 15 minutes region

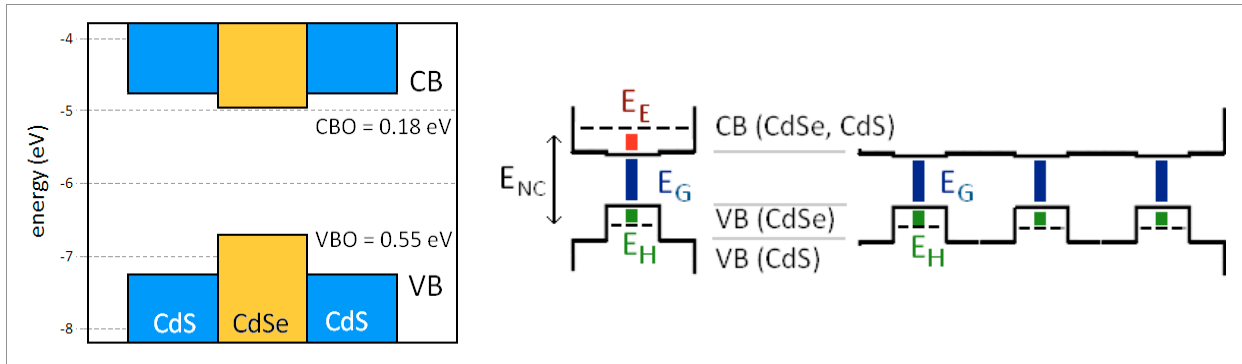


Fig. 3.10 (left): band offset in a CdSe-CdS heterojunction

(right): schematization of apparent bandgap decreasing with CdS shell merging together: apparent bandgap E_{NC} is represented by the sum of bulk CdSe bandgap E_G (blue), electron confining potential E_E (red – decreasing while CdS shell merge together) and hole confining potential E_H (green, that is not influenced by CdS shell merging)

The successive bandgap energy increase is consistent with alloying of CdSe and CdS: the bandgap of the alloyed material changes as a function of composition, according to Vegard's Law. Core-shell NCs used in this study were composed by a CdSe core with a diameter of 3.2 nm, and a 5ML-thick CdS shell, corresponding to a molar ratio S/Se of 2.44 (that is a $CdSe_xS_{1-x}$ alloy with $x = 0.3$). Under this assumptions, this alloy should have a bulk material E_G of about 2.15 eV.

It is possible to notice that both initial bandgap decrease rate and subsequent bandgap increase rate are faster at higher temperatures, as should be, since sintering and diffusion are a thermal activated processes. It is possible to find the kinetic constants k for every temperature, linearly interpolating the first experimental points (for sintering), or last experimental points (for diffusion). Activation energies can be estimated from Arrhenius plots (shown in Fig. 3.11)

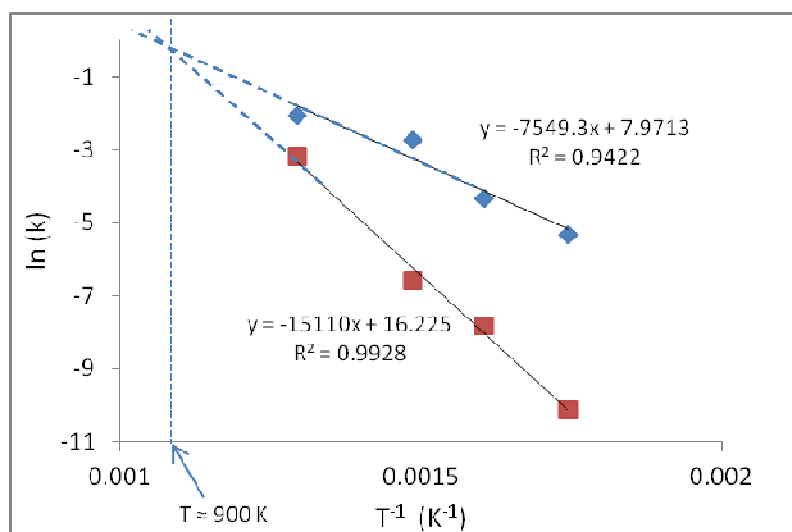


Fig. 3.11: Arrhenius plot for bandgap energy variation (blue: initial part – red: final part) in CdSe-CdS NCs.

Both the processes behaves like a thermal activated processes; activation energies can be estimated for sintering of external material ($E_A = 63$ kJ /mol) and reciprocal diffusion of CdSe into CdS ($E_A = 126$ kJ /mol). It should be noted that the activation energy (63 kJ /ml) found for sintering of shell material (which is, as already mentioned, CdS) is similar to the activation energy (70 kJ/mol) found for sintering of single phase CdS NCs with similar curvature. The activation energy required for reciprocal diffusion is higher than that required for sintering; according to the plot in Fig. 3.11 (intercept of the two linear fittings at $1/T = 0.0011 \rightarrow T \approx 900$ K), the sintering of the shell material should be faster than core-shell materials inter-diffusion for $T \leq 900$ K (≈ 630 °C). Practically, as it can be noticed in Fig 3.9, bandgap energy change is so fast at $T > 400$ °C (minimum bandgap energy is reached after 2 minutes at 400 °C, in less than 1 minute at 500 °C) that it is better to apply longer heat treatment at lower temperature (for example 50 minutes at 300 °C or 25 minutes at 350 °C) to finely control the nanostructure and avoid interdiffusion.

These results suggest that is possible to sinter the external material (CdS) without altering the nano-heterostructure, if temperature and time of heat treatment are controlled properly. The proposed nanostructure evolution during heat treatment is schematized in Fig. 3.12.

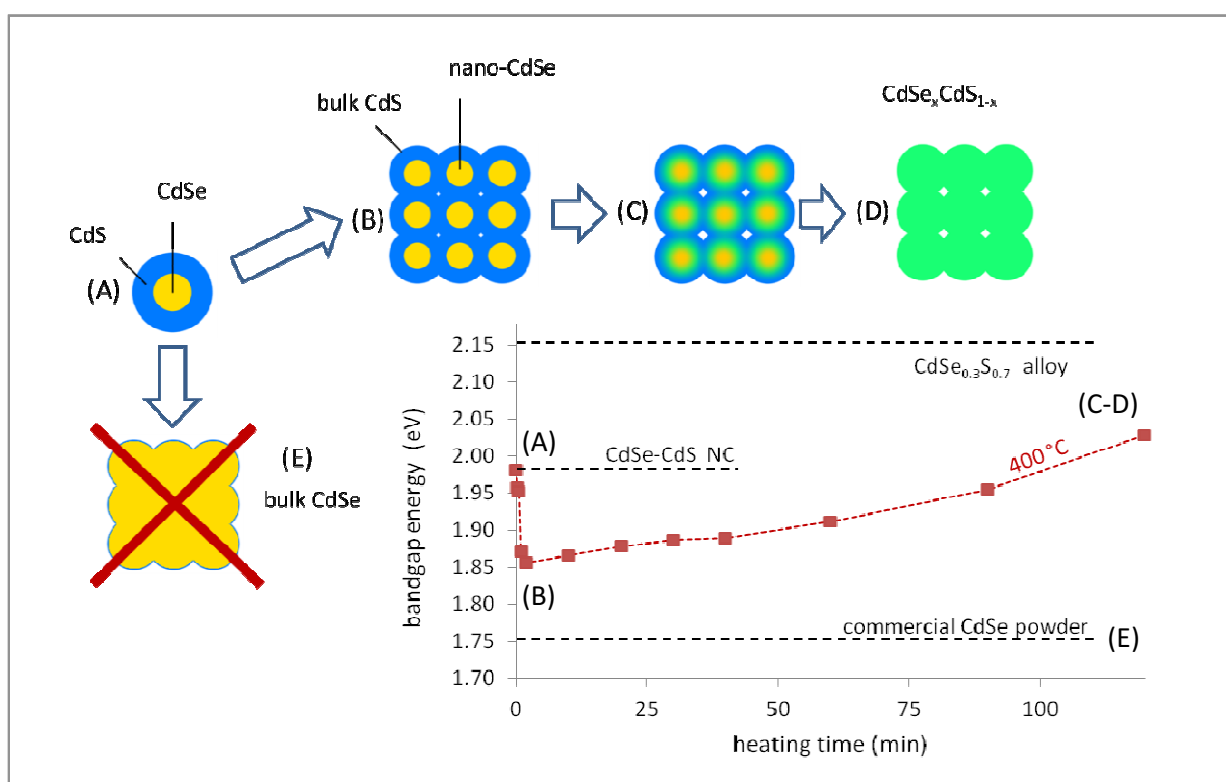


Fig. 3.12 : bandgap energy evolution (plot) and proposed nanostructure evolution (sketched) at 400 °C:
 from CdSe-CdS NC (A) heat treatment initially cause a bandgap decrease;
 bandgap does not decrease down to the bulk CdSe value (E);
 bandgap decreases to a value consistend with nano-CdSe enclosed into a CdS matrix (B);
 then, the heterostructure start alloying (C-D), causing an increase in the bandgap energy.

3.5 Conclusions and future developments

These results, although direct observations (e.g. TEM) are still needed to confirm them, suggest that it is possible to obtain the desired nano-geometry (CdSe QDs embedded into a CdS matrix) starting from colloidal CdSe-CdS core-shell NCs, via a multiple step process:

- (i) synthesis
- (ii) organic ligands removal
- (iii) sintering of the shell materials

These results set the stage for interesting future developments. Other systems could be tested: CdTe-CdS is a promising system, but synthesis techniques have to be improved to obtain spherical-shaped core-shell systems. Other characterization techniques, such as wide-angle X-Ray diffraction and Transmission Electron Microscopy could be used in parallel to spectroscopic techniques to characterize the nanostructure evolution. Once obtained the desired material, this could be integrated into a simple Schottky junction (example shown in Fig. 3.13), and its spectral efficiency tested. The photogeneration of current when illuminated with photon of energy lower than the bandgap of the barrier material will be regarded as a major indication of an electronic intermediate band in this kind of architecture.

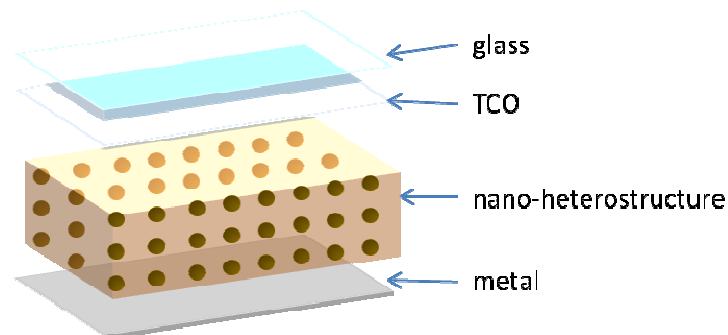


Fig. 3.13. : example of Schottky junction. Different layers, from top to bottom: glass, front contact (Transparent Conductive Oxide –TCO – such as Indium Tin Oxide), QD-based nano-heterostructure as absorbent material, metal (such as aluminum or gold)

References

- (1) Marti, A.; Lopez, N.; Antolin, E.; Canovas, E.; Stanley, C.; Farmer, C.; Cuadra, L.; Luque, A. *Thin Solid Films* **2006**, *511-512*, 638-644.
- (2) Luque, A.; Marti, A.; Nozik, A. J. *MRS Bulletin* **2007**, *32*, 236-241.
- (3) Luque, A.; Marti, A. *Physical Review Letters* **1997**, *78*, 5014-5017.
- (4) Marti, A.; Antolin, E.; Stanley, C.; Farmer, C.; Lopez, N.; Daaz, P.; Canovas, E.; Linares, P.; Luque, A. *Physical Review Letters* **2006**, *97*, 1-4.
- (5) Tomic, S.; Harrison, N. M.; Jones, T. S. *Optical and Quantum Electronics* **2008**, *40*, 313-318.
- (6) Luque, A.; Marti, A. *Progress in Photovoltaics: Research and Applications* **2001**, *9*, 73-86.
- (7) Marti, A.; Cuadra, L.; Luque, A. In *Conference Record of the 28th IEEE Photovoltaic Specialists Conference, 2000*; IEEE; pp. 940-943.
- (8) Tomic, S.; Jones, T. S.; Harrison, N. M. *Applied Physics Letters* **2008**, *93*, 263105.
- (9) Cuadra, L. *Thin Solid Films* **2004**, *451-452*, 593-599.
- (10) Shao, Q.; Balandin, A. A.; Fedoseyev, A. I.; Turowski, M. *Applied Physics Letters* **2007**, *91*, 163503.
- (11) Mazur, Y. I.; Ma, W. Q.; Wang, X.; Wang, Z. M.; Salamo, G. J.; Xiao, M.; Mishima, T. D.; Johnson, M. B. *Applied Physics Letters* **2003**, *83*, 987.
- (12) Springholz, G. *Science* **1998**, *282*, 734-737.
- (13) Kiravittaya, S.; Benyoucef, M.; Zapf-Gottwick, R.; Rastelli, A.; Schmidt, O. G. *Applied Physics Letters* **2006**, *89*, 233102.
- (14) Luque, A.; Martí, A.; Stanley, C.; López, N.; Cuadra, L.; Zhou, D.; Pearson, J. L.; McKee, A. *Journal of Applied Physics* **2004**, *96*, 903.
- (15) Levy, M. Y.; Honsberg, C.; Marti, A.; Luque, A. *Conference Record of the 31st IEEE Photovoltaic Specialists Conference, 2005* **2005**, 90-93.
- (16) Adachi, S. In *Properties of Group-IV, III-V and II-VI Semiconductors*; John Wiley & Sons, Ltd, 2005; pp. 1-21.
- (17) Adachi, S. In *Properties of Group-IV, III-V and II-VI Semiconductors*; John Wiley & Sons, Ltd, 2005; pp. 103-145.
- (18) Adachi, S. In *Properties of Group-IV, III-V and II-VI Semiconductors*; John Wiley & Sons, Ltd, 2005; pp. 195-209.
- (19) Horley, P.; Gorley, V.; Gorley, P.; Gonzalezhernandez, J.; Vorobiev, Y. *Thin Solid Films* **2005**, *480-481*, 373-376.
- (20) Schooss, D.; Mews, A.; Eychmüller, A.; Weller, H. *Physical Review B* **1994**, *49*, 17072-17078.
- (21) Nikesh, V. V.; Lad, A. D.; Kimura, S.; Nozaki, S.; Mahamuni, S. *Journal of Applied Physics* **2006**, *100*, 113520.
- (22) Law, W. C.; Yong, K. T.; Roy, I.; Ding, H.; Hu, R.; Zhao, W.; Prasad, P. N. *Small* **2009**, *5*, 1302-10.
- (23) Zhang, J.; Sun, K.; Kumbhar, A.; Fang, J. *Journal of Physical Chemistry C* **2008**, *112*, 5454-5458.
- (24) Bang, J.; Park, J.; Lee, J. H.; Won, N.; Nam, J.; Lim, J.; Chang, B. Y.; Lee, H. J.; Chon, B.; Shin, J.; Park, J. B.; Choi, J. H.; Cho, K.; Park, S. M.; Joo, T.; Kim, S. *Chemistry of Materials* **2010**, *22*, 233-240.
- (25) Van Embden, J.; Jasieniak, J.; Gomez, D. E.; Mulvaney, P.; Giersig, M. *Australian Journal of Chemistry* **2007**, *38*, 457-471.
- (26) Jasieniak, J.; MacDonald, B. I.; Watkins, S. E.; Mulvaney, P. *Nano letters* **2011**, *11*, 2856-64.
- (27) Goldstein, A. N.; Echer, C. M.; Alivisatos, A. P. *Science* **1992**, *256*, 1425-7.
- (28) Kingery, W. D.; Bowen, H. K.; Uhlmann, D. R. *Introduction to Ceramics, 2nd ed.*; John Wiley & Sons, 1967.